Large Deformation Behavior of Rubber-Plastic Laminates

by

Rahul Gopalan Ramachandran

Bachelor of Technology, National Institute of Technology Calicut, 2012

Master of Engineering, Indian Institute of Science Bangalore, 2016

Submitted to the Graduate Faculty of the

Swanson School of Engineering in partial fulfillment

of the requirements for the degree of

Doctor of Philosophy

University of Pittsburgh

2022

UNIVERSITY OF PITTSBURGH

SWANSON SCHOOL OF ENGINEERING

This dissertation was presented

by

Rahul Gopalan Ramachandran

It was defended on

January 31, 2022

and approved by

Dr. Anne Robertson, Professor, PhD, Professor, Department of Mechanical Engineering and Materials Science

Dr. William Slaughter, Professor, PhD, Professor, Department of Mechanical Engineering and Materials Science

Dr. Rajendra K. Krishnaswamy, PhD, CJ Bio Group

Dissertation Director: Dr. Spandan Maiti Professor, PhD, Professor, Department of Bioengineering

Dissertation Director: Dr. Sachin S. Velankar, Professor, PhD, Professor, Department of Chemical Engineering

Large Deformation Behavior of Rubber-Plastic Laminates

Rahul Gopalan Ramachandran, PhD

University of Pittsburgh, 2022

We study the large deformation behavior of rubber-plastic laminates in this thesis. Tensile, fracture, and shape programming with uniaxial tensile deformation is discussed. This research showed that the tensile behavior of the laminates resembles a second-order phase transition. For sufficiently small rubber/plastic thickness ratio, the rubber-plastic laminates showed necking and drawing, wherein a tensile bar coexists in two strain states, one with a large stretch (necked phase) and the other with a modest stretch (unnecked phase). With increasing rubber/plastic thickness ratio, the two strain states approached each other, culminating in a critical point. The distinct effect of rubber properties, i.e., modulus and strain hardening, on the phase diagram and the critical point are also discussed.

Turning to fracture, specimens of plastic with a sharp notch failed by forming a highly stretched neck-like process zone at the notch tip. Close inspection of notch tip of the plastic material revealed notch blunting and the initiation of a secondary crack inside the process zone. The stress analysis through finite element simulations further revealed that the crack initiation occurs at a location with high stress triaxiality. Bonding a rubber layer is showed to modify the process zone and reduce the magnitude of stress triaxiality in the plastic. The result is a dramatic improvement in flaw tolerance with rubber addition.

Finally, we examined shape-morphing of rubber-plastic laminates. Uniaxially stretching a rubber-plastic bilayer composite beyond its yield point created an elastic strain mismatch between the two layers. Upon release, the bilayer bent out-of-plane. In rubber-plastic bilayers we showed a

remarkable dependence of the final shape upon the stretch applied prior to release. All bilayers bent into arch or roll shapes with the plastic on the convex face at a small applied stretch. At a large stretch, the bilayers bent into half-tubes with the plastic, now heavily wrinkled, becoming the concave face. Between these two extremes, saddle shapes appeared that have characteristics of both arches and half-tubes. The flip in shape formed was driven by the significant yielding in compression and formation of plastic wrinkles. A model was developed which predicts these shape changes through energy minimization.

Table of Contents

List of Tables

List of Figures

Preface

I would like to sincerely acknowledge the efforts of many people who have been an integral part of my thesis. During my PhD, I have been fortunate to be part of two research groups lead by Dr. Sachin Velankar and Dr. Spandan Maiti. The conducive work environment in both the groups made my PhD enjoyable. This thesis involves both experimental and numerical techniques which was guided throughout by both my supervisors. Regular discussions with Dr. Sachin Velankar, was central to the development of ideas that have been explored in this thesis. Much of the experiments in this thesis involve everyday materials, equipment and devices. This is largely inspired by the guidance of Dr. Sachin Velankar. Working on these experiments has taught me to look at even the simplest things for utility. I started my PhD with little knowledge of scientific computing. I would like to thank Dr. Spandan Maiti's guidance and support with code development and guiding through the nuances of numerical techniques.

I would like to thank the committee members, Dr. Anne Robertson and Dr. William Slaughter, whose suggestions enriched this thesis. Incidentally, their courses on continuum mechanics laid the foundation for all discussions in this thesis. I am also thankful for the contribution of Dr. Rajendra Krishnaswamy for his input on practical applications.

I would also like to acknowledge Dr. Siladitya Pal, Dr. James Thunes, and Ronald Fortunato for their contribution to the base finite element code central to this work. I would also like to thank Jonah De Cortie, Zachery Kushnir, S. Hariharakrishnan, and Zang Yi, whose experiments have directly contributed to this work.

I would also like to acknowledge the help from Dr. Steve Abramovich for guiding the tracking part of the digital image correlation package and lending access to the tensile testing

machine. I would also like to thank Dr. Luca Deseri for guiding me with the modelling of shape generation.

An intensive project like a PhD thesis naturally can have its ups and downs. Part of the work for this thesis was done during an ongoing pandemic, and therefore most of the work was done from home. I am grateful to all my friends, Ankit and Rithwik, for being wonderful roommates. Finally, I am thankful for consistent support from my parents, brother, and especially my friend and now wife Anwesha.

1.0 Introduction

Elastomers like rubbers and gels and semicrystalline plastics like polyethylene can sustain large deformation without failure. However, the mechanical responses of these two materials are quite distinct. Elastomers, for example a household rubber band, can stretch uniformly and recover their initial shape upon unloading. In contrast, pulling a piece of grocery bag made of polyethylene creates inhomogeneous deformation and does not recover its original shape upon unloading. The stretching behavior of a rubber band and a polyethylene grocery bag is shown in Figure 1.

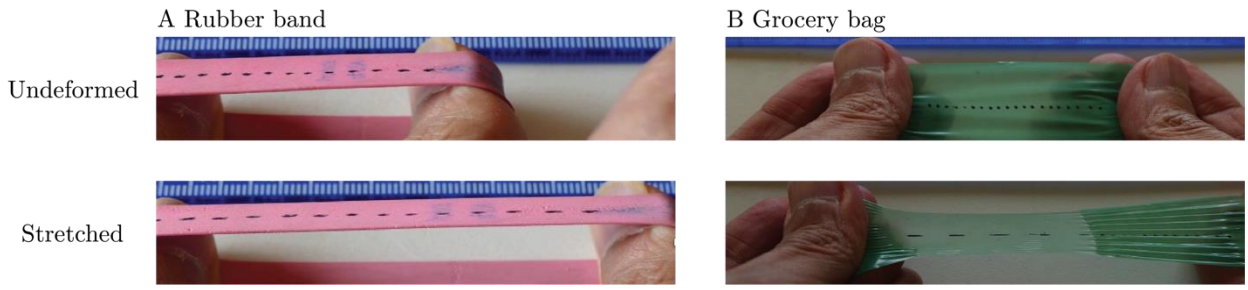

Figure 1: (A) Homogenous deformation of a rubber band. (B) Inhomogeneous deformation of a strip cut from grocery bag showing neck formation. Black dots in both images are ink markers.

Composite materials are often formed by combining highly dissimilar constituents because of functional, mechanical, or cost incentives. Our everyday cloth fabrics are often a blend of natural and synthetic fibers like cotton, wool, nylon, and polyester, etc., to achieve required thermal, comfort, and cost considerations. Similarly, everyday building material, concrete, is reinforced with steel rods to improve its tensile properties. Plastics reinforced with glass or carbon fibers are commonly used in high-end applications such as aircraft. Sometimes, constituent materials of a composite can even have diametrically different functional properties. For example, electrical conductors can be embedded in an insulating polymeric matrix to form moldable

conductors(Amoabeng & Velankar, 2017). In this context, composites made up of elastic layers, whose deformation is mostly recoverable, and plastic layers, whose deformation is mostly irrecoverable, have been studied. For example, bonding a layer of elastomer to a ductile metal allowed the layered composite to stretch to a larger extent without necking, whereas the metal alone would neck to failure at only a small-applied strain(T. Li, Huang, Suo, Lacour, & Wagner, 2004; N. S. Lu, X. Wang, Z. G. Suo, & J. Vlassak, 2007). However, very little is known about the mechanics of soft elastic-plastic laminates that can undergo large deformations many times their original dimensions. This thesis studies the mechanics of laminate composites composed of soft elastomers and semicrystalline plastic under large deformation conditions.

Polyethylene (PE), like the grocery bag material in Figure 1B, is one of the most widely used polymers in the world (Malpass, 2010). PE is cheap(Pascu, 2005), has good processability(Pascu, 2005), has chemical resistance(Pascu, 2005) and is bio-compatible(Fouad & Elleithy, 2011). PEs are used for pipe and fittings applications (Nguyen et al., 2021), biomedical applications (Fouad & Elleithy, 2011), and others (L. Wang, Isaac, Wilcox, Jones, & Thompson, 2019). Additionally, thin polyethylene films are extensively used in the packaging industry (Nisticò, 2020). The inhomogeneous deformation exhibited by the grocery bag in Figure 1B is called cold drawing(Carothers & Hills, 1932). Cold drawing polymers undergo strain localization beyond tensile yield stress, typically at a small, applied strain, forming a neck upon further loading. However, for this class of materials, the strain localization does not necessarily imply ductile failure. Instead, the deformation in the neck becomes stagnated(Argon, 2013a). Further deformation then progresses at constant engineering stress by the process of neck propagation, where the shoulder of the neck can be seen to be moving as the material outside the neck gets

drawn into the necked state. Upon unloading after tensile deformation, the specimen shows little recovery(Argon, 2013a).

During cold drawing in polyethylene, the deformation is concentrated at the propagating neck front. The immense strain gradient present at the neck font makes it a hotspot for stress triaxiality(G'Sell, Aly-Helal, & Jonas, 1983) in the geometry. Stress triaxiality is a measure of mean stress relative to effective stress. Large stress triaxiality has been found to be associated with ductile to brittle transition in such materials (Bao & Wierzbicki, 2004; El-Sayed, Barton, Abdel-Latif, & Kenawy, 2001; Han, Zhang, Xue, Zhou, & Liu, 2020). Furthermore, polyethylene films are known to exhibit limited flaw tolerance(Bartczak, Argon, Cohen, & Weinberg, 1999). Therefore, even though plastics like polyethylene can deform to large strains, they can easily fail at these hot spots.

Like semicrystalline plastics, soft elastic materials like elastomers(Lee et al., 2017) and gels(Calvert, 2009) can deform to large stretches, albeit recoverable and without necking. Beyond traditional uses in tires, gaskets, and adhesives, such soft materials are extensively studied for applications like soft robotics(Abdullah, Li, Braun, Rogers, & Hsia, 2018; Coyle, Majidi, LeDuc, & Hsia, 2018), stretchable electronics(Arafat, Dutta, & Panat, 2015, 2016) etc. Furthermore, unlike cold drawing plastics like polyethylene, soft elastic materials show good flaw tolerance (C. Chen, Wang, & Suo, 2017).

These excellent mechanical properties of the elastomer and its natural ability to undergo considerable deformation motivate the bonding of rubber to cold drawing plastics to modify the necking and failure behavior. However, there are additional incentives to layering rubber and plastic. Stretching of an elastic layer bonded to a plastic material creates elastic strain mismatch between the layers when the plastic yields. Elastic strain mismatch in laminate materials can induce

out-of-plane deformation. For example, the familiar bimetallic strips found inside a household thermostat use the elastic stain mismatch generated by incompatible thermal expansion to bend out-of-plane. Moreover, soft biological materials like tissues exploit growth-induced heterogeneous elastic strain to create a myriad of static shapes and dynamic mechanisms. Opening of seed pods by elastic incompatibility(Armon, Efrati, Kupferman, & Sharon, 2011), growing complex three-dimensional features in internal organs(B. Li, Cao, Feng, & Gao, 2011; Nelson, 2016), twisting of plant tendrils(Gerbode, Puzey, McCormick, & Mahadevan, 2012), curvatures in leaves(Liang & Mahadevan, 2009) and others(Katifori, Alben, Cerda, Nelson, & Dumais, 2010; Savin et al., 2011; Sharon & Efrati, 2010) are all examples of shape changes through inhomogeneous strain generation in soft materials. In this context, shape generation in rubber-plastic bilayer under large deformation is of interest.

1.1 Aim of the Thesis

Boding a rubber layer to plastically deforming material has been observed to retard the necking behavior in the plastic layer(T. Li et al., 2005). Furthermore, the bonding of a rubber layer has been shown to decrease the crazing in the plastic layer(Hachisuka, Kobayashi, & Yamaguchi, 2019) and thereby improve the material's stretchability. Elastic strain mismatch generated in elastic-plastic bilayer forms curved morphology, whose curvature increases with applied strain(Wisinger, Maynard, & Barone, 2019). While these report on the effect of bonding rubber to a plastically deforming material, there is little research done on rubber-plastic bilayers at large stretches.

The objective of this thesis is to study the large-deformation mechanics of layered composites of rubber and plastic. Specifically, this thesis examines necking and neck propagation and the fracture and process zone kinematics in layered rubber-plastic composites. Finally, this thesis also examines the morphologies generated from the large elastic strain mismatch in the rubber-plastic laminate system. The detailed objectives of each project are given below.

1.1.1 Necking and Drawing in Rubber-Plastic Laminates

The necking followed by stable neck propagation is studied in bilayers made from linear low-density polyethylene (LLDPE) as the plastic layer and styrene-ethylene/propylene-styrene (SEPS) as the rubber layer. A neck stretch-based scalar quantity is defined and experimentally measured to quantify the inhomogeneous deformation during neck propagation in LLDPE-SEPS bilayers. The rubber thickness required to avoid necking and neck propagation altogether is evaluated. Further, a clear understanding of the effects of the rubber modulus and the rubber strain hardening on the necking and drawing deformation is desired. To isolate these effects clearly, constitutive equations are adopted in which the low strain modulus, yielding behavior, and strain hardening can all be varied independently. A predictive analytical model based on the uniaxial first Piola-Kirchhoff stress is developed and validated using finite element simulations. The analytical model can be practically useful for design purposes, e.g., rapidly estimating the rubber/plastic ratio needed to eliminate necking or estimating the maximum stress experienced in each layer. This portion of the research is published in two papers(R. G. Ramachandran et al., 2018; Rahul G. Ramachandran, Maiti, & Velankar, 2020).

1.1.2 Fracture of Rubber-Plastic Laminates

Among polyethylene polymers, HDPE has the least toughness(Choi et al., 2010). Hence the effect of rubber addition on the fracture of cold drawing plastics is studied on trilayers films prepared from High-Density Polyethylene (HDPE) as the plastic layer and SEPS as the rubber layer. First, the flaw tolerance of the HDPE-SEPS trilayer with SEPS fraction is quantified experimentally. Fracture tests are performed on HDPE and HDPE-SEPS trilayer films with concurrent video capture of the process zone deformation. The objective of the fracture experiment is to capture the effect of rubber fraction on the process zone formation, growth, and crack initiation. Complementary finite element simulation explains the change in crack initiation, process zone size, and propagation with rubber fraction in the composite. This portion of the research is still yet to be submitted for publication

1.1.3 Morphology in Rubber-Plastic Laminates

Uniaxially stretching a rubber-plastic bilayer composite beyond its yield point can create an elastic strain mismatch between the two layers. Upon release, it is often observed that the bilayer then bends out-of-plane. Literature on shape changes from elastic strain mismatch generated in a rubber-plastic system has followed an elastic-after-release approach. However, In the LLDPE-SEPS trilayer system, it is observed that large stretching beyond a critical stretch cause formation of surface wrinkles during unloading(Yang, Damle, Maiti, & Velankar, 2017). Hence the validity of the elastic-elastic approach needs re-examination. Further, the shape generation in rubber-plastic bilayer systems at large applied stretches has not been explored.

The experimental portion of this research involved the preparation of Natural Rubber (NR)-LLDPE bilayers of various rubber plastic ratios. Multiple samples of the same rubber-plastic ratio were stretched and released to allow for shape formation to capture the shapes formed with increasing applied stretch. The test was conducted for various rubber-plastic ratios as well various aspect ratios to capture the effect of these geometric parameters on the shape formed. Finally, a single layer energy-based saddle model considering the aspect ratio as well as the thickness of the rubber was developed to correlate the imposed strain mismatch on the final shape formed. This portion of the research has been published(Rahul G. Ramachandran, de Cortie, Maiti, Deseri, & Velankar, 2021).

2.0 Necking and Drawing in Rubber Plastic Laminates

2.1 Introduction

Different types of materials can show qualitatively distinct behaviors under tensile stress. If a bar or rod of an elastomeric material with uniform cross section is pulled, it tends to stretch uniformly with a correspondingly uniform decrease in thickness. This is our common experience with a rubber band which stretches homogeneously even when stretched to many times its original length. Another class of materials such as metals and many polymers develop a *necking instability* in tension, i.e. an initially-uniform sample, post yielding, shows strong strain localization. As a result, the material thins locally at the necked region until it fails(Courtney, 1990c). However, necking need not necessarily lead to failure. In materials such as some semi-crystalline or glassy polymers, the neck stabilizes and spreads by recruiting new material into the necked region, which is indicative of post-yield strain hardening(Argon, 2013a; I. M Ward, 1971a). For example, Figure 1a shows such behavior in polyethylene, discussed later. Such a material behavior where deformation proceeds by neck propagation is called *stable drawing* or *cold drawing* a term originally introduced by Carothers and Hill(Wallace H. Carothers, 1932).

Stability of deformation at the neck is governed by the post-yield constitutive response of the material(Coates & Ward, 1980; I. M Ward, 1971b). A commonly-used constitutive model to describe the material response in strain hardening materials in tension is $\sigma = K\epsilon^n$, where σ is the true stress, ϵ the true strain, and K and n are constitutive parameters(Courtney, 1990b). Typically, the value of n for ductile metals is around 0.5 or less(G. E. Dieter, 2003). Therefore, for strains exceeding a few percent, these materials show a gentle rise in stress with strain. Since the load

bearing capacity of the neck is decreasing with every strain increment, the material is expected to fail by local thinning. In contrast, the polymers capable of cold drawing show a highly non-linear, asymptotic increase in true stress with strain(Hutchinson & Neale, 1983; I. M Ward, 1971b).Such a strain hardening behavior would restrict further deformation in the necked region due to the increasing stress increment required for stretching and thereby stabilizing the neck. This type of highly non-linear strain hardening is common in a wide variety of materials, e.g. soft tissues(Fung, 1993), elastomers(I. M. Ward, 1971), or semi-crystalline polymers(I. M Ward, 1971a).

The central concern of this paper is the behavior of composite laminates in which a layer of a cold drawing plastic is bonded to a layer of elastomer. Since cold drawing plastics show stable necking whereas elastomers stretch homogeneously, it is reasonable to expect that rubber-plastic composites would show intermediate behavior. Mechanics of bilayer laminates of metals and elastomers bonded together, where the metal layer exhibits strong post-yield strain localization, have been studied by Li and Suo(T. Li & Suo, 2006). Upon stretching under plane strain conditions, the yielding layer (by itself) developed a single neck which failed upon further stretching. In contrast, the elastomer (by itself) showed uniform thinning and stretching. Laminate composites with sufficiently large rubber layer thickness or stiffness were predicted to thin homogeneously to large strain. This is interesting because bonding an elastomer allowed a plastic layer (which would ordinarily fail at a small strain by necking) to be stretched to a high strain without failure. Indeed, this situation – the experimental(Macionczyk & Bruckner, 1999; Xiang, Li, Suo, & Vlassak, 2005) and numerical observations(T. Li et al., 2005){Hutchinson, 1983, NECK PROPAGATION} that metal films bonded to elastomers could be stretched in a ductile fashion up to a high strain – was the motivation for their research(T. Li & Suo, 2006) and subsequent research on this topic(Andreasson, Kao-Walter, & Ståhle, 2014; Arafat et al., 2015,

2016; Ben Bettaieb & Abed-Meraim, 2017; Jia & Li, 2013; Lacour, Chan, Wagner, Li, & Suo, 2006; T. Li & Suo, 2007; Liu, He, Chen, Leow, & Chen, 2017; Xue & Hutchinson, 2007, 2008; Yang et al., 2017). However, that research was restricted to cases such as metal-rubber composites in which where the plastic layer (metal) could not show stable drawing. The situation when the plastic layer of the composite is a strain hardening polymer that is capable of stable drawing is likely to be quite different. The goal of this article is to explore the modification of necking and drawing behavior when such a stable drawing polymer is bonded to an elastomer.

An example illustrating the main issues of interest in this paper is shown in Fig. 1 which compares the tensile deformation behavior of a plastic layer, a rubber layer, and a rubber-plastic bilayer laminate composite. Here we will only discuss the qualitative aspects briefly; the quantitative details will be discussed later in this paper. Fig. 1a shows the behavior of a film of linear low-density polyethylene (LLDPE) plastic which develops a neck at a modest deformation, followed by stable drawing during which the necked region grows by recruiting new material into the neck. During stable drawing, neither the necked region nor the material outside the neck deforms significantly. Instead, deformation is confined to a very narrow transition zone (which appears as a sharp line in the images) between the necked and un-necked regions. Fig. 1b shows a sample of styrene-ethylene/propylene-styrene (SEPS) rubber, and in sharp contrast to the LLDPE, the SEPS deforms homogeneously with no indication of any localized stretching. Finally Fig. 1c shows a bilayer laminate composite of the SEPS:LLDPE in the thickness ratio of 1.2:1. The behavior is intermediate between the rubber and the plastic: while the sample does undergo necking, the transition between the necked and un-necked region is not as sharp (this is especially clear in the videos, *LLDPE.avi*, *SEPS.avi* and *Bilayer.avi*, available as ESI), and we will show later that the magnitude of strain localization is reduced as compared to Fig. 1a. In this paper we

explore this situation quantitatively and address the extent to which the necking behavior is modified and how this depends on rubber thickness.

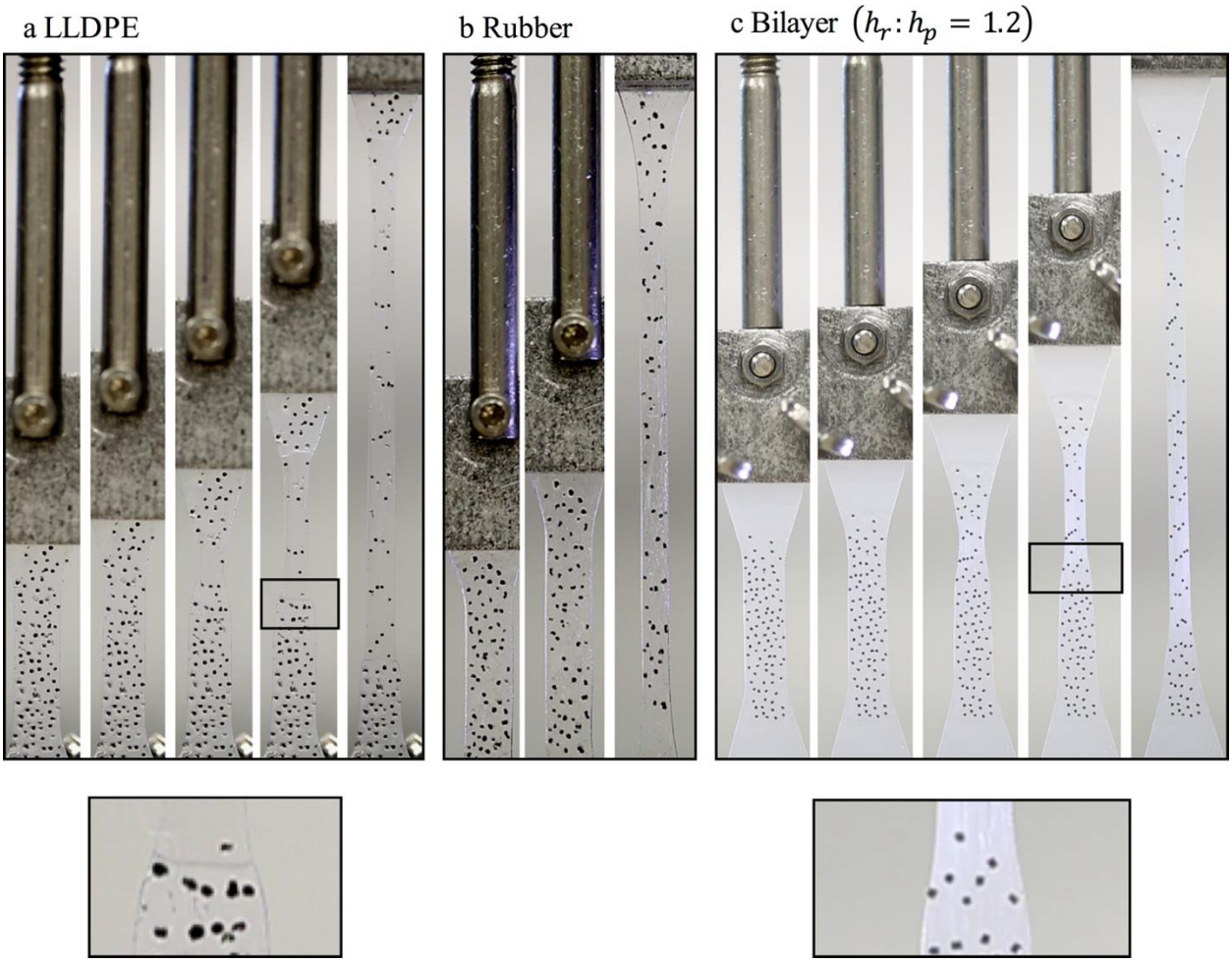

Figure 2: Images of samples during tensile deformation of dog bone-shaped samples of (a) LLDPE plastic, (b) SEPS rubber, (c) rubber-plastic laminate composite with a 1.2:1 rubber:plastic ratio. Black dots are marker particles. Lower two images are magnified view showing the sharp neck of LLDPE and more diffuse neck of the composite. Videos of (a-c) are available as ESI.

2.2 Methods

2.2.1 Experimental

Most of the details of experimental methods are given in the Electronic Supplementary information. Briefly, bilayer laminate samples were prepared by bonding LLDPE films to SEPS rubber films using compression molding. Most of the samples have a nominal plastic layer thickness of 120 μm, whereas a few samples have a nominal plastic layer thickness of 50 μm. 50 μm thick plastic layer was used to achieve large rubber:plastic thickness ratios. Dog-bone shaped samples (6 mm width and a nominal gauge length of 20 mm) were cut from the resulting bilayer composite sheet. Small black particles were then stuck onto this surface (rendered sticky with silicone oil) to serve as markers for Digital Image Correlation (DIC). Tensile testing was conducted at a crosshead speed of 120 mm/min and video-recorded. The two layers remained fully bonded to each other during tensile deformation (and indeed remained bonded after releasing, causing the plastic layer to develop intense wrinkles(Yang et al., 2017)). Similar experiments were conducted on the SEPS and the LLDPE layers individually; the ESI explains how residual orientation of the LLDPE film was relaxed prior to experiments.

2.2.2 Stretch Mapping by DIC

Since the deformation of the samples was not always uniform along its length, the stretch profile on the sample surface was computed for quantifying deformation. A finite element based interpolation technique was used to estimate the evolution of the stretch distribution with time on the sample surface by tracking the position of the finite number of marker points. Typical

distribution of the marker particles (the black dots) on the samples can be seen from Fig. 1. Marker positions were tracked at each frame of the recorded video of the specimen deformation by using Blender™ (Stitching Blender Foundation, Amsterdam, Netherlands) software suite. The marker positions from the first video frame was triangulated to construct the reference configuration, which was a 2D finite element mesh of three-noded triangles with nodes located at the marker locations. The markers locations were triangulated by Delaunay triangulation technique by making using of the opensource software Triangle (Computer Science Division, University of California at Berkeley). Fig. 2 shows examples of the initial reference configuration (Fig. 2a), and the deformed configuration at some later instant (Fig. 2b) for an LLDPE sample, superimposed on the corresponding images.

The stretch map was generated by evaluating the stretch in the axial direction of each triangular element at their corresponding integration point and then averaging them at nodes(Logan, 2007). The process was repeated at all frames of the video recording to generate the stretch evolution with time, on the sample surface. Calculations involved in calculating the stretch map are described in ESI. An example of the stretch maps as a function of time is shown as ESI video LLDPE_Stretch_Map.avi.

Fig. 2c shows the calculated stretch map superimposed onto the image of the deformed specimen of Fig. 2b. Overall the local deformation of the sample is very well-captured by the color maps. Yet, we acknowledge that at the transition between the necked and un-necked region, agreement is much poorer. Specifically, the experimental image shows a sharp transition, whereas the color map appears much smoother. This is because our continuum mechanics based DIC algorithm cannot capture displacement discontinuities arising at the sharp transition fronts. Increasing the area density of the markers would allow displacement discontinuity at the transition

front to be represented as a sharp gradient. Thus, the analysis below will only use the maximum and minimum values of stretch, with no further comment on the sharpness of the transition.

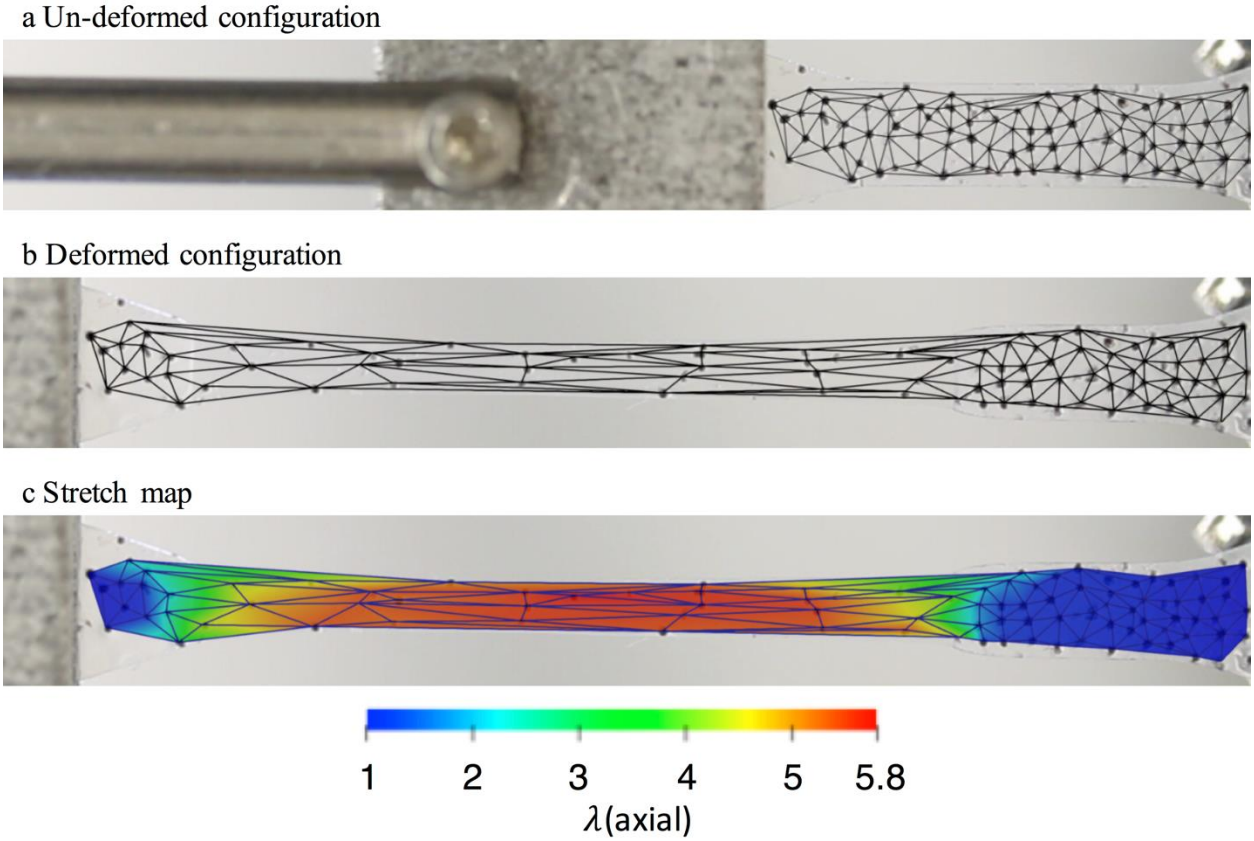

Figure 2: Mesh generated by triangulating the marker locations superimposed over the corresponding frame of the recorded video in (a) the initial configuration is (b) deformed configuration. (c) The stretch map corresponding to (b).

2.3 Results

2.3.1 Mechanical Behavior of LLDPE/SEPS Bilayer

We start with discussing the force data measured during tensile testing experiments (the corresponding videos are discussed in the Section 2.3.2). Fig. 3a shows the nominal stress strain response of pure LLDPE plastic, SEPS rubber and laminate composites with two different rubber:plastic thickness ratios. Here the nominal strain is defined as the ratio of the crosshead displacement to the gauge length (20 mm). The free-standing LLDPE plastic and the two rubber-plastic bilayer laminates in Fig. 3 all have the same nominal plastic layer thickness of 120 microns. The stress-strain curve for the SEPS rubber increases monotonically. In contrast, the LLDPE plastic shows a sharp rise in stress at small strain, followed by a peak which is generally associated with the onset of neck formation. More specifically, since the neck has a smaller cross-sectional area than the original sample, the total force reduces upon neck initiation, and so does the nominal stress. Since the decrease in nominal stress is primarily attributable to a decrease in cross sectional area at the neck, it is sometimes called *geometric softening*(Bower, 2010). The load however does not continue reducing indefinitely. Instead it reaches a minimum value that corresponds to the onset of stable drawing. Then the stress rises gently over a wide range of nominal strain over which the necked region propagates across the entire sample. Once the neck reaches the wider ends of the dog-bone shaped specimen, the nominal stress rises again.

The behavior of the composites is qualitatively similar to that of the plastic, but with the key difference that the peak is much less sharp. To emphasize the difference between the layered composites vs the LLDPE in the peak region, Fig. 3b plots the same results, but in the form of

load-elongation curves at small strain. These measured curves are compared against the simplest model of a layered composite, which is to treat the total force as a sum of the force in each layer:

$$F_{bilayer} = F_r + F_p = w\left[h_r\sigma_{nom,r} + h_p\sigma_{nom,p}\right] \quad (2.1)$$

where h_r and h_p are the rubber and plastic layer thickness respectively, w is the sample width, and $\sigma_{nom,r}$ and $\sigma_{nom,p}$ are the nominal stresses for the rubber and plastic measured independently at the same nominal strain (i.e. same crosshead displacement). The predictions of Eqn. 2.1 are shown in Fig. 3b as dotted lines. This comparison makes it clear that for both the laminate composites shown, the experimentally-measured peak is much less sharp than predicted by Eqn. 2.1. Furthermore, for $h_r/h_p = 4.0$, the force-strain curve shows no apparent peak. Since the presence of a peak is associated with necking, the force data alone suggest that the degree of necking decreases with increasing rubber thickness, which will be considered next.

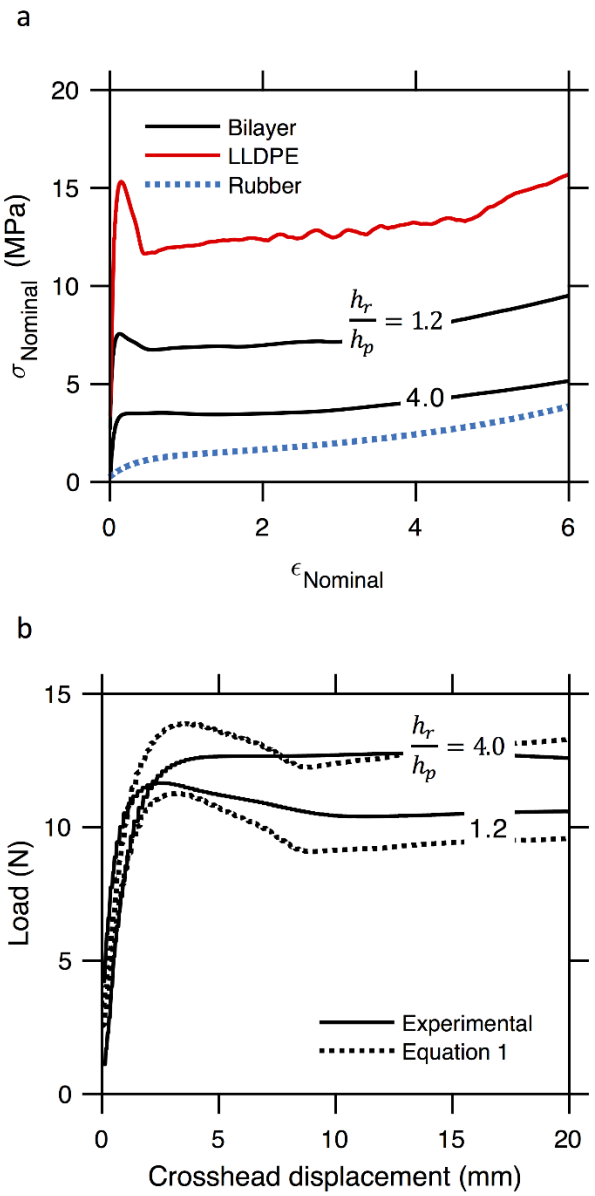

Figure 3: (a) Nominal stress-strain response for rubber, LLDPE, and LLDPE - rubber bilayers of rubber:plastic thickness ratio 1.2 and 4.0 stretched at a rate of 120 mm per minute. (b) The same data as the composites in (a) but shown as force vs crosshead displacement. Only the small-deformation region is shown in (b) Dotted lines are Eqn. 2.1.

2.3.2 Qualitative Behavior of Tensile Deformation

Fig. 4 shows the stretch maps of LLDPE, SEBS rubber, and a rubber-plastic laminate composite. The crosshead displacements for each of the images is listed below the image. The LLDPE, initially deforms uniformly (second frame shown in Fig. 4a), followed by necking (evident as the green region with higher stretch in the third frame). With further crosshead displacement, the stretch in the neck first increases, but eventually (last two frames in Fig. 4a) it saturates as judged by the similar intensity of the red color in the last two frames. Beyond this point, further crosshead displacement is accommodated purely by drawing un-necked material into the neck, with no further change in the necked region.

In sharp contrast, the rubber (Fig. 4b) stretches uniformly, as judged by the nearly uniform color at all deformation stages, with the stretch increasing steadily with crosshead displacement.

The behavior of LLDPE – rubber bilayer with $h_r/h_p = 1.2$ (Fig. 4c) is qualitatively similar to that of the LLDPE: the initial deformation is homogeneous, followed by necking and then drawing. The chief difference is that the maximum stretch developed in the necked region saturates at a much lower value than the LLDPE. Accordingly, towards the end of the stretching experiment, the neck propagates throughout the test section of the sample, and hence the deformation reverts to becoming homogeneous. The electronic supplementary material Fig. S1a,b shows stretch maps for two other rubber:plastic thickness ratios (2.4 and 4.0). At a ratio of 2.4, the behavior is qualitatively similar to Fig. 4c. At a ratio of 4.0, the necking behavior is much more subtle; variations in stretch across the length of the test section remain relatively small (albeit larger than the SEPS rubber in Fig. 4b) throughout the experiment.

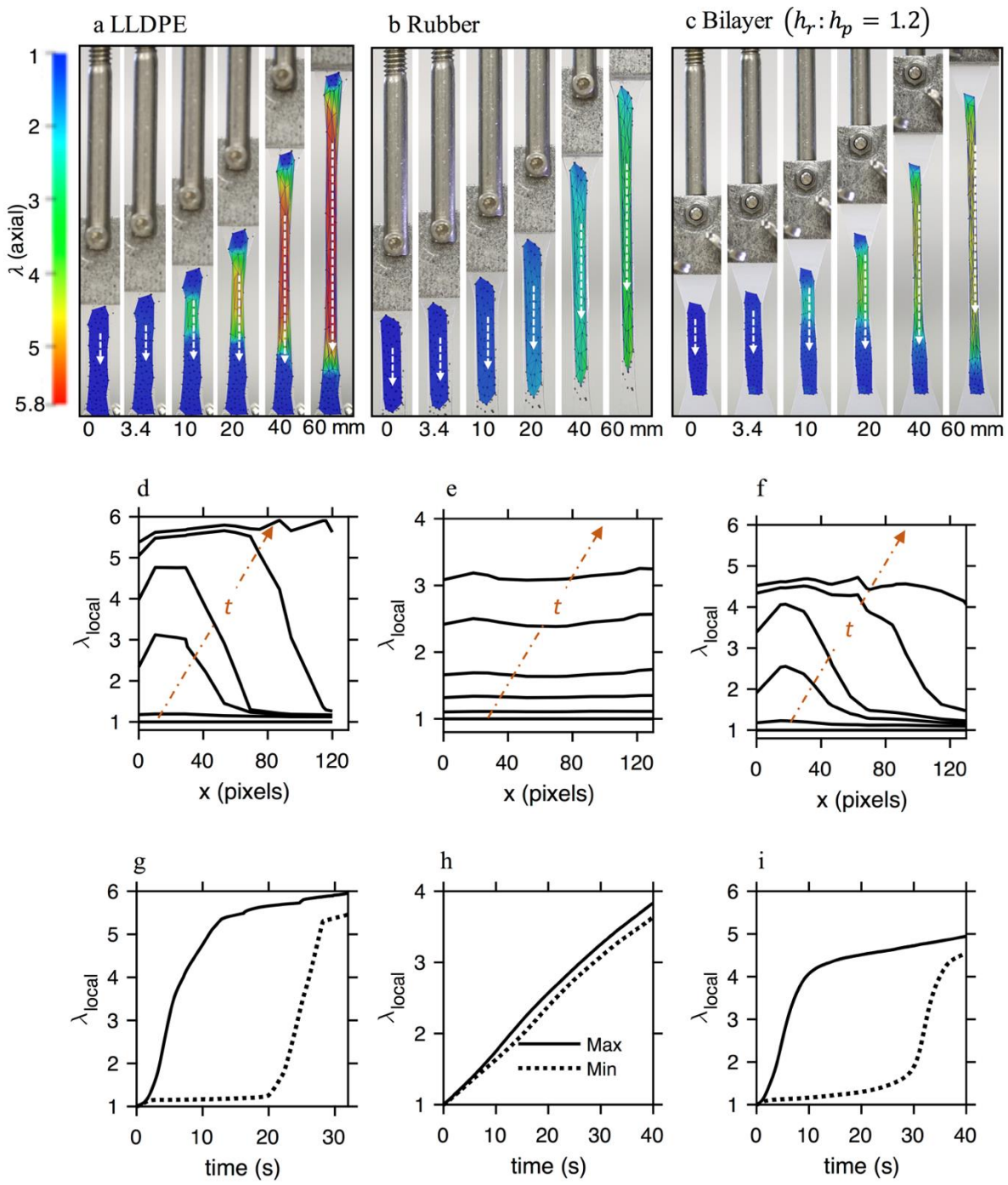

Figure 4: (a,b,c) Stretch maps superimposed on corresponding specimen configurations for (a) LLDPE plastic, (b) SEPS rubber, (c) bilayer composite with rubber:plastic thickness ratio of 1.2. Number below each image is the crosshead displacement. (d,e,f) plot stretch data extracted along the white dashed lines in (a,b,c) against the pixel coordinate along the line in the undeformed configuration. (g,h,i) show maximum and minimum stretches vs time along the white dashed lines in (a,b,c).

2.3.3 Quantifying Inhomogeneous Deformation

We now proceed with a more quantitative analysis. Since the deformation of the samples is predominantly uniaxial, most of the insights about the heterogeneity of sample deformation can be obtained from examining the stretch along the stretching direction only. Accordingly, the stretch was extracted along the center line in the gauge section of the dog-bone as illustrated by the dashed lines in Fig. 4a-c. Therefore, these dotted lines are the region of interest (ROI) for quantitative analysis. The end-points of these lines were chosen to ensure that the transition from the un-necked to the necked region could be followed unambiguously, while still avoiding the wider ends of the dog-bone shaped specimen. The stretch profiles along the centerline for the samples of Fig. 4a-c are shown in Fig. 4d-f respectively. In these plots, the abscissa indicates the location (in pixels) along the dashed lines, whereas the ordinate axis shows the corresponding axial stretch at that location (λ_{local}). These plots now quantify all the features discussed in the previous section. The LLDPE (Fig. 4d) shows necking, followed by drawing, with the stretch saturating at roughly 5.7. This value can be regarded as the natural draw ratio of this LLDPE, defined as the steady state stretch at which the neck stabilizes for a cold drawing plastic(I. M Ward, 1971a). The rubber sample (Fig. 4e) shows a monotonic increase in stretch, but with little spatial variation with position at any instant. The composite laminate (Fig. 4f) with rubber:plastic thickness ratio 1.2 behaves similarly as the LLDPE, but with the stretch saturating at roughly 4.5.

As a quantitative measure of the degree of heterogeneity in the deformation, we extract the maximum and minimum stretch, λ_{max} and λ_{min} at all stages of deformation for each sample. Figs. 4g-i plot these extreme values for each of the three samples of Fig. 4a-c throughout the deformation. Fig. S1c&d in the ESI plots the same for bilayers of rubber:plastic thickness ratio 2.4 and 4.0.

To facilitate comparisons of the various samples, Fig. 5a plots λ_{max} vs λ_{avg}, where λ_{avg} is the average stretch in the ROI. Fig. 5a includes all the three samples of Fig. 4 as well as bilayer laminates with two additional thickness ratios shown in the supplementary Fig. S1. The degree of non-homogeneity of deformation can be readily identified from this plot as deviations from the $\lambda_{max} = \lambda_{avg}$ line. For the SEPS rubber, the data remain close to the $\lambda_{max} = \lambda_{avg}$ line throughout the deformation indicating near-homogeneous deformation. All the other samples deviate from the $\lambda_{max} = \lambda_{avg}$ line, with deviations becoming more severe as the rubber thickness decreases. Furthermore, samples with small rubber thickness show a near plateau in λ_{max} whose value is the natural draw ratio. In contrast, samples with $h_r/h_p = 4.0$, λ_{max} shows a steady increase during the deformation. This implies that there is no stable drawing regime, and one cannot identify a single value as a natural draw ratio.

It would be convenient to have a single numerical metric to quantify the degree of non-homogeneity of deformation. The most convenient metric for this purpose would be the plateau in λ_{max} because it has immediate physical significance as the natural draw ratio. Yet, the λ_{max} plateau is not an ideal metric because at large rubber thickness, the data do not show a plateau at all. Furthermore, Figs. 4f, and Fig. S1c&d all show that λ_{min} itself increases indicating that the non-homogeneity of deformation reduces during the deformation process. Ideally, we would prefer a metric that can capture the changes in both λ_{max} and λ_{min}. One simple approach is to take the ratio $\lambda_{max}/\lambda_{min}$. This quantity is plotted against λ_{avg} in Fig. 5b. We may now select any convenient average stretch and use the corresponding value of $\lambda_{max}/\lambda_{min}$ to quantify the degree of non-homogeneity. For instance, the dashed line in Fig. 5b shows $\lambda_{avg} = 3.5$, and the corresponding values of $\lambda_{max}/\lambda_{min}$ are plotted in Fig. 7a.

We acknowledge that the choice of $\lambda_{avg} = 3.5$ is arbitrary, and a different choce of λ_{avg} would give somewhat different values for $\lambda_{max}/\lambda_{min}$. For instance, ESI Fig. S2 shows $\lambda_{max}/\lambda_{min}$ at λ_{avg}=3, and the points at high rubber thickness are distinctly shifted with respect to Fig. 7a.

To avoid this arbitrariness, we define a new metric dubbed the *inhomogeneity index* as the highest value of $\lambda_{max}/\lambda_{min}$ during the entire deformation. Thus, the inhomogeneity index is the y-axis value of the open circles in Fig. 5b. These values of the inhomogeneity index are plotted in Fig. 7b as a function of the rubber:plastic thickness ratio. Both Fig. 7a and 7b show similar trends: the non-homogeneity of deformation reduces as rubber thickness increases.

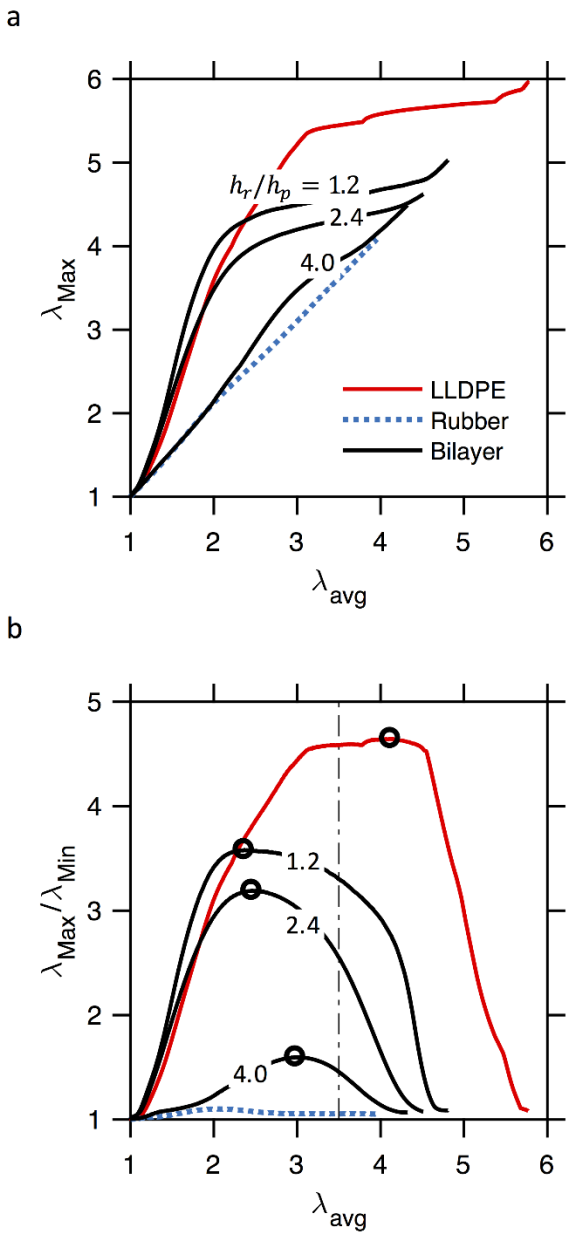

Figure 5: (a) Maximum stretch vs average stretch in the ROI, for a free-standing LLDPE, a free-standing SEPS and bilayer laminates of rubber:plastic thickness ratio 1.2, 2.4 and 4.0 (b) Same samples as in Fig. 5 (a), but with maximum to minimum stretch ratio plotted against average stretch in the ROI. The maximum of each curve, indicated with an open circle, is defined as the inhomogeneity index. The dot-dashed line corresponds to an average stretch of 3.5.

2.4 Discussion

To summarize the main experimental observations: tensile behavior of the LLDPE plastic is characterized by necking, followed by stable drawing, and a sharp transition between the necked and un-necked zone. Once stable drawing is realized, the natural draw ratio in the necked region is roughly 5.7, whereas the un-necked region is nearly undeformed (stretch of about 1.1).

Composites of the LLDPE plastic and the SEPS rubber show the following features: decrease in the stretch of the necked region; an increase in the stretch of the un-necked region; and an increase in the width of transition between the necked and un-necked region. In some cases, the necked region reaches the wider ends of the dog-bone shaped sample, therefore the deformation in the sample reverts to being uniform across the entire sample.

The remainder of this discussion is split into two sections. The first develops a simple model that captures many of the experimental observations. The second discusses possible refinements and limitations of the model along with other noteworthy issues.

2.4.1 Force-additive Rule of Mixtures Model

The overall goal of the model is not a detailed description of deformation, but a minimal description that captures most of the above observations. The analysis is based on the following assumptions. The first is Eqn. 2.1, that the force developed in the bilayer is simply the sum of the force in the plastic and the rubber layers measured independently at the same crosshead displacement. This is equivalent to assuming that the two layers are not bonded to each other, but simply deforming in parallel. We will comment further on this assumption at the end of this section, but Fig. 3b suggests that – despite the difference in the sharpness of the peak in the stress

strain curve – Eqn. 2.1 is reasonably correct. The second assumption is to ignore the transition region between the necked and un-necked regions. Thus, a sample can have at most two values of stretch that coexist at any instant. Finally, we adopt the simplest constitutive models that capture the qualitative behavior of the individual layers. For the rubber, a two parameter Mooney Rivlin hyperplastic constitutive relation was found to capture the rubber behavior reasonably well. For uniaxial deformation, the corresponding nominal stress is given by,

$$\sigma_{nom,r} = 2\left(C_{1,r} + \frac{C_{2,r}}{\lambda}\right) \times \left(\lambda - \frac{1}{\lambda^2}\right) \qquad (2.2)$$

The values of $C_{1,r} = 0.305\,MPa$ and $C_{2,r} = 0.360\,MPa$ were found by fitting the measured data for the SEPS rubber. We note that setting $C_{2,r} = 0$ reverts to the simpler neo-Hookean model, but this gave poor fits to the measured SEPS rubber data.

The plastic behavior is approximated by a two-parameter model previously employed by Haward to describe the behavior of a wide variety of thermoplastics (Haward, 1993). In Haward's approach, the stress in the LLDPE is assumed to be sum of a yield stress and incompressible neo-Hookean stress:

$$\sigma_{nom,p} = \frac{\sigma_{yield}}{\lambda} + 2C_{1,p} \times \left(\lambda - \frac{1}{\lambda^2}\right) \qquad (2.3)$$

This model has the obvious shortcoming that the stress has a discontinuity at zero strain, and hence mechanical behavior prior to yielding cannot be captured. Nevertheless, this model provides a simple analytical approach to quantify necking and drawing behavior. The yield stress (σ_{yield}) of LLDPE was taken to be the peak stress in the experimental nominal stress stretch curve and assigned a value of 16.8 MPa which is an average from multiple specimens. The $C_{1,p}$value was obtained as follows. As per the mathematical form of Eqn. 2.3, in a tensile experiment, the sample yields at λ=1 once the yield stress is exceeded. The subsequent behavior depends on the

value of $C_{1,p}$. For $2C_{1,p} > \sigma_{yield}/3$, the nominal stress increases monotonically with stretching. In contrast, for $2C_{1,p} < \sigma_{yield}/3$, the nominal stress first reduces and then increases at high stretch (see Fig. 6a). The latter must be true for LLDPE because non-monotonic behavior of the nominal stress-stretch relationship is necessary to see necking. The natural draw ratio then depends on the subsequent rise of the nominal stress at high stretch. One approach to calculating the natural draw ratio from the $\sigma_{nom,p}(\lambda)$ was provided by the Maxwell equal area construction as described by Hutchinson *et al*(Hutchinson & Neale, 1983). The construction is shown in Fig. 6a as a black dashed horizontal line drawn such that the two closed areas between the dotted line and the stress-stretch curve are equal. The idea is derived from the fact that as a material point transforms from an un-necked region to necked region, the work done by the applied force must equal the change in energy in the material:

$$\sigma_{draw}(\lambda_{neck} - \lambda_{unneck}) = W_{neck} - W_{unneck} \qquad (2.4)$$

where λ_{neck} is the stretch corresponding to the necked region, i.e. the natural draw ratio, λ_{unneck} is the stretch corresponding to the region that has not yet necked, and σ_{draw} is the nominal stress corresponding to stable drawing called *draw stress*. Since the constitutive behavior of Eqn. 2.3 gives yielding and neck initiation at $\lambda_{unneck} = 1$, we have $W_{unneck} = 0$. This implies,

$$\sigma_{draw}(\lambda_{neck} - 1) = W_{neck} \qquad (2.5)$$

where,

$$W_{neck} = \int_{1}^{\lambda_{neck}} \sigma_{nom,p}(\lambda)\ d\lambda = \ln(\lambda_{neck}) + 2C_{1,p}\left\{\frac{\lambda_{neck}^2 - 1}{2} + \left(\frac{1}{\lambda_{neck}} - 1\right)\right\} \qquad (2.6)$$

Moreover, since the stress for drawing is simply the nominal stress corresponding to the necked region,

$$\sigma_{draw} = \sigma_{nom,p}(\lambda_{neck}) = \frac{\sigma_{yield}}{\lambda_{neck}} + 2C_{1,p}\left(\lambda_{neck} - \frac{1}{\lambda_{neck}^2}\right) \quad (2.7)$$

Since $\sigma_{yield} = 16.8\ MPa$ and $\lambda_{neck} = 5.7$ is already known, we can combine Eqs. 2.5-2.7 to find $C_{1,p}$ explicitly:

$$C_{1,p} = \frac{\sigma_{yield}\left\{\ln(\lambda_{neck}) + \frac{1}{\lambda_{neck}} - 1\right\}}{\lambda_{neck}^2 - 2\lambda_{neck} + 2\frac{1}{\lambda_{neck}^2} + 3} \quad (2.8)$$

The value of $C_{1,p}$ thus calculated is 0.635 MPa. Incidentally, with this value for $C_{1,p}$, Eqn. 2.7 predicts $\sigma_{draw} = 10.2$ MPa, which underestimates the measured value of roughly 13.7 MPa. We will comment on this later.

The rule of mixture as given by Eqn. 2.1 can now predict the behavior of the bilayer. For convenience the bilayer force is normalized by the undeformed cross-sectional area of the plastic layer:

$$\frac{F_{bilayer}}{wh_p} = \frac{h_r}{h_p}\sigma_{nom,r} + \sigma_{nom,p} \quad (2.9)$$

Note that although the left-hand side in Eqn. 2.9 has units of stress, it does not represent the stress at any physical location; it is simply a convenient way of normalizing the force. Eq. 9 is plotted in Fig. 6b using the constitutive parameters already determined, for various values of h_r/h_p. It is clear that for large rubber thicknesses, the force vs stretch curve is monotonic, and hence necking is not expected. For $h_r/h_p < 3.25$, the force vs stretch curve has a minimum and hence necking is expected. Similar to the free-standing plastic, Eqn. 2.3 also shows yield at $\lambda = 1$,

i.e. the model predicts that the undrawn portion of the bilayer laminates is completely undeformed, and $\lambda_{unneck} = 1$. The draw ratio for the bilayer laminates can then be found numerically from the Maxwell equal area construction which can now be compared against experiments.

In fact, it is difficult to compare the draw ratio against experiments directly. This is because at large rubber thicknesses, the maximum stretch λ_{max} in the necked region does not show a plateau (Fig. 5a), so a single unique draw ratio is difficult to identify. Therefore, we compare the model against the two measures of non-homogeneity of deformation discussed in Section 2.3.3: the ratio $\lambda_{max}/\lambda_{min}$ obtained at $\lambda_{avg} = 3.5$ (Fig. 7a) and the inhomogeneity index (Fig. 7b). For the model described the value for comparison is simply $\lambda_{neck}/\lambda_{unneck} = \lambda_{neck}$. The corresponding comparisons shows reasonable agreement with the experimental quantification of inhomogeneity at low rubber thicknesses, but not at large rubber thicknesses. Specifically, the model predicts that necking is eliminated for $h_r/h_p > 3.25$, whereas significant inhomogeneous deformation is still evident at larger values of rubber thickness. Indeed, experimentally we were not able to completely eliminate necking even at the highest rubber thickness examined.

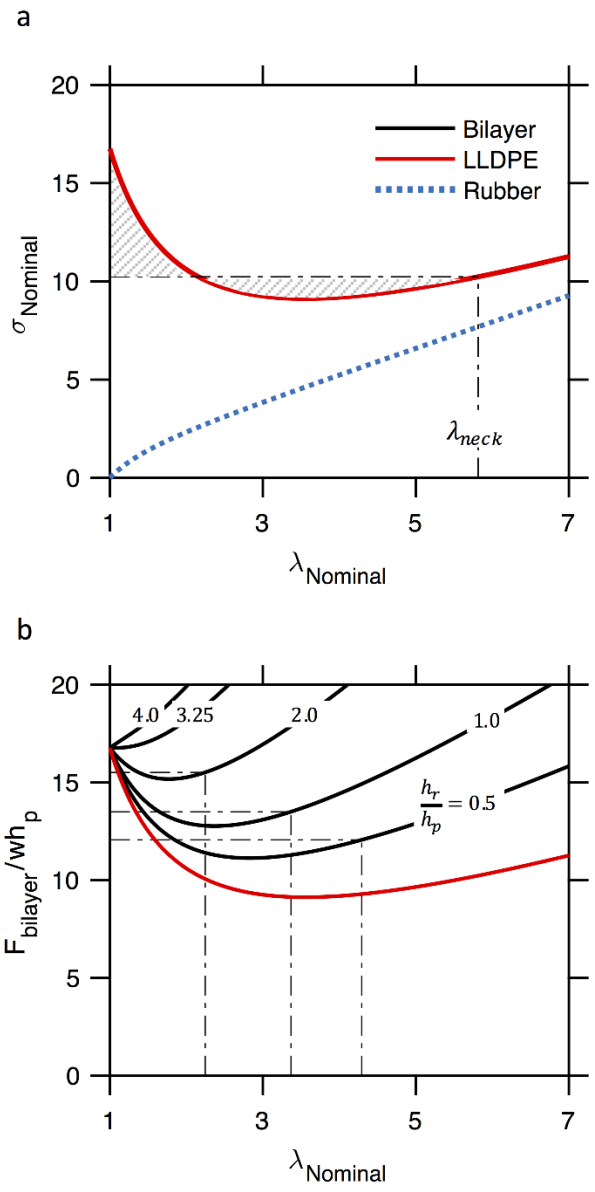

Figure 6: (a) Constitutive behavior of SEPS and LLDPE approximated by Eqn. 2.2, 2.3 respectively. The black dot-dashed line is the Maxwell line construction where the shaded areas are equal. (b) Solid black lines are predictions of Eqn. 2.9 for the various rubber:plastic ratios indicated. Solid red line is the LLDPE behavior, same curve as (a). Horizontal dot-dashed lines are Maxwell constructions for each rubber:plastic ratio.

A second parameter of comparison is the draw stress from experiment against model predictions. Experimentally this is simply nominal stress value corresponding to the onset of stable

drawing, which is the local minimum in the nominal stress strain curve post yielding. To obtain the predicted value of the draw stress, the force $F_{bilayer}$ is obtained from Eqn. 2.9 where $\sigma_{nom,r}$ and $\sigma_{nom,p}$ are evaluated by substituting the predicted values of λ_{neck} into Eqs. 2.2 and 2.3. The corresponding nominal stress is simply $F_{bilayer}/(wh_r + wh_p)$, and is shown as a solid line in Fig. 7c. The predicted nominal stress reduces from 10.2 MPa for the free-standing LLDPE to roughly 4 MPa for $h_r/h_p = 3.25$. Beyond this rubber thickness, the deformation is predicted to be homogeneous and it is not physically meaningful to define a draw stress. Fig. 7c plots the experimentally obtained draw stress with h_r/h_p and compares with predicted values. The draw stress is poorly predicted for pure LLDPE. Fortuitously, the draw stress is in much better agreement for the bilayer laminates. Overall, the trend of decrease in draw stress with increasing rubber thickness is qualitatively captured.

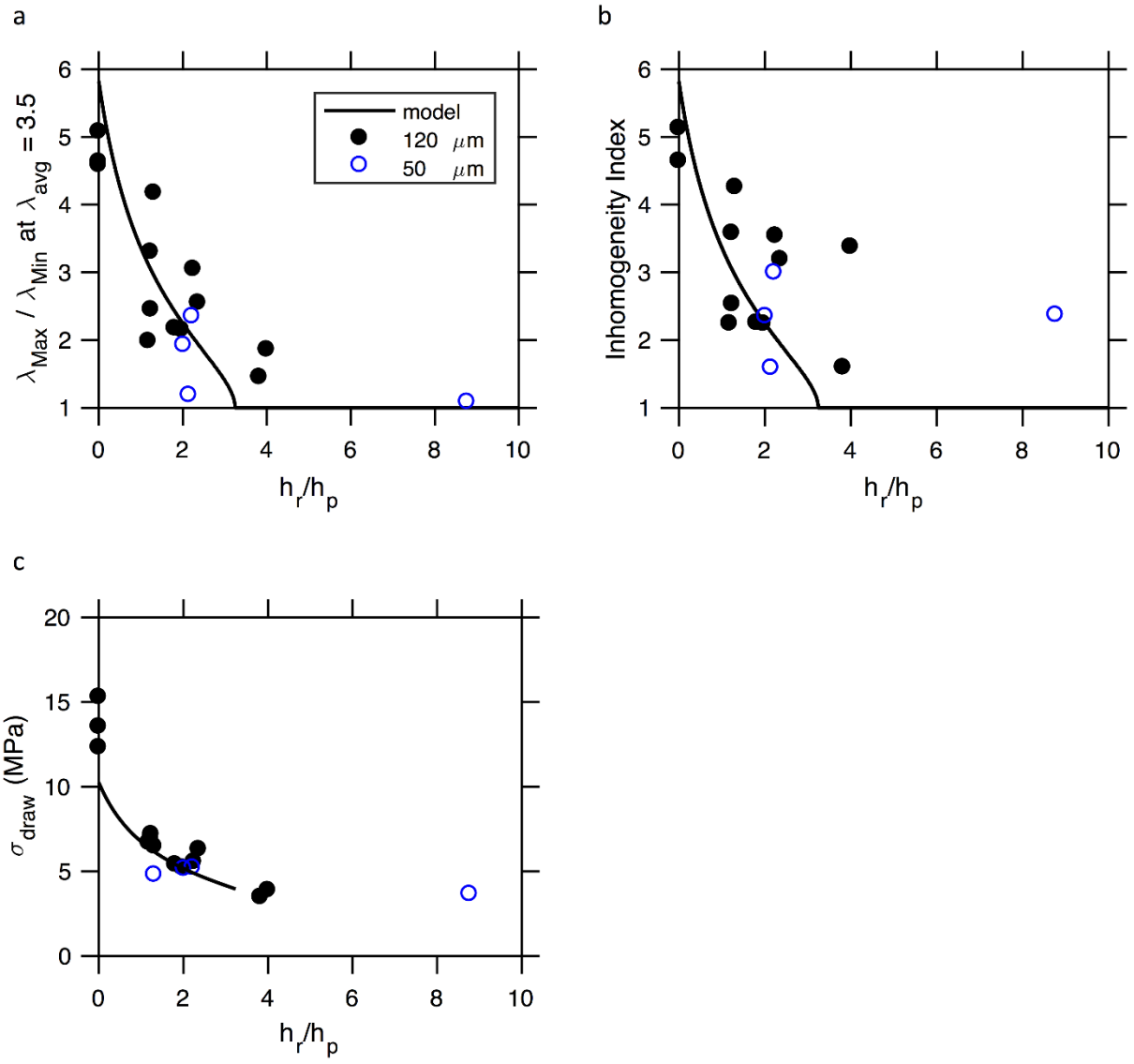

Figure 7: (a) Ratio of maximum stretch to minimum stretch in ROI, when the average stretch in ROI is 3.5 (b) Inhomogeneity index and (c) draw stress, all plotted vs rubber:plastic thickness ratio. Filled and open circles are bilayers with 120 micron and 50 micron plastic respectively. Solid lines are model predictions.

2.4.2 Limitations

Although very simple, the model appears to be qualitatively successful in capturing the decrease in the inhomogeneity of deformation (Fig. 7a&b) and decrease in the stress for stable

drawing (Fig. 7c). Quantitatively however, there are three significant discrepancies. First, the stress for stable drawing for the free-standing plastic is underpredicted by about 25%. Second, the plastic and the composites all yield at a stretch of 1, and hence one important experimental observation, that the onset of necking requires higher stretch for the laminate composites, is not captured even qualitatively. Finally, the model predicts that deformation is homogeneous for $h_r/h_p > 3.25$ whereas experimentally, deformation remains somewhat inhomogeneous even at the highest rubber:plastic thickness ratios examined.

Some these limitations may be addressed with a constitutive equation for the plastic layer that accounts for elastic behavior up to some finite strain prior to yield. Yet, even with this improvement, the above modeling approach may not be able to capture the experimental observations quantitatively for several reasons. First, Eqn. 2.1 treats the bilayer force as a sum of the force in the rubber and in the plastic when measured independently. Yet, when tested independently, the plastic undergoes necking whereas the rubber does not, and hence they are in an altogether different strain state. In a bilayer composite, since the layers are bonded, their strain state must be very similar. As one consequence, at small rubber thicknesses, the rubber layer in the necked region experiences a stretch that far exceeds that in the free-standing rubber. In the other extreme, at large rubber thicknesses when deformation is homogeneous, the plastic layer experiences a variety of strain states, whereas the free-standing plastic is mostly in just two states – necked ($\lambda \sim 5.7$) or un-necked ($\lambda \sim 1$). This fact – that in the bilayer each layer constrains the deformation of the other – affects the width-direction narrowing of the samples as well. Clearly then, the individual layers in the bilayer may experience very different strain from the corresponding free-standing layer, which is not captured in Eq. 1. Second, the equal-area analysis is based on treating the behavior of the plastic as a non-linearly elastic material, i.e. Eqn. 2.5 is a

statement of energy conservation during deformation. In fact, the plastic deforms permanently, and energy is not conserved. Finally, one key observation is that the transition zone between the necked and un-necked region is sharp for the free-standing plastic but becomes much broader as rubber thickness increases. Obviously since the model of the previous section altogether ignores the transition zone, this broadening cannot be captured at all. In fact, the transition region is the only region that actually deforms during stable drawing, and hence is not possible to correctly describe drawing (neither for the free-standing plastic layer nor for the bilayer) without explicitly modeling the transition region(Crist & Metaxas, 2004). We are presently conducting FEM simulations, to be published, which address the deficiencies of the 1D model.

One last noteworthy aspect is sample-to-sample variability in the experiments. The SEPS rubber was found to deform homogeneously in all cases, whereas the LLDPE samples showed highly consistent necking and drawing, with the natural draw ratio λ_{max} being close to 5.7 in all cases. In contrast, the bilayers showed much greater variability as may be judged from Fig. 7 despite no apparent differences in sample quality or sample thickness. A possible reason for this may be judged from Fig. 6b which shows that slightly below the value of $h_r/h_p = 3.25$, the force vs stretch curve must necessarily have a very shallow minimum. In such cases, while necking is possible, imperfections in the experiment may affect whether a neck develops, and how severely. Such imperfections include minor mis-misalignment of the dog-bone shaped specimen with respect to the stretching direction, small stresses imposed during loading the sample, or variations in layer thickness within each sample.

2.5 Summary and Conclusion

We examined the tensile behavior of bilayer laminate films of SEPS rubber and LLDPE plastic with rubber:plastic ratios ranging from 1.2 to 9. Similar to many semi-crystalline polymers, LLDPE when stretched shows necking at a few percent strain owing to plastic yielding, followed by stable drawing owing to its strong strain hardening character, post-yield. In contrast, the elastomer does not exhibit plastic deformation and hence stretches uniformly, similar to most hyperleastic materials. Dog-bone shaped specimens prepared by compression molding were subjected to tensile tests, and the degree of non-homogeneity in the deformation field was quantified by digital correlation image analysis of video recordings of the tensile tests. Bilayer laminates showed behavior that was intermediate between the plastic and the rubber. Bilayers with thin rubber layers showed necking and drawing, but the stretch of the necked region (i.e. the natural draw ratio) was lower than of the free-standing plastic. Moreover, the transition between the necked and un-necked region was also much less sharp than in the LLDPE plastic. At large rubber thickness, necking was almost completely eliminated, although the deformation was not completely homogeneous even at the largest rubber:plastic thickness ratio examined.

A simple model was developed in which the force in the bilayer was taken as the sum of forces in the plastic and the rubber layers measured independently. Mechanical energy balance based on the Maxwell construction, were applied to this model to predict how the rubber layer affects necking and drawing. The model successfully predicted the decrease in the natural draw ratio and the decrease in draw stress with increasing rubber layer thickness. A more detailed model that includes the bond between the two layers, and the transition zone between the necked and un-necked regions may be able to capture the experiments more quantitatively.

3.0 **Necking and Drawing of Rubber–Plastic Laminate Composites: Finite Element Simulations and Analytical Model**

3.1 Introduction

Many polymers show yielding behavior during deformation wherein the slope of the true stress-strain relationship decreases sharply at some stress, generally called the yield stress(Argon, 2013b). However, when deformed to higher strain, some yielding polymers show strong strain hardening wherein the slope of the true stress-strain relationship increases again(Argon, 2013a). A macroscopic consequence of yielding followed by strain hardening is an inhomogeneous deformation behavior called "cold drawing": under tension, a bar of the polymer first develops a neck(Hutchinson & Miles, 1974), however, the deformation in the neck stagnates and then the neck propagates steadily along the length of the bar(Andrews & Ward, 1970; Barenblatt, 1974; Carothers & Hills, 1932; Vincent, 1960). In contrast, elastomers do not show yielding behavior and deform without necking, as may be verified readily by stretching a rubber band.

This article is about the behavior of layered composites of a cold drawing polymer and an elastomer. Composites comprising layers with distinct material properties have been found to exhibit exceptional properties. For instance, the tear strength of a brittle material can be improved by layering it with a compliant layer(Hutchinson, 2014). Bonding a layer of elastomer to a ductile metal can allow the layered composite to stretch a larger extent without necking, whereas the metal alone would neck to failure at only a small applied strain(T. Li et al., 2004; N. S. Lu et al., 2007). For example, a gold film deposited on elastomer was found to stretch 100% more without losing conductivity(Lambricht, Pardoen, & Yunus, 2013).

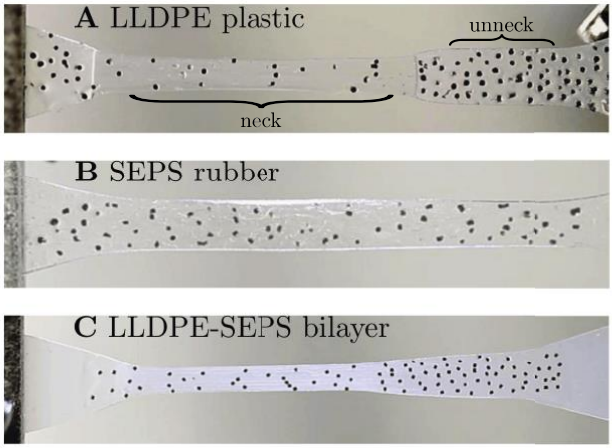

Figure 3: Deformed shapes during tensile tests of dogbone-shaped samples of (A) Cold drawing LLDPE plastic (B) SEPS rubber which deforms uniformly throughout the gauge section. (C) SEPS - LLDPE bilayer of rubber/LLDPE thickness ratio of 1.2(R. G. Ramachandran et al., 2018). Note the strongly non-homogeneous deformation in Figure 3A where the necked region has a stretch of ~6, whereas the unnecked region has a stretch of less than 1.2. In contrast, the stretch in the necked region of the composite in Figure 1C is lower, roughly 4.5. Increasing rubber thickness further reduced the stretch in the necked region(R. G. Ramachandran et al., 2018). The black dots are markers used for quantitative image analysis conducted previously(R. G. Ramachandran et al., 2018).

This paper is motivated by our recent experimental research(R. G. Ramachandran et al., 2018) on the large-deformation tensile behavior of bilayer composites comprising a cold drawing plastic layer (linear low-density polyethylene, LLDPE) bonded to an elastomer (styrene-ethylene/propylene-styrene, SEPS). Figure 3A shows a snapshot of the tensile deformation of a dog bone shaped specimen of LLDPE undergoing cold drawing. The gauge section of the sample shows two distinct zones: a highly stretched necked region with a stretch of almost 6, and an unnecked region with a stretch of less than 1.2. In contrast, SEPS rubber (Figure 3B) stretched without necking to a few hundred percent strain, as typical for elastomers. Figure 3C is a bilayer laminate composite of SEPS and LLDPE whose behavior is intermediate between the plastic and the rubber: while it showed necking and drawing, the degree of non-homogeneity of deformation

reduced as compared to the pure LLDPE. For such composites, deformation became increasingly homogeneous as the rubber/plastic thickness ratio increased, and the transition region between the necked and unnecked regions became much wider.

During drawing the material in the necked region is subjected to a large true stress due to a significant reduction in cross-section area. Strain hardening in the plastic controls the cold drawing phenomenon (Bigg, 1976; Coates & Ward, 1978, 1980; Erickson, 1975; Gsell & Jonas, 1979; Hutchinson & Miles, 1974; Hutchinson & Neale, 1977; Vincent, 1960). The present article focuses on the modifications to the large deformation of thin layers of cold drawing polymers due to the addition of a rubber layer. The goals of this study are as follows. First, we seek a clear understanding of the effects of the rubber modulus and the rubber strain hardening on the deformation. Specifically, the rubber modulus is expected to affect small deformation processes (e.g. neck initiation) whereas the rubber strain hardening behavior is expected to affect large deformation processes (e.g. neck propagation). To isolate these effects clearly, we adopt constitutive equations in which the low strain modulus, yielding behavior, and strain hardening can all be varied independently. Such independent control of various material properties is not possible experimentally. Second, we seek to test whether the predictions of an analytical model developed in our previous paper are valid, even approximately. Even though the model cannot give all details of the deformation during neck propagation, it readily predicts practically useful quantities such as the engineering stress needed for stable neck propagation, or the stretch within the necked region (sometimes called draw ratio). If these model predictions can be shown to agree with 3D simulations, the analytical model can be practically useful for design purposes, e.g. rapidly estimating the rubber/plastic ratio needed to eliminate necking or estimating the maximum stress experienced in each layer.

This paper is organized as follows. Section 3.2 describes the constitutive equations used and the simulation methods. Section 3.3 discusses the simulation results of how rubber thickness affects the stress-strain behavior for one specific case of material properties. Section 3.4 discusses the analytical model to show that many of the important quantities obtained from simulations can be predicted accurately and discusses the effect of inelastic deformation on the model predictions. Further, we conduct a parametric study to test how the material parameters of the rubber affect the initiation of necking and stable neck propagation. Finally, the practical relevance of these results to rubber-plastic laminates are discussed.

3.2 Methods

3.2.1 Constitutive Modeling of Rubber and Cold Drawing Plastic

The rubber (denoted with the subscript r) was modeled as a rate-independent, isotropic, incompressible hyperelastic material. For our constitutive model, the behavior in uniaxial tension is:

$$\sigma_{\mathrm{r}}(\lambda) = [2(C_{1\mathrm{r}} + C_{2\mathrm{r}}\lambda^{-1}) + 4C_{3\mathrm{r}}(\lambda^2 - 2\lambda^{-1} - 3)](\lambda^2 - \lambda^{-1}) \tag{3.1}$$

where σ_{r} is the xx component of the Cauchy stress of the rubber (true stress), λ (true stretch) is the uniaxial stretch along the x direction, and $C_{1\mathrm{r}}, C_{2\mathrm{r}}$, and $C_{3\mathrm{r}}$ are fitting parameters. The constitutive behavior for rubber in terms of the First Piola-Kirchoff (PK1) stress is given as:

$$P_{\mathrm{r}}(\lambda) = \frac{\sigma_{\mathrm{r}}}{\lambda} \tag{3.2}$$

The cold drawing plastic (denoted with the subscript p) was modeled as a rate-independent, isotropic, incompressible elasto-plastic material. For our constitutive model, the behavior in uniaxial tension is:

$$\sigma_{\mathrm{p}}(\lambda) = \begin{cases} 2C_{1\mathrm{p}}(\lambda^2 - \lambda^{-1}) & , \text{if } \sigma_{\mathrm{p}} < \sigma_y \\ \sigma_y + H\bar{\epsilon}_p + 4C_{2\mathrm{p}}(\lambda^2 - 2\lambda^{-1} - 3)(\lambda^2 - \lambda^{-1}) & , \text{if } \sigma_{\mathrm{p}} \geq \sigma_y \end{cases} \tag{3.3}$$

where σ_{p} is the xx component of the Cauchy stress of the plastic (true stress), σ_y is the yield stress, H is the coefficient of linear strain hardening and $C_{2\mathrm{p}}$ is the non-linear strain hardening coefficient. The plastic strain $\bar{\epsilon}_p$is given as

$$\bar{\epsilon}_p(\lambda) = \ln\left(\frac{\lambda}{\lambda_y}\right) \qquad \forall\, \lambda > \lambda_y \tag{3.4}$$

where λ_y is the yield stretch obtained from setting $\sigma_{\mathrm{p}} = \sigma_y$ in Eqn. 3.3. Once again, constitutive behavior of plastic in terms of PK1 stress can be obtained as:

$$P_{\mathrm{p}}(\lambda) = \frac{\sigma_{\mathrm{p}}}{\lambda} \tag{3.5}$$

3D form of the constitutive relations Eqn. 3.1 and Eqn. 3.3 for rubber and plastic were implemented in finite element simulations. Further details of the simulation procedure were published previously(Yang et al., 2017).

3.2.2 Material Parameters for the Rubber and Plastic

The material parameters of cold drawing polymer and hyperelastic rubber were calibrated by regressing simulated engineering stress-applied stretch curves against uniaxial experimental curves for LLDPE and SEPS rubber respectively. For the rubber, the simulated engineering stress with material parameter values $C_{1\mathrm{r}}$ = 0 MPa, $C_{2\mathrm{r}}$= 0.7 MPa, and $C_{3\mathrm{r}}$ = 0.004 MPa yielded a good fit with experimental engineering stress- applied stretch behavior of SEPS (Appendix Figure

A2A). These values are used for most of the research in this paper. For the parametric analysis (Section 3.4.3), C_{1r} was kept constant, whereas C_{2r} was varied from 0.7 to 14.7 MPa, and C_{3r} was varied from 0 to 0.14 MPa. We note that even though C_{1r} = 0 MPa offered a good fit for the experimental behavior of the rubber modelled here, general rubber behavior may require finite value for C_{1r}.

For the cold drawing plastic, the engineering stress response from finite element simulation was calibrated against the experimentally obtained engineering stress response, as well as the experimentally measured draw ratio (i.e., the stretch in the neck during stable drawing), of LLDPE. A minimum of four parameters are needed to fit the four readily quantifiable aspects (three from the stress-strain plot and draw ratio). The simulated engineering response with shear modulus, $2C_{1p}$ = 100 MPa, the yield stress and the strain hardening parameters $\sigma_y = 18.4$ MPa, $H =$ 19 MPa, and $C_{2p} = 0.0073$ MPa captured the experimental engineering stress-applied stretch response reasonably well as shown in the Electronic Supplementary Information (Appendix Figure A2B). These values are used throughout this paper.

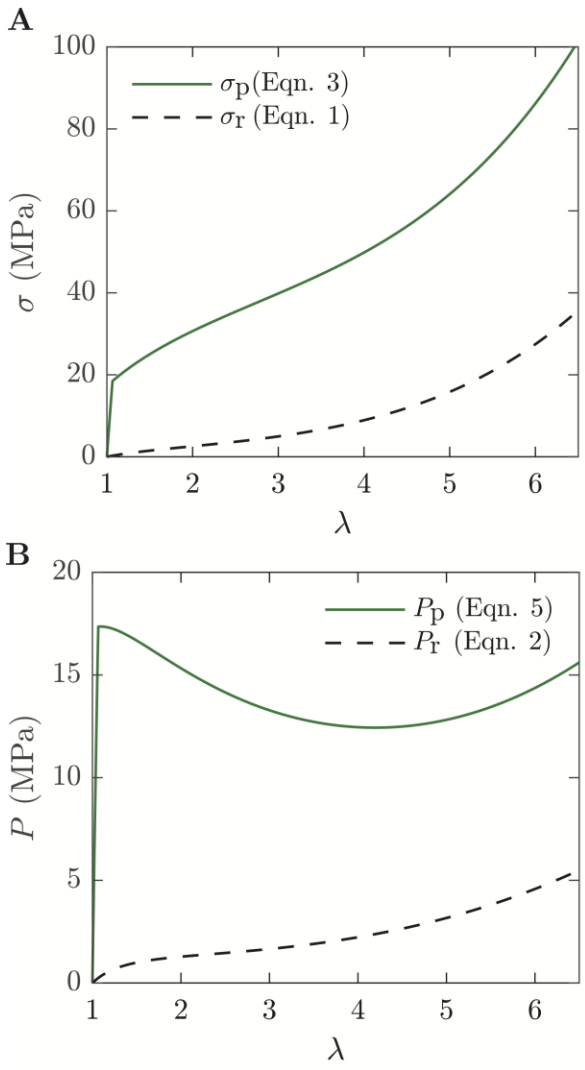

Figure 4: Uniaxial constitutive behavior for the cold drawing plastic and the rubber (A) true stress ($\sigma - \lambda$ curve) (B) PK1 stress ($P - \lambda$ curve). PK1 stress in the plastic does not increase monotonically in contrast to rubber which increases monotonically.

The constitutive behavior in terms of true stress ($\sigma - \lambda$ curve) and PK1 stress ($P - \lambda$ curve) for rubber and plastic with material parameter values given above are shown in Figure 2. The key point to note is that the $P - \lambda$ curve increases monotonically for the rubber layer, but shows a maximum followed by a minimum for the plastic layer. This non-monotonic behavior is the crucial feature that induces necking and drawing as discussed later.

3.2.3 Finite Element Model

Simulations were conducted using a custom nonlinear finite element program. One-eighth of the plastic/rubber/plastic trilayer specimen of rectangular cross-section was modeled to exploit the symmetry of the specimen. The computational model consisted of a single layer of plastic and rubber each, with length l =10 mm along the stretching direction, and width w = 1.5 mm along the transverse direction. This geometry mimics the gauge section of the tensile experiments of Figure 1, although the experiments used bilayers rather than trilayers. The thickness of the plastic layer was kept at, $h_p = 100$ micron and the rubber thickness were varied from h_r= 100 to 800 microns. This corresponds to rubber/plastic thickness ratio (ω) defined as $\omega = h_r/h_p$, in the range from 1 to 8.0. The thickness of the array of elements (75 microns long in the stretching direction) on the top surface along the centerline in the plastic layer was reduced by 2 microns (inset of Figure 5) to consistently introduce necking at the midplane. Roller boundary conditions were enforced on adjoining faces in all three rectangular directions ($X = 0, Y = 0$, and $Z = 0$ planes), as marked by red lines and green circles in the top and side view (Figure 5A and B). The rubber and the plastic faces with $X = l$ (rightmost edge in Figure 3B) were displaced stepwise along x-direction to stretch the sample, whereas the surfaces $Y = w$ and $Z = h_p + h_r$ were specified as stress-free.

The representative computational model of the trilayer was meshed using 8-noded brick elements. Each material layer contained at least 2 elements in the thickness direction with 1330 elements in each layer (mesh shown in Figure 5). The ratio of the deformed length ($\delta + l$) to the original length l is defined as the applied stretch, $\lambda_{app} = 1 + \frac{\delta}{l}$ where δ is the applied displacement. A stretch of 6.5 was applied at the right end in 7000 steps. Stretch, plastic strain and effective stress contours were enumerated at an interval of 20 steps over the specimen volume. The stretch and

stress distribution monitored on the top free surface ($Z = h_r + h_p$) are shown in section 3.3. Reaction forces were measured at all the nodes on the midplane along the length of the specimen ($X = 0$ plane), which is the symmetry plane that acts as a boundary of the simulation domain. The engineering stress (N) over the composite is calculated by: $N = \frac{F}{A_0} = \frac{F}{w(h_r+h_p)}$. where F is the sum of current reaction forces in all the nodes along the midplane ($X = 0$ plane) and $A_0 = w(h_r + h_p)$ is the cross-section area in the undeformed state.

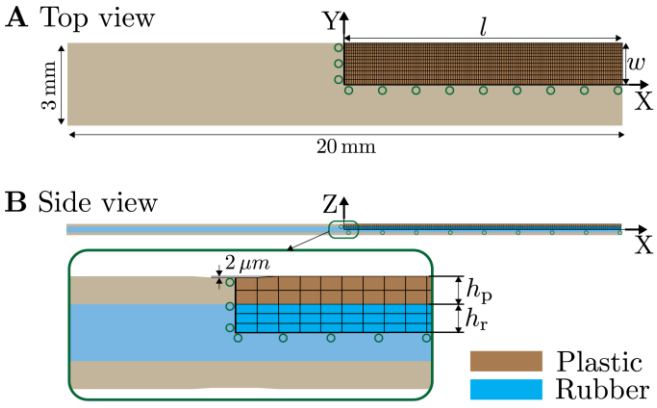

Figure 5: The rectangular specimen geometry 20 x 3mm. One-eighth of geometry is modeled with rollers (green open circles) applied along the X = 0, Y = 0, and Z = 0 planes. The thickness of the element along the center (in the X direction) is decreased by 2 μm to induce consistent neck initiation at the center.

3.3 Results

Section 3.3.1 discusses the deformation of free-standing rubber and cold drawing plastic from finite element simulations. Section 3.3.2 discusses rubber-plastic trilayer composites for different ω values.

3.3.1 Deformation of Free-Standing Plastic and Rubber

The engineering stress in uniaxial tension from finite element simulations for the rubber and the cold drawing plastic is shown in Figure 6A. The corresponding deformed configurations at λ_{app} values of 1, 1.5, 3 and 6 are shown in Figure 6B and C respectively. The color map shows the stretch distribution in the longitudinal direction. The Von Mises stress (σ_e) distribution at λ_{app}=3 for the rubber and cold drawing plastic are shown in Figure 6D and E respectively.

For the rubber, the engineering stress vs applied stretch ($N - \lambda_{\text{app}}$ curve) increases monotonically (Figure 6A), and Figure 6B shows that the deformation remains homogeneous, i.e. at all locations within the sample, the stretch value in the longitudinal direction is equal to the applied stretch. Due to chosen boundary conditions, the stress field is uniform under uniaxial loading, as indicated in Figure 6D. Furthermore, although not shown in Figure 6A, the engineering stress agrees almost exactly with the PK1 stress, $P_{\text{r}}(\lambda)$ (Eqn. 3.2), which was already shown in Figure 4B.

In contrast, for the free-standing plastic, the $N - \lambda_{\text{app}}$ curve does not increase monotonically (Figure 6A). The deformation of the plastic, as shown in Figure 6C is non-homogeneous. The specimen stretches uniformly up to a stretch of 1.12, upon which a neck initiates at the center, and the engineering stress reduces sharply. The neck then stretches locally, whereas the material outside the neck stays at a lower stretch. This state is illustrated at $\lambda_{\text{app}} = 1.5$ in Figure 6C. In concert, the engineering stress reduces towards a plateau at draw stress of $N_{\text{draw}} \approx 13$ MPa. The configuration at $\lambda_{\text{app}} = 3$ in Figure 6C shows the deformed shape typical of a specimen within the engineering stress plateau where three distinct regions can be identified. The first is the necked region near the center which has a large stretch ($\lambda_{\text{neck}} \approx 5.9$) compared to the

rest of the geometry. The second is the unnecked region where the material remains in nearly the same state prior to necking, with a local stretch of $\lambda_{\text{unneck}} \approx 1.1$. The third is the transition region between the aforementioned regions, where the value of the stretch smoothly transitions from the value in necked region to the value in the unnecked region. Similar to the stretch distribution, the stress within this sample is also non-homogeneous as indicated in Figure 6E. The stress is maximum in the neck with a value of 80MPa.

These three regions do not change significantly with λ_{app} throughout the engineering stress plateau; the sole change is the increase in the length of the necked region at the expense of the unnecked region. Thus, this regime of stretching corresponds to stable drawing or stable neck propagation. Finally, at $\lambda_{\text{app}} = 5.9$ the necked state spans the entire specimen, beyond which the sample stretches homogeneously.

Incidentally, the dip in stress seen at $\lambda_{\text{app}} \approx 5.5$ is due to the geometric softening when the neck reaches the edge of the specimen. The reduction in cross-section of the transition zone reduces the force required to sustain tensile deformation. Such a dip is an artifact of the rectangular simulation geometry and would not be seen experimentally when dog-bone shaped specimens are used.

Unlike the rubber which deforms homogeneously, for the cold drawing plastic, the $N - \lambda_{\text{app}}$ curve distinctly deviates from the $P - \lambda$ relation. Analytical prediction of some of the features of $N - \lambda_{\text{app}}$ curve from the $P - \lambda$ relation is discussed in Section 3.4.

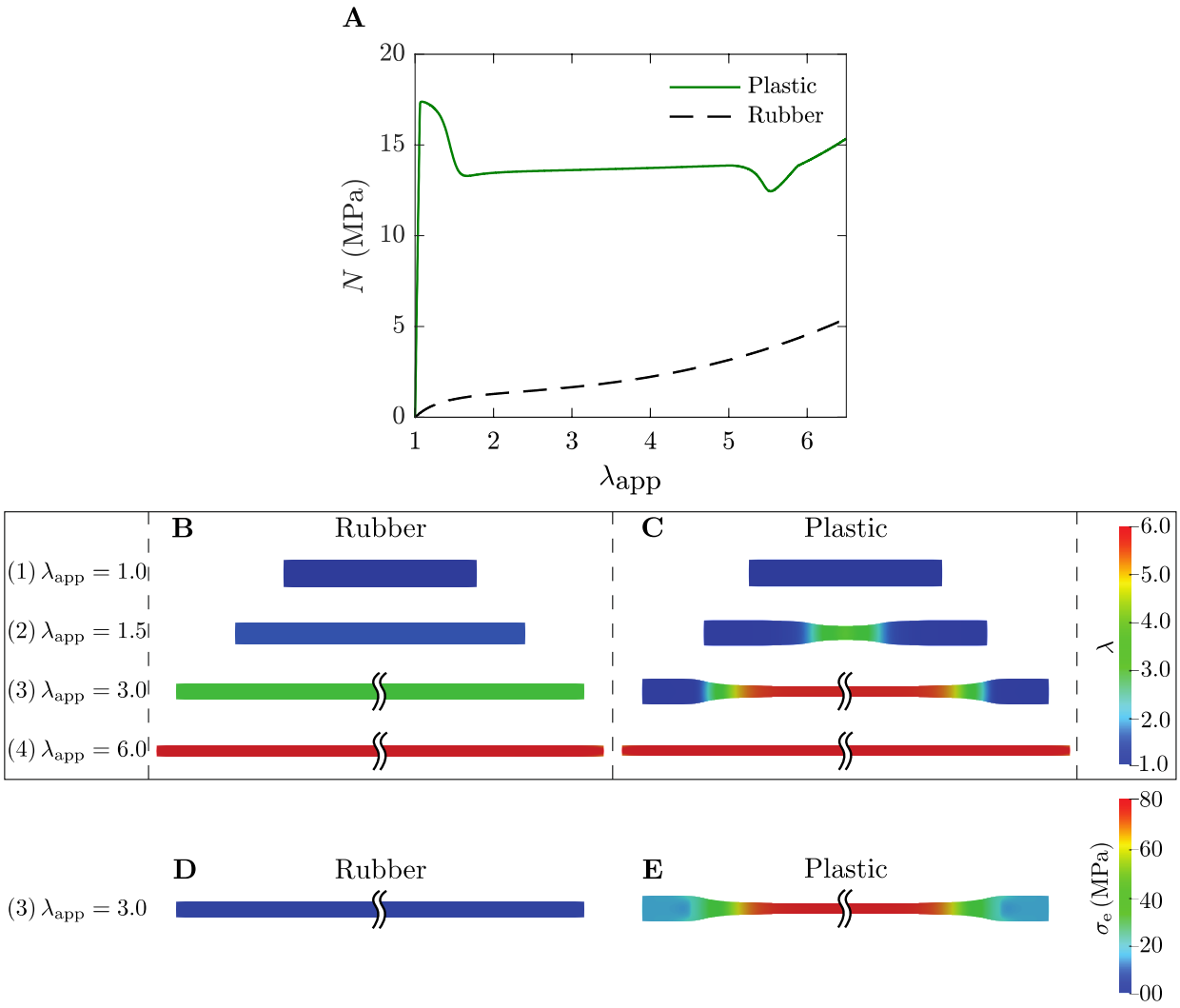

Figure 6: (A). Engineering stress vs applied stretch ($N - \lambda_{app}$ curve) from simulations of rubber and cold drawing plastic. Initial configuration and deformed configurations for (B) the rubber and (C) the cold drawing plastic. Numbers far left indicate applied stretch (λ_{app}) values for each configuration, and contours indicate the distribution of stretch in the tensile direction. Deformed configuration with color map of Von Mises stress, σ_e at an applied stretch (λ_{app}) of 3 for the rubber (D) and the cold drawing plastic (E).

3.3.2 Deformation of Rubber-Plastic Laminates

The engineering stress response ($N - \lambda_{app}$ curve) of laminate composites with ω =1, 3 and 7 are shown in Figure 7A. The curves for the free-standing plastic layer ($\omega = 0$) and the free-standing rubber, which were shown in Figure 6A, are also shown for reference. The deformed shapes at a λ_{app} =3 for the specimens are shown in Figure 7B. The color maps indicate the local stretch in the x-direction. For $\omega = 1$ and 3, the engineering stress exhibits a peak, followed by a plateau, both typical of necking and stable drawing behavior. The corresponding deformed shapes clearly show non-homogeneous deformation. The stretch maps indicate that with increasing ω, the stretch in the neck λ_{neck} decreases and the stretch in the unnecked region λ_{unneck} increases. The λ_{neck} and λ_{unneck} remain constant throughout the neck propagation, similar to the free-standing plastic in Figure 6B. However, λ_{neck} and λ_{unneck} approach each other with increasing ω. All these trends agree with our previous experimental observations(R. G. Ramachandran et al., 2018). For $\omega = 7$, necking is eliminated completely as judged by both, the monotonic rise on N with λ_{app} as well as by the uniform stretch distribution.

It is interesting to compare the simulated behavior of the composite against a thickness-weighted sum of the force in each free-standing layer. However, such force additivity of the free-standing rubber and plastic does not capture the entire stress-stretch behavior of the laminate composite accurately. This issue is discussed further in the Supplementary Information along with Figure A1.

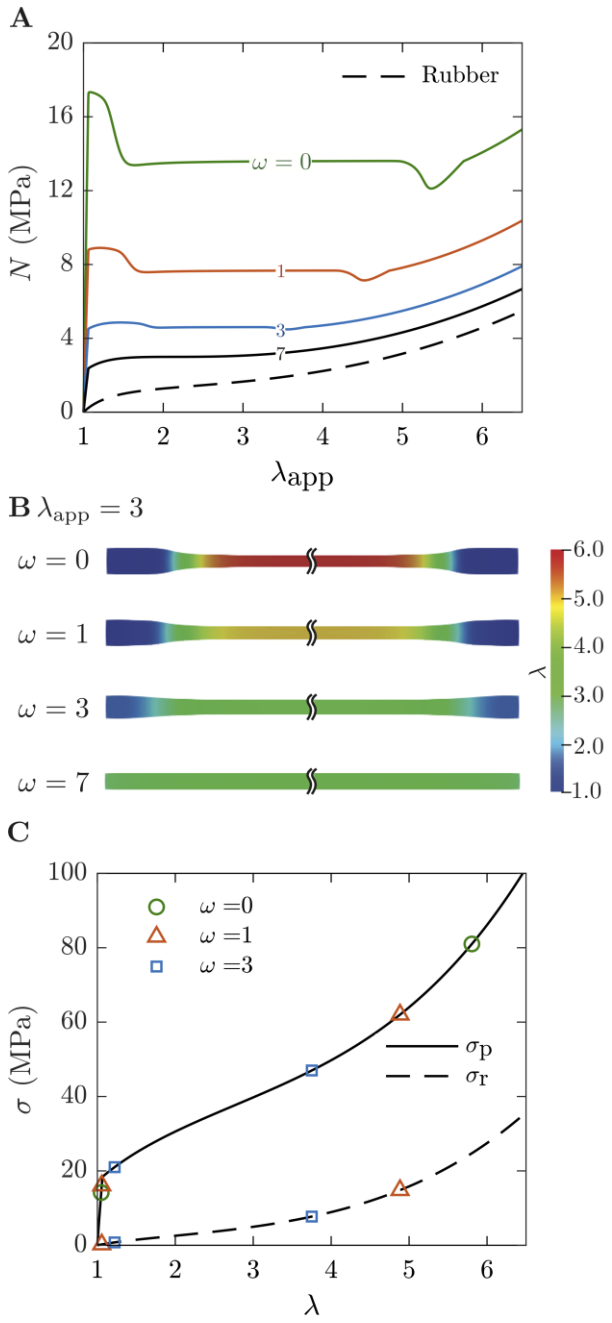

Figure 7: (A) Engineering stress vs applied stretch ($N - \lambda_{app}$) response of layered composites with rubber/plastic ratios (ω) listed alongside each curve. (B) The deformed configurations at λ_{app}=3 for free-standing plastic ($\omega = 0$) and composites of ω values listed on the left of each image. (C) The true stress in the necked and unnecked regions of individual layers of HDPE (ω = 0) and composites (ω = 1 and 3) are marked on the respective true stress vs true stretch ($\sigma - \lambda$) curve. Solid and dashed lines are the $\sigma - \lambda$ for the rubber and plastic, Eqns. 3.1 and 3.3 respectively.

To further emphasize this issue of different strain states, Figure 7C plots the Cauchy stress and the stretch of the individual layers within the composites in the necked and unnecked region. The solid and dashed curves represent the constitutive behavior of the plastic and the rubber in uniaxial tension respectively (Eqns. 3.3 and 3.1). The circles on the solid curve mark the true stress in the necked and unnecked region for free-standing plastic, with the larger value of stress corresponding to the necked region. With increase in ω, the true stress in the necked region decreases. This plot shows that the plastic layers in the composites experience lower stress and therefore experience deformation states that are inacessble to the free-standing plastic during drawing.

Another significant effect is that the increase in ω delays the peak in engineering stress-stretch response (λ_{peak}) to a larger applied stretch. Yet the yield strain in the plastic layer of the composite remains a constant since it is a material property. Therefore increasing ω increases the inelastic deformation in the plastic material at the onset of necking. This is illustrated more clearly in Figure 8, which plots the plastic strain at the onset of necking; it is clear that when bonded to rubber, the plastic layer can undergo large plastic deformation before necking. This same point was made previously by Li and Suo(T. Li et al., 2005), albeit with a plastic that was not capable of cold drawing. The central point, therefore, is that bonding together the rubber and the plastic force the individual materials to stretch in a fashion that is different from the same materials when stretched alone.

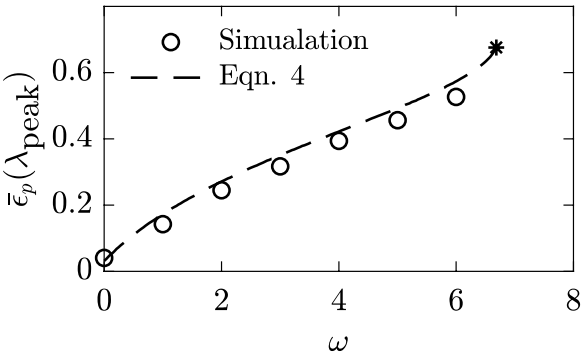

Figure 8: Effective plastic strain from the 3D simulations at the onset of necking is shown as open circles. The dashed line corresponds to substituting the prediction for $\lambda = \lambda_{\text{peak}}$ from Eqn. 3.7 into Eqn. 3.4.

Four key quantities of practical interest, λ_{peak}, N_{draw}, λ_{neck}, and λ_{unneck} can be extracted readily from the simulations. The first two can be extracted directly from the engineering stress data: the stretch corresponding to the peak in engineering stress, λ_{peak}, which marks the onset of necking, and the engineering stress, N_{draw} for stable drawing, corresponding to the stress plateau. The increase in λ_{peak} with ω is shown in Figure 9A, whereas the decrease in N_{draw} with ω is shown in Figure 9B. λ_{neck} and λ_{unneck} can be obtained from the deformed configurations. To do this in a consistent fashion for all samples, we plot the highest and the lowest stretch within each specimen during stretching (see Appendix Figure A3) and extract the two plateau values which correspond to stable drawing. The two quantities are plotted vs the rubber/plastic ratio ω in Figure 9C. Such plots depend on the material properties, and Section 3.4.2 will show similar plots for laminate composites with different parameter values in the material constitutive equations. The solid curves in Figure 9 will be discussed later.

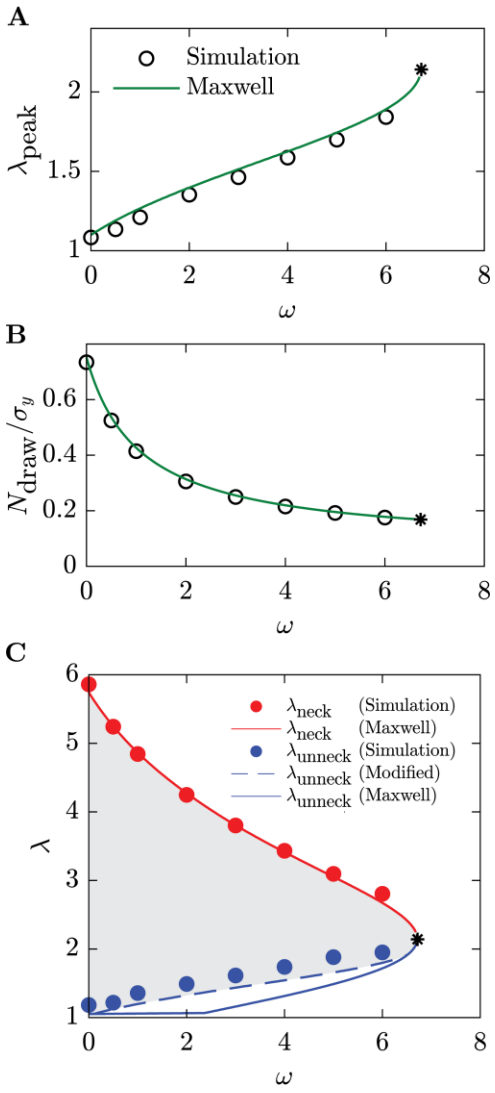

Figure 9: (A) Open circles are stretch values at which simulations show a peak in engineering stress. (B) Open circles are normalized engineering draw stress from simulations. (C) Filled circles are simulation results for the stretch in the necked and unnecked regions (λ_{neck} and λ_{unneck}) during stable drawing. Solid lines are predictions: in (A) solid curve is the λ at which $P - \lambda$ curve of composites (Eqn. 3.7) shows a peak, at any value of ω. In (B) and (C) solid curves are the predictions of N_{draw} (normalized by σ_y), λ_{neck} and λ_{unneck} by applying Maxwell construction to Eqn. 3.7 (see Figure 11). The dashed line in (C) is the prediction for λ_{unneck} after correcting for inelastic deformation effects (see text and Figure 12). In all graphs, the asterisk is the critical point, i.e. the lowest ω value (ω_c) needed for the $P(\lambda)$ from Eqn. 3.7 to be monotonically increasing.

3.4 Analytical Model

The central phenomenon of interest in this paper is the coexistence of two strain states during stable drawing and the changes in these states as rubber thickness changes. We extend the Maxwell analysis, which identifies the two coexisting states(Coleman, 1983; Erickson, 1975; Fager & Bassani, 1986; Hutchinson & Neale, 1983; Neale & Tugcu, 1985), to the tensile deformation of the composites. Unlike our previous paper(R. G. Ramachandran et al., 2018), we will focus on the energy of the system to make more explicit the analog to phase transition phenomenon familiar from thermodynamics and to make more transparent the issue of inelastic deformation that was ignored previously.

3.4.1 Comparison Against Energy-Based 1D Model

It is well-recognized that in uniaxial elongation of a bar, if the $P-\lambda$ curve shows a maximum, a neck initiates at the stretch corresponding to the maximum(Considère, 1885; Courtney, 1990a). Stable neck propagation further requires that the homogenous $P-\lambda$ curve also has a minimum(Coleman, 1983; Erickson, 1975; Neale & Tugcu, 1985). Figure 10A therefore illustrates a $P-\lambda$ curve showing such a maximum followed by a minimum. In previous analyses of stable neck propagation(Coleman, 1983; Erickson, 1975; Hutchinson & Neale, 1983), the cold drawing material was assumed to have a fictitious non-linear elastic sigmoidal stress-stretch response, and a Maxwell equal area construction was then developed to identify the two coexisting strain states that correspond to stable drawing. This construction is illustrated as a dashed green line in Figure 10A, where points *b* and *c* correspond to the unnecked and necked states respectively,

and the shaded areas are equal. Prediction from Maxwell analysis has been compared against experiments previously and found to have a reasonable agreement(Crist & Metaxas, 2004).

The total area under the $P - \lambda$ curve is proportional to the work done in deforming the sample to any desired applied stretch, λ_{app}. Within the energy-conservation framework, this corresponds to the strain energy density, W

$$\mathrm{W} = \int_{1}^{\lambda_{\text{app}}} P \, d\lambda \tag{3.6}$$

It is illuminating to illustrate the deformation process on a W vs λ_{app} diagram (Figure 10B), which closely resembles the energy vs order parameter diagrams commonly used in the study of phase transitions. Coexistence between the necked and unnecked states can now be identified by the familiar double-tangent construction for first-order phase transitions. This double-tangent makes it obvious that for λ_{app} values between those of points *b* and *c*, a specimen with two coexisting strain states can have lower energy than a specimen that stays homogeneous. The region between points *b* and *a* is metastable: while a specimen may remain in a homogeneous strain state, the separation between two coexisting strain states can reduce the energy to the value indicated by the double tangent. Such metastable states, e.g. supercooled liquids, are well-known amongst phase transitions. Thus, when stretching a bar of the material, necking initiates when the specimen is stretched to point *a*; once the neck is initiated, the stress must reduce to the level indicated by the Maxwell construction while the sample bifurcates into unnecked and necked regions in states *b* and *c* respectively. This decrease in stress is accompanied by a decrease in energy, indicated by a downward arrow in Figure 10B.

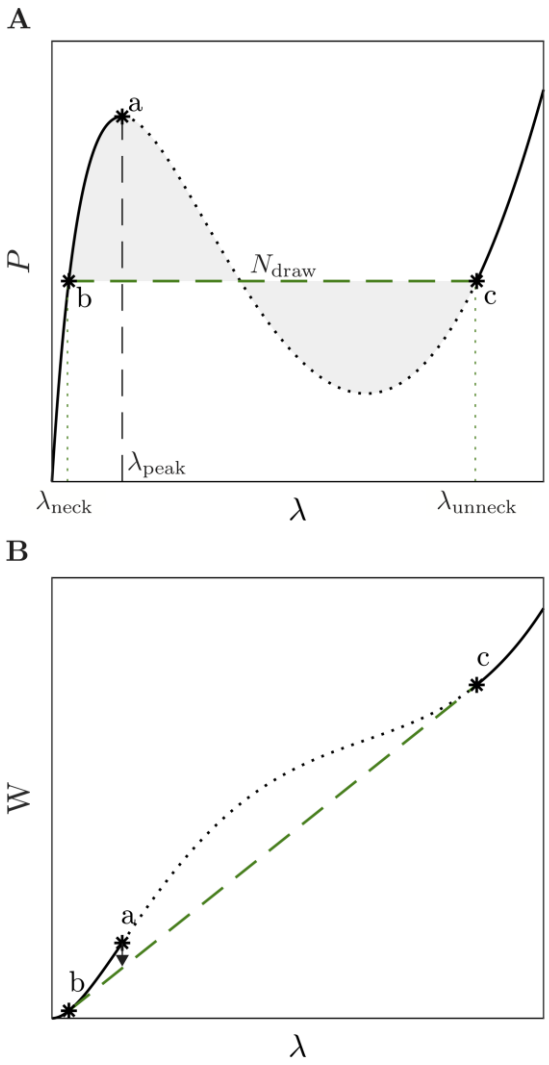

Figure 10: (A) Schematic of a $P - \lambda$ curve with a maximum and minimum, which can show stable neck propagation. The neck initiates at the peak load (marker *a*). Constant PK1 stress dashed green line (N_{draw}) corresponds to the Maxwell construction where the two shaded areas are equal. Points *b* and *c* correspond to material states in the unnecked and necked region during stable neck propagation. (B) Strain energy per unit volume corresponding to constitutive behavior shown in Figure 10A. The dashed green line is a double tangent to the $W(\lambda)$ curve. The black dotted curves in both figures correspond to unstable regions where homogeneous deformation is not possible.

The schematic of Figure 10 applies for any specimen capable of stable drawing in tension. To apply it quantitatively to layered composites, an expression is needed for the $P-\lambda$ curve. We adopt a simple expression of thickness-weighted stress additivity:

$$P = P_{\mathrm{p}}\left(\frac{1}{\omega+1}\right) + P_{\mathrm{r}}\left(\frac{\omega}{\omega+1}\right) \tag{3.7}$$

It must be emphasized that Eqn. 3.7 adds the nominal stresses under homogenous deformation. Eqn. A1 in the Appendix discusses a different version which adds forces from the free-standing layer.

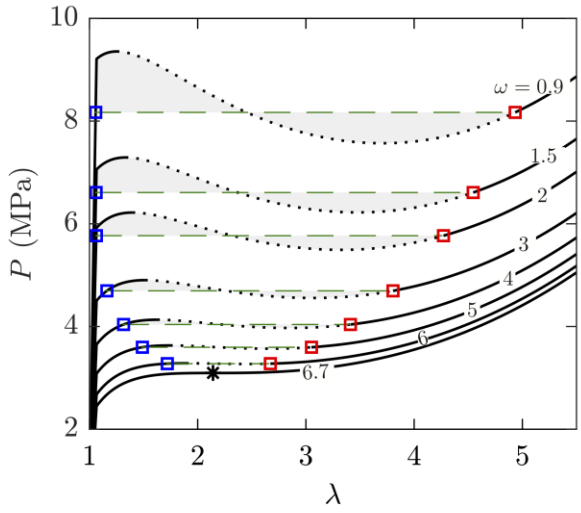

Figure 11: $P-\lambda$ curves for composites (Eqn. 3.7) of various ω values indicated for each curve. Dotted regions of each curve correspond to regions where homogeneous stretching is not possible. Dashed green lines show Maxwell constructions where the shaded areas above and below each green line are equal. The material configurations in the necked and the unnecked regions are marked as the red and blue squares respectively on each $P-\lambda$ curve. The $P-\lambda$ curve is monotonic for laminate composites with $\omega > 6.7$ (not shown here).

Using the analytical expressions from Eqns. 3.2 and 3.5, the $P-\lambda$ curve for the laminate composite can be calculated from Eqn. 3.7. Plots of Eqn. 3.7 for various values of ω are shown in Figure 11. For small values of ω, this equation is non-monotonic. The maximum then gives the

stretch, λ_{peak}, at which a neck initiates. Further, the Maxwell construction identifies λ_{neck}, λ_{unneck}, (the red and blue squares respectively) and the draw stress, N_{draw} (PK1 stress corresponding to horizontal green dashed line). This Maxwell construction implemented using MATLAB®, is also illustrated in Figure 11. For $\omega \geq 6.7$, P increases monotonically with λ, i.e. it is no longer possible to initiate necking. The corresponding predictions for stable neck propagation are shown as solid lines in Figure 9: these correspond to the location of the maximum of Eqn. 3.7 in Figure 9A, and the results of the Maxwell construction in Figure 9B and C.

There is an obvious resemblance of Figure 9C to second-order phase transitions, e.g. gas-liquid coexistence near the critical point, liquid-liquid coexistence near the consolute point or the ferromagnetic transition near the Curie point. For the specific material parameters selected here, the critical value of rubber thickness, i.e. the value above which $P(\lambda)$ becomes monotonic, corresponds to $\omega_c = 6.7$. Indeed, Appendix Figure A4 plots the results in the form suggested from the critical phenomena literature and shows that $(\lambda_{neck} - \lambda_{unneck}) \propto (\omega_c - \omega)^{\beta}$. The critical exponent β is found to be 0.54, a value close to 0.5, predicted from the mean-field theory of critical phenomena.

As mentioned in the Introduction, one key goal of this paper was to examine whether the analytical model of Eqn. 3.7, combined with the Maxwell construction, can predict the key quantities obtained from the simulations. If so, the model can give rapid predictions for composite behavior based on pure component properties without needing detailed simulations. The solid curves in Figure 9 suggest that the model can predict all quantities well, except λ_{unneck} which is significantly underpredicted. Section 3.4.3 will show that the degree of the underprediction of λ_{unneck} depends on the material properties. The following section examines the reasons for the underprediction.

3.4.2 Irreversible Deformation Effects

The effect of irreversible deformation of the cold drawing plastic layer on the prediction of material configuration in the unneck region of the composite is discussed below. For illustrative purposes, most of the calculations in this section are done for a rubber-plastic composite of $\omega = 3.5$. The $P - \lambda$ curve calculated from Eqn. 3.7, with $\omega = 3.5$, is shown in Figure 12A. As explained along with the discussion of Figure 10 above, during initial stretching, the neck initiates at the maximum in the $P - \lambda$ curve, marked *a* . As per the Maxwell construction, stable neck propagation requires lower engineering stress. This decrease in engineering stress after point *a* must be accompanied by a decrease in the stretch in the unnecked region. In a purely elastic system, the stretch of the unnecked region can recover from point *a* to point *b*, and in this final state, both layers would still remain under tension. However, with plasticity effects, i.e. irreversible deformation, the situation is different: if $\lambda_a - \lambda_b > \epsilon_y$, the plastic layer would lose tension altogether and experience compression. Further if $\lambda_a - \lambda_b > 2\epsilon_y$, the plastic would have to yield in compression. Here $\epsilon_y = \lambda_y - 1$ is the yield strain of the cold drawing material. The rubber in the unnecked region may not have sufficient elastic energy to accomplish the work necessary to force this compressive deformation. Therefore, the actual stretch of the unnecked region, λ_d would exceed λ_b. The goal of this section is to estimate λ_d through an energy analysis that accounts for irreversible work done.

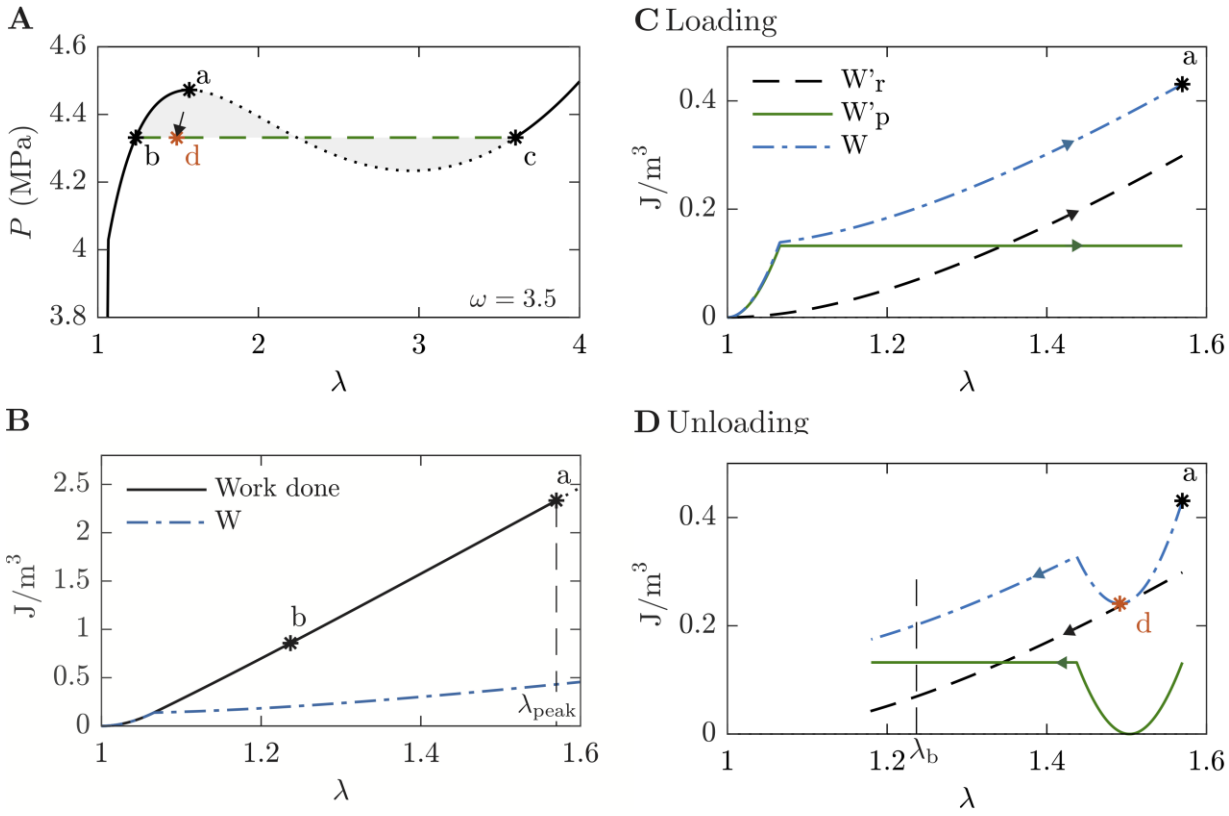

Figure 12: (A) $P-\lambda$ curve for the rubber-plastic laminate of $\omega = 3.5$ (Eqn. 3.7). Maxwell construction is indicated by the green dashed, constant PK1 stress line. The points *b* and *c* where the Maxwell construction intersects the $P-\lambda$ curve are the predictions for material states in necked and unnecked regions. The material state in the unnecked region after considering the inelastic deformation of is marked as *d*. The dashed arrow linking *a* and *d* is indicative only. (B) Loading from $\lambda = 1$ to $\lambda = \lambda_a$. The black curve is the work done per unit volume of the composite, i.e. the area under the $P-\lambda$ curve in A. Blue dot-dashed line is the total strain energy density (Eqn. 3.8). (C) Strain energy density when loading from $\lambda = 1$ to $\lambda = \lambda_a$. Plastic contribution (green) and rubber contribution (black dashed), their sum (blue dot-dashed, which is the same curve as in B). (D) Strain energy density when unloading from $\lambda = \lambda_a$.

For the following analysis, the composite is treated as a single material with uniform properties. The strain energy density of the composite is computed by the volume fraction-

weighted sum of rubber and plastic strain energy density during loading and unloading. Loading and unloading are considered separately due to path dependence of the cold drawing material.

Therefore, we now write the total strain energy in the layered composite as a sum of contributions from the rubber and the plastic:

$$wl\left(h_{\mathrm{r}}+h_{\mathrm{p}}\right)\mathrm{W}(\lambda)=wlh_{\mathrm{r}}\mathrm{W}_{\mathrm{r}}(\lambda)+wlh_{\mathrm{p}}\mathrm{W}_{\mathrm{p}}(\lambda)$$

Hence

$$\mathrm{W}(\lambda)=\frac{\omega}{\omega+1}\mathrm{W}_{\mathrm{r}}(\lambda)+\frac{1}{\omega+1}\mathrm{W}_{\mathrm{p}}(\lambda)$$

$$\mathrm{W}(\lambda)=\mathrm{W}_{\mathrm{r}}^{'}(\lambda)+\mathrm{W}_{\mathrm{p}}^{'}(\lambda) \tag{3.8}$$

where w and l are the width and length of the specimen, respectively. $\mathrm{W}_{\mathrm{r}}^{'}(\lambda)=\frac{\omega}{\omega+1}\mathrm{W}_{\mathrm{r}}(\lambda)$ is the rubber contribution to the strain energy density of the laminate composite, and similarly, $\mathrm{W}_{\mathrm{p}}^{'}(\lambda)=\frac{1}{\omega+1}\mathrm{W}_{\mathrm{p}}(\lambda)$ is the plastic contribution to the strain energy density of the laminate composite.

During the loading process, for the rubber layer, all the work is presumed to be reversible, and hence is stored as elastic energy:

$$\mathrm{W}_{\mathrm{r}}(\lambda)=\int_{1}^{\lambda}P_{\mathrm{r}}(\lambda)\,d\lambda \tag{3.9}$$

In contrast, for the plastic, only the work done prior to yielding is taken to be reversible. Thus, the plastic strain energy density is given as:

$$\mathrm{W}_{\mathrm{p}}(\lambda)=\begin{cases}\displaystyle\int_{1}^{\lambda}P_{\mathrm{p}}(\lambda)\,d\lambda & ,\text{if } \lambda<\lambda_{y}\\ \displaystyle\int_{1}^{\lambda_{y}} & \\ \displaystyle\int_{1}^{}P_{\mathrm{p}}\,(\lambda)d\lambda & ,\text{if } \lambda\geq\lambda_{y}\end{cases} \tag{3.10}$$

From the above equations, W_r', W_p', and their sum $W(\lambda)$, during the loading process can be calculated readily and the values for $\omega = 3.5$ are shown in Figure 12C. It is important to note that the latter integral in Eqn. 3.10 is independent of λ, i.e. beyond the yield point, the plastic makes no further contribution to elastic energy. Therefore W_p' becomes flat for stretch larger than λ_y in Figure 12C. The strain energy density of the composite, $W(\lambda)$ and the work done per unit volume up to the $P - \lambda$ curve peak (marker *a*) are shown in Figure 12B. At the onset of necking, the work done per unit volume of the composite far exceeds the strain energy density.

We now turn to the unloading process in which the λ reduces starting from point *a*. To proceed, it is convenient to define $\Delta\epsilon = \lambda - \lambda_a$, i.e. the decrease in strain after the neck initiates, and $\epsilon_y = \lambda_y - 1$ as the yield strain. Since the rubber is elastic, its loading and unloading is not path dependent. Hence the rubber contribution to the strain energy density of the laminate during unloading is $W_r'(\lambda_a - \Delta\epsilon)$ from Eqn. 3.9. The plastic contribution to the strain energy density of the laminate during unloading is path dependent and given as:

$$W_p(\lambda) = \begin{cases} W_p(\lambda_a) - \int_{1+\epsilon_y}^{1+\epsilon_y-\Delta\epsilon} P_p(\lambda)\, d\lambda & , \text{if } \Delta\epsilon < (\epsilon_y) \\ \int_{1}^{1+(\Delta\epsilon-\epsilon_y)} P_p(\lambda)\, d\lambda & , \text{if } (\epsilon_y) \le \Delta\epsilon < 2(\epsilon_y) \\ \int_{1}^{1+\epsilon_y} P_p(\lambda)\, d\lambda & , \text{if } \Delta\epsilon \ge 2(\epsilon_y) \end{cases} \tag{3.11}$$

Eqn. 3.11 can be understood as follows: As the stretch decreases below λ_a, the plastic layer first reduces its strain energy density while remaining under tension. At $\Delta\epsilon = \epsilon_y$, the plastic completely loses tension and its strain energy density is zero. Further increase in $\Delta\epsilon$ forces the

plastic into compressive deformation, and the strain energy density increases. Once $\Delta\epsilon$ reaches $2\epsilon_y$, the plastic yields in compression, after which there is no further increase in strain energy density. This process is represented by the U-shaped green curve in Figure 12D. The total strain energy in the composite during unloading can be found by adding the plastic and the rubber contributions (Eqn. 3.8), and is shown as the U-shaped blue dot-dashed curve. The minimum in this blue dot-dashed curve is now the predicted value of the stretch λ_{d} of the unnecked state. The point *d* is also marked in Figure 12A. The dashed arrow linking *a* and *d* is only for illustration, and not quantitative.

The calculation illustrated in Figure 12 was done for several ω values to obtain a prediction for $\lambda_{\mathrm{unneck}}$ which is shown as the dashed blue line in Figure 9C. It is in reasonable agreement with the $\lambda_{\mathrm{unneck}}$ obtained from simulations suggesting that the above model can successfully capture the effects of inelastic deformation. We emphasize that this updated prediction still relies on Eqn. 3.7, but it no longer uses the Maxwell construction.

3.4.3 Effect of Rubber Parameters

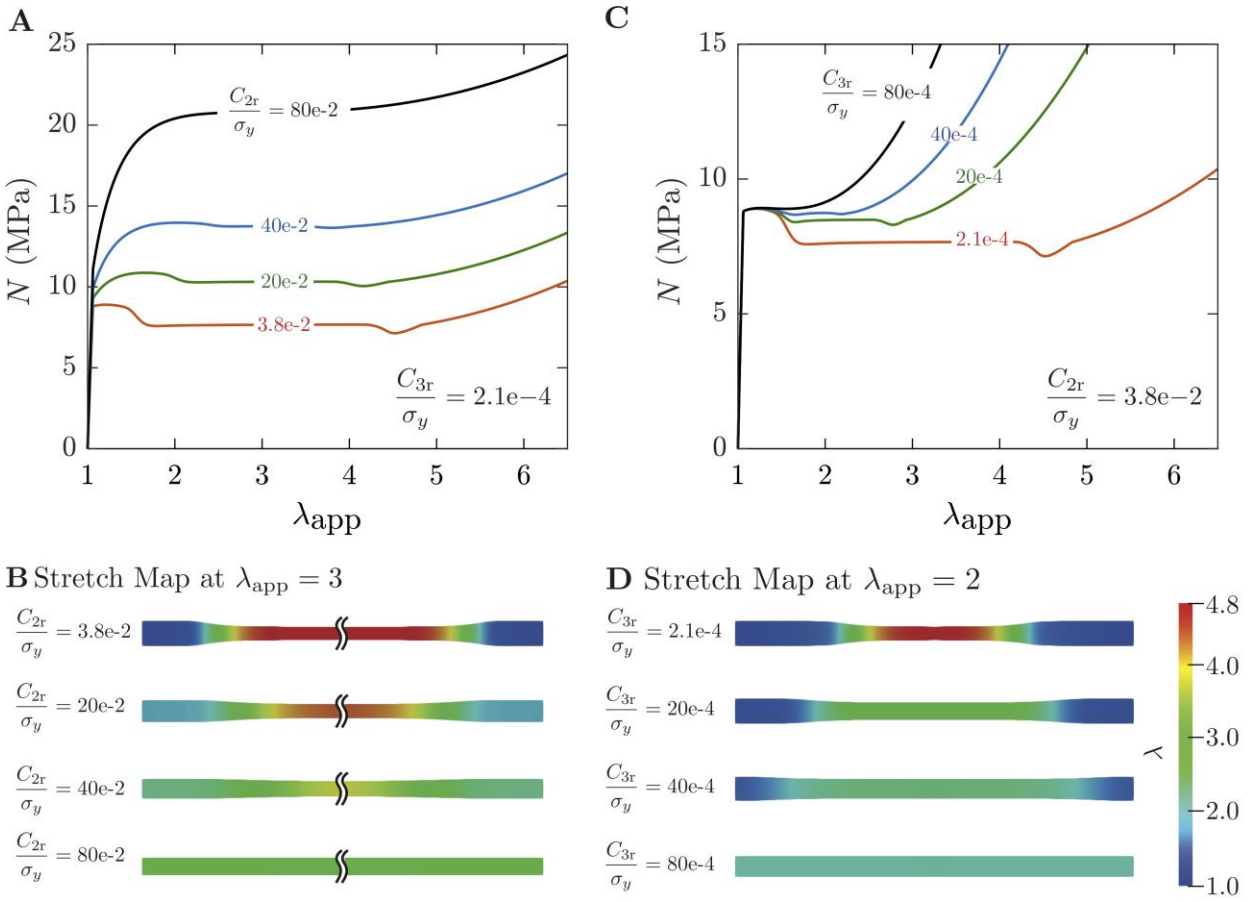

Figure 13: (A&B): Engineering stresses and deformed shapes for laminate composites at $\lambda_{app} = 3$ with $\omega = 1$ as the C_{2r} value is changed keeping $C_{3r} = 0.004\ MPa = 0.00021 \times \sigma_y$. (C&D): C_{3r} value is changed while keeping $C_{2r} = 0.7\ MPa = 0.038 \times \sigma_y$. The deformed configuration is shown at a $\lambda_{app} = 2$. The orange solid curves are identical to the orange curve in Figure 7.

Simulations were conducted varying the two parameters C_{2r} and C_{3r} which define the constitutive behavior of the rubber (C_{1r} was still kept at zero). These simulations were done only at an equal thickness of the rubber and plastic layers, i.e. at $\omega = 1$. Figure 13 shows the engineering stress curves and the corresponding deformed shapes as C_{2r} or C_{3r} are increased, holding all the

other parameters constant. Qualitatively, the effect of changing these parameters is similar to that of changing rubber thickness (Figure 7): increasing these parameters reduces the non-homogeneity of deformation (necking appears at a higher applied stretch; λ_{neck} decreases; λ_{unneck} increases) and the nominal draw stress increases. At sufficiently high values of $C_{2\text{r}}$ and $C_{3\text{r}}$, necking is eliminated altogether.

There are however quantitative differences between the effects of these two parameters, which can be seen by plotting the four key metrics, $\lambda_{\text{peak}}, \lambda_{\text{neck}}, \lambda_{\text{unneck}}$ and N_{draw}, against $C_{2\text{r}}$ and $C_{3\text{r}}$ (Figure 14). It is clear that the stretch at which the neck appears, λ_{unneck} and N_{draw} all increase significantly as $C_{2\text{r}}$ increases, whereas these same quantities are fairly insensitive to $C_{3\text{r}}$. In contrast, the stretch of the necked region, λ_{neck}, is strongly sensitive to $C_{3\text{r}}$. The reasons for these trends are evident from Eqn. 3.1, the constitutive behavior for the rubber in uniaxial tension. With a series expansion at small strains, it can be shown that

$$\sigma_{\text{r}} = (6C_{2\text{r}} - 48C_{3\text{r}})(\lambda - 1) + \mathcal{O}((\lambda - 1)^2) \tag{3.12}$$

i.e. the tensile modulus is $(6C_{2\text{r}} - 48C_{3\text{r}})$. Since the $C_{2\text{r}}$ values in Figure 14 are typically two orders of magnitude higher than $C_{3\text{r}}$ values, the tensile modulus, and hence the small-strain behavior, is almost entirely dominated by $C_{2\text{r}}$. Since the neck usually initiates at small stretch values, and λ_{unneck} is also usually small, both these are fairly insensitive to $C_{3\text{r}}$. On the other hand, at large stretch, the terms containing $1/\lambda$ in Eqn. 3.1 become less important and hence the large strain behavior is dominated by $C_{3\text{r}}$. More specifically, as the rubber becomes more strain hardening with increasing $C_{3\text{r}}$, it strongly resists large deformation, and hence the λ_{neck} value reduces sharply.

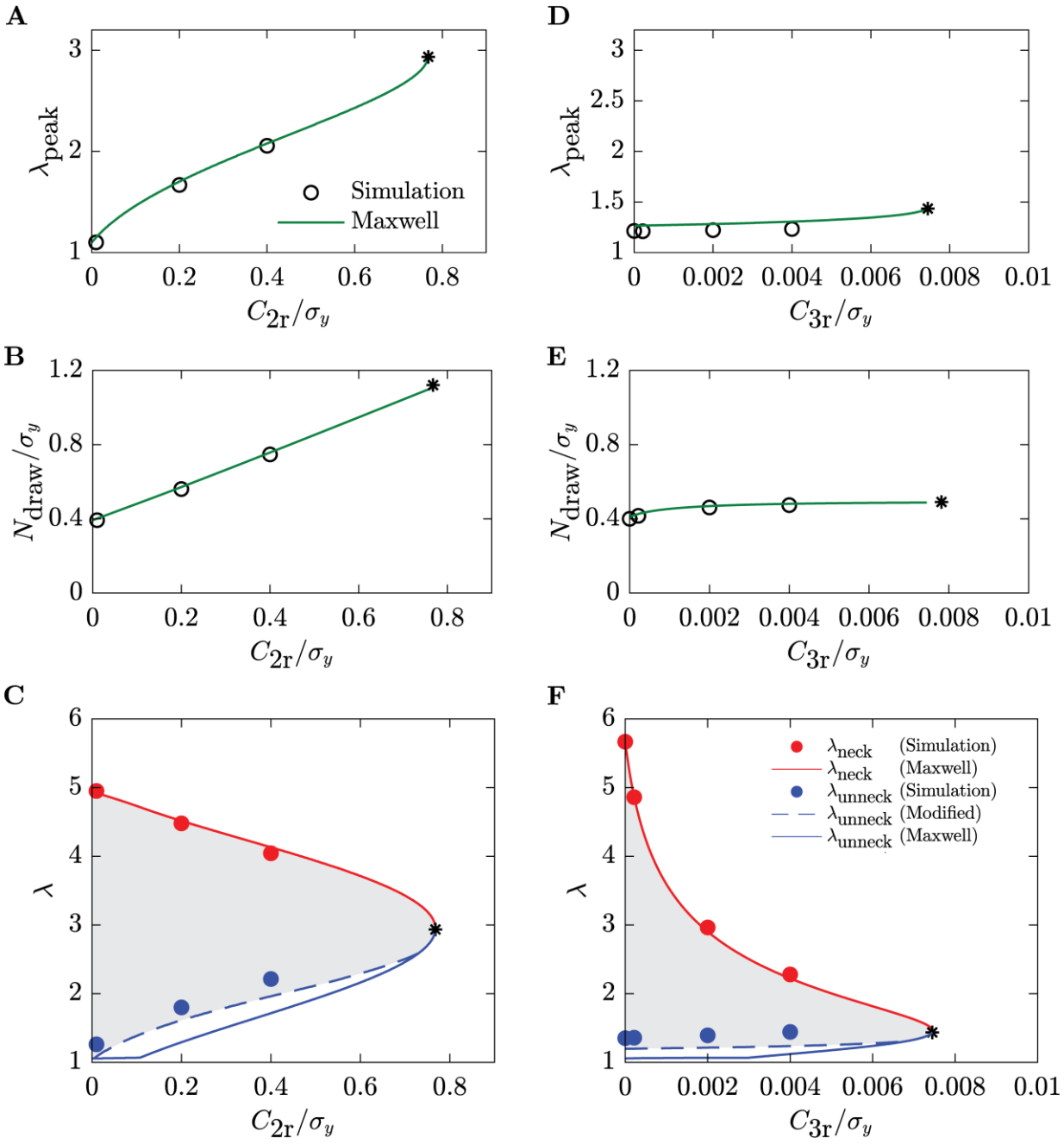

Figure 14: Parameters extracted from the simulations of the previous Figure 13. Solid lines in A and D are the location of the maximum PK1 stress in Eqn. 3.7. Solid lines in B, C, E, F are predictions of Maxwell construction as applied to Eqn. 3.7. The dashed line in C and F are the modification described in section 3.4.2.

Finally, we also calculated these four quantities using the models of Section 3.4.1 and 3.4.2 and those predictions are shown as solid lines in Figure 14. Broadly, the conclusions remain the same as in the previous two sections: Eqn. 3.7 along with the Maxwell construction method gives excellent predictions for λ_{peak}, λ_{neck}, and N_{draw}. However, $\lambda_{\mathrm{unneck}}$ is significantly underpredicted by the Maxwell construction and slightly underpredicted by the correction for irreversible deformation illustrated in Figure 12.

3.4.4 Practical Relevance

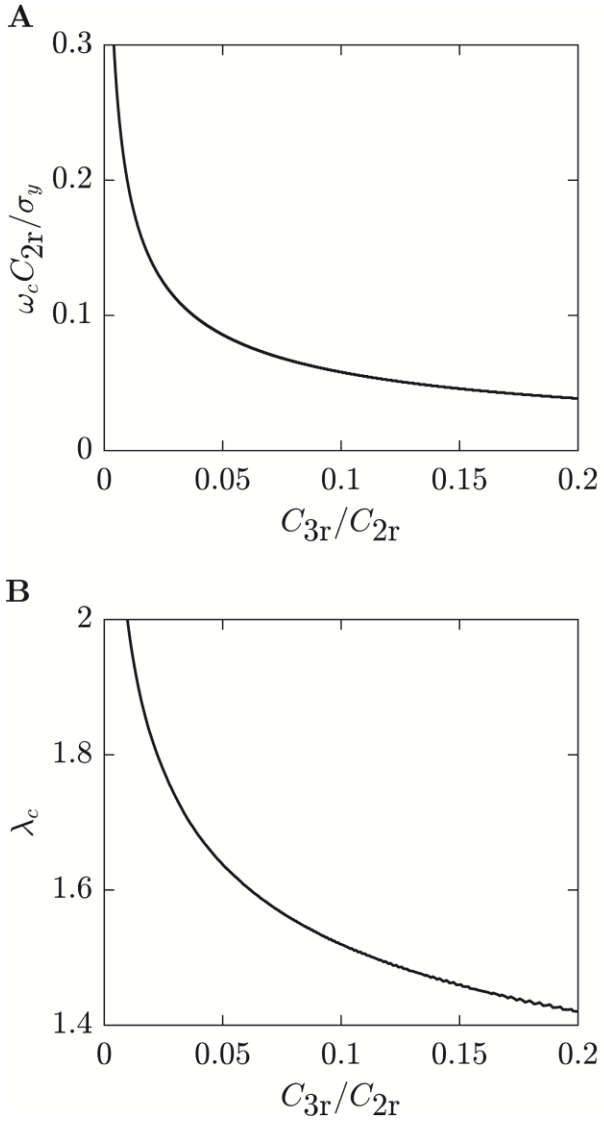

Figure 15: (A) The minimum rubber/plastic ratio to avoid necking (ω_c) in scaled form (see text) and (B) the corresponding critical stretch λ_c , both plotted against the ratio of two rubber material parameters C_{3r}/C_{2r}.

The first practical message from the previous sections is that a rubber layer can altogether eliminate the necking of the plastic. The analytical model offers a simple way to estimate the thickness of rubber needed (i.e. the ω value needed) to enforce homogeneous deformation: ω_c is

the minimum rubber-plastic thickness ratio (ω) required to make the nominal stress response monotonic. Appendix (Eqn. A2-12) proves that for a given plastic, the quantities $\omega_c C_{2\mathrm{r}}$ and λ_c do not depend on C_{2r} and C_{3r} separately, but on the ratio $C_{3\mathrm{r}}/\,C_{2\mathrm{r}}$. Thus master curves of $\omega_c C_{2\mathrm{r}}/\sigma_y$ and λ_c vs $C_{3\mathrm{r}}/C_{2r}$ can be constructed readily (Figure 13), and thus ω_c needed for from any choice of rubber can be identified. For example, at fixed $C_{2\mathrm{r}}$, Figure 15A shows that ω_c reduces strongly with increasing $C_{3\mathrm{r}}/C_{2r}$ at small values of$C_{3\mathrm{r}}/C_{2r}$. Recognizing that the modulus is almost entirely determined by C_{2r} (Eqn. 3.12), this means that at fixed modulus, if the rubber is even slightly strain hardening, a small rubber thickness is sufficient to eliminate necking.

However, bonding a rubber layer may be useful for improving the failure resistance of the plastic layer even if necking is not completely eliminated. To illustrate this, Figure 16A redraws the state diagram of Figure 9C but superposes the Von Mises effective stress in the plastic layer as a color map. Here the effective stress is calculated as:

$$\sigma_{\mathrm{e,p}}(\lambda_{\mathrm{app}}) = \begin{cases} \sigma_{\mathrm{p}}(\lambda_{\mathrm{app}}) & \text{, if } \lambda_{\mathrm{app}} < \lambda_{\mathrm{peak}} \quad i.e.\, homogenous\ deformation \\ \sigma_{\mathrm{p}}(\lambda_{\mathrm{neck}}) & \text{, if } \lambda_{\mathrm{peak}} \le \lambda_{\mathrm{app}} \le \lambda_{\mathrm{neck}} \quad i.e.\, necked\ state \\ \sigma_{\mathrm{p}}(\lambda_{\mathrm{app}}) & \text{, if } \lambda_{\mathrm{app}} > \lambda_{\mathrm{peak}} \quad i.e.\, homogenous\ deformation \end{cases} \tag{3.13}$$

Outside of the stable drawing envelope, deformation is homogeneous and hence the constant-stress contours are horizontal because stress only depends on the applied stretch. In contrast, inside the envelope where the material bifurcates into two coexisting phases, the constant-stress contours are vertical since they do not depend on the applied stretch, but only on the material and geometric properties.

Consider now a plastic with a failure stress of $\sigma_{\mathrm{e,p}} = 60\ \mathrm{MPa}$, a value that exceeds the stress in the necked region of a free-standing plastic layer. Accordingly, a free-standing plastic layer fails as soon as the neck initiates, i.e. at only a few percent strain. Bonding a rubber layer

reduces the stress in the plastic, and Figure 16A shows that at $\omega = 1.1$, the stress in the plastic layer during stable drawing is below the assumed failure value. Thus, rubber bonding may be an effective toughening mechanism, i.e. may force ductile deformation in a plastic that is relatively brittle.

Finally, the ability of the rubber layer to reduce stress in the plastic depends almost entirely on the strain hardening characteristics of the rubber at large strain, not on its small strain behavior. This is illustrated in Figure 16B-D. Figure 16D shows the nominal stress-strain behaviors of three different rubbers dubbed r, ra, and rb. The rubber material properties $C_{2\mathrm{r}}$ and $C_{3\mathrm{r}}$ are listed in Figure 16. The rubber r corresponds to the same properties as used in most of this paper. The rubber ra has nearly the same modulus as r but no strain hardening, whereas rb has the same strain hardening behavior as r, but zero $C_{2\mathrm{r}}$.

Figure 16B&C show the boundaries of the coexistence regions for ra and rb respectively. The minimum rubber thickness value needed to avoid the necking of the plastic layer are seen to be $\omega = 29.9$ for ra and $\omega = 98.4$ for rb. i.e. both these rubbers require a large thickness to eliminate necking. However, to avoid failure (i.e. keep $\sigma_{\mathrm{p,eff}} = 60\ MPa$), the ω values needed are 39.3 for ra and 1.4 for rb; the latter value is not much larger than for the rubber r, which was 1.1. Clearly, reducing the degree of strain hardening of the rubber greatly increases the rubber thickness needed to avoid failure, whereas reducing the rubber modulus has little effect. This is not surprising: since λ_{neck} values for the plastic are quite high, the low-strain behavior of the rubber does not play a significant role. Indeed, some polymeric plastics can have λ_{neck} values exceeding 10(Andrews & Ward, 1970; Seguela, 2007), especially at elevated temperatures. In such situations, the rubber would be forced into an extremely high-strain state, and even very thin rubber layers may significantly reduce the stress in the plastic. In summary, for improving failure resistance

during drawing, one needs to add a layer with high large strain-strain hardening, whereas its small strain behavior is nearly irrelevant.

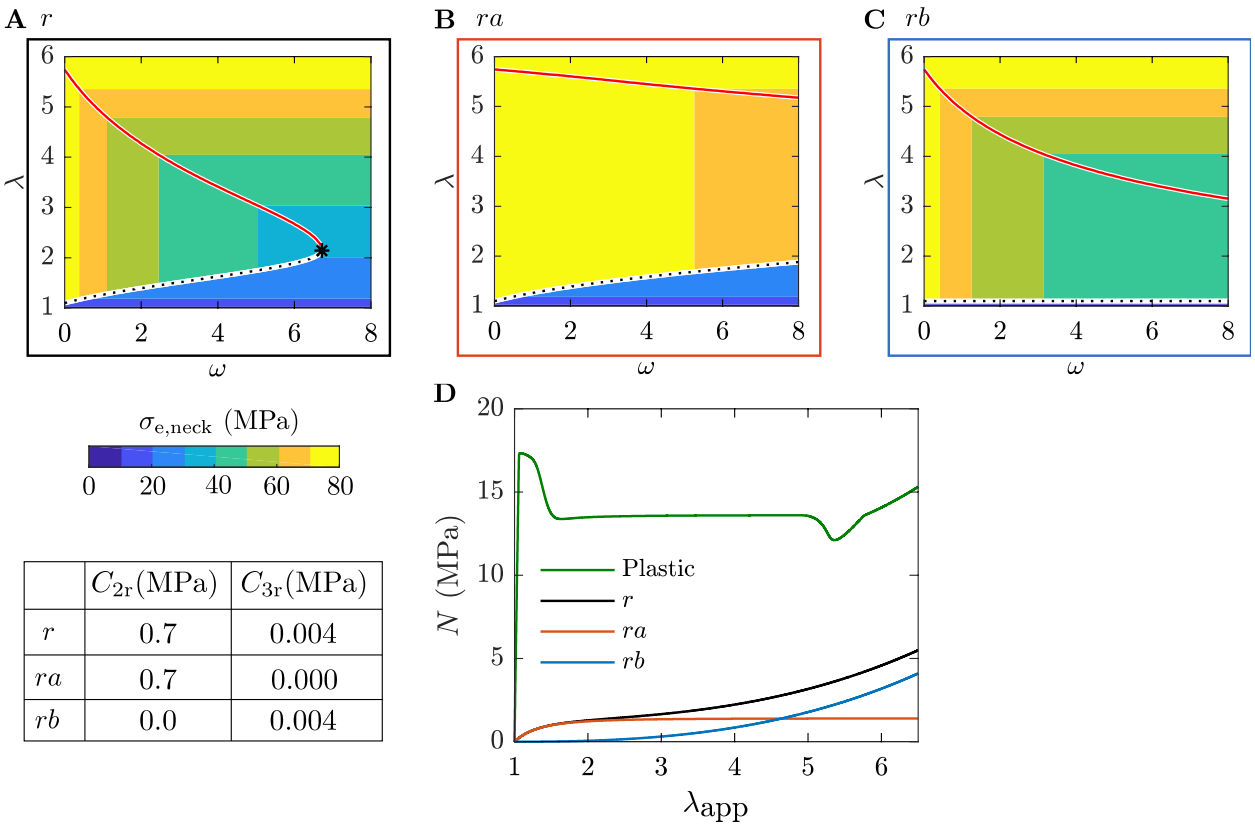

	C_{2r}(MPa)	C_{3r}(MPa)
r	0.7	0.004
ra	0.7	0.000
rb	0.0	0.004

Figure 16: (A, B, C) Envelope of stable drawing for rubber/plastic composites with three different rubbers of properties in the table. (D) Engineering stress-strain behavior of the three rubbers.

3.5 Summary and Conclusions

We adapted an energy-based model, originally developed to capture the behavior of unsupported plastics, to rubber-plastic laminate composites. This model quantitatively captured some of the key parameters predicted by the simulations, including the engineering stress (or force)

needed for drawing, the stretch at which the neck first appeared, and the stretch of the necked region during stable propagation. However, because the model ignores inelastic deformation (i.e. plasticity), it underpredicts the stretch of the unnecked region. An improved prediction was obtained by including the effects of irreversible deformation explicitly in the energy model. The results from finite element simulations validate the model.

The two most interesting insights from this article are :

- The stable drawing behavior of the laminate composites can be regarded as the coexistence of two states, analogous to the thermodynamic phase transition that ends in a critical point. The envelope of this two-state region as layer thickness is varied strongly resembles a typical two-phase region, e.g. of a gas-liquid transition.
- Strain hardening rubber layer can reduce the stress in the plastic layer, even when the rubber is too thin to eliminate necking. Therefore, even a modest amount of elastomer may inhibit failure of the plastic layer during drawing.

4.0 Fracture of Rubber-Plastic Laminates

4.1 Introduction

Polyethylenes, such as HDPE (High-Density Polyethylene), are one of the most widely used polymers globally(Malpass, 2010). They are cheap(Pascu, 2005), have good processability(Pascu, 2005), chemical resistance(Pascu, 2005) and are bio-compatible(Fouad & Elleithy, 2011). They are widely used for applications like pipe and fittings(Nguyen et al., 2021), biomedical applications(Fouad & Elleithy, 2011), and others(L. Wang et al., 2019). Further, polyethylene films are extensively used in the packaging industry(Nisticò, 2020). These films are ductile and can undergo extreme inelastic deformations by the process of necking, and neck propagation called cold drawing(Argon, 2013b; Carothers & Hills, 1932). However, high-density polyethylene films exhibit limited flaw tolerance(Bartczak et al., 1999). A better understanding of the fracture processes becomes imperative in the interest of flaw tolerance. However, research is not conclusive on the fracture of HDPE and other polyethylene films, where the material undergoes extreme inelastic deformation.

Like ductile polymers, soft elastic materials like elastomers(Lee et al., 2017) and gels(Calvert, 2009) can deform to large stretches, albeit recoverable and without necking. Beyond traditional uses in tires, gaskets, and adhesives, such soft materials are extensively studied for applications like soft robotics(Abdullah et al., 2018; Coyle et al., 2018), stretchable electronics(Arafat et al., 2015, 2016) etc. In contrast to HDPE, a soft elastic material undergoes elastic blunting(Hui, A, Bennison, & Londono, 2003) and shows good flaw tolerance (C. Chen et al., 2017). Although, when it fractures, the crack propagation can be unstable.

Tensile deformation of HDPE films occurs by necking and neck propagation (Crist & Metaxas, 2004; Hutchinson & Neale, 1983), where the necked region is stiffer and less ductile(Argon, 2013b). The tensile deformation of a HDPE film and HDPE-SEPS trilayer film with a rubber fraction, ζ = 0.35 at a nominal stretch rate of 1 s^{-1} is shown in Figure 17A. At this relatively large, applied strain rate, the HDPE undergoes necking and starts further deformation by neck propagation. However, the neck may not propagate throughout the length of the gauge section of the dogbone specimen. Instead, after some propagation, the material often fails at the boundary separating the necked region from the rest of the specimen. The partial neck propagation and the failure are reflected in the nominal stress plot in Figure 17B by the plateau, followed by the fall in the nominal stress. In contrast, an HDPE-SEPS (Styrene-Ethylene-Propylene-Styrene) trilayer film of rubber fraction, ζ = 0.35, under the same condition, can propagate the neck throughout the gauge section of the specimen (Figure 17A). Since the trilayer sample does not fail, the plateau of nominal stress is sustained to a large nominal strain Figure 17B. Thus, bonding a layer of SEPS rubber allowed the HDPE to stretch in conditions that would otherwise have resulted in failure. Understanding the improved stretchability of the HDPE by bonding a soft elastic layer is the objective of this chapter.

Details of the fracture of HDPE can be obtained by a video imaging of an HDPE film with a preexisting sharp notch. Fracture of HDPE involves the formation of a neck-like, highly stretched plastic zone ahead of the notch followed by a crack initiation in the process zone (Figure 17C). Moreover, the plastic zone forms a sharp boundary with the bulk, where the specimen thickness changes a lot over a small length. At the same applied displacement, there is no crack insipient in the neck-like deformation zone formed at the notch tip in a laminate of ζ = 0.6 (Figure 17C). In contrast to HDPE, the fracture in elastomers occur at the crack tip (Creton & Ciccotti, 2016) due

to chain scission or cross-link failure after significant elastic blunting(Hui et al., 2003). Hence, in the presence of defects, the increased stress in the rubber layer magnified at the flaw tip can be an alternate pathway for the composite failure. Furthermore, inelastic deformation can also be a toughening mechanism because of the energy dissipation (Anderson). All these factors warrant a comprehensive quantitative study on the fracture of HDPE-rubber laminate and potential toughening effects.

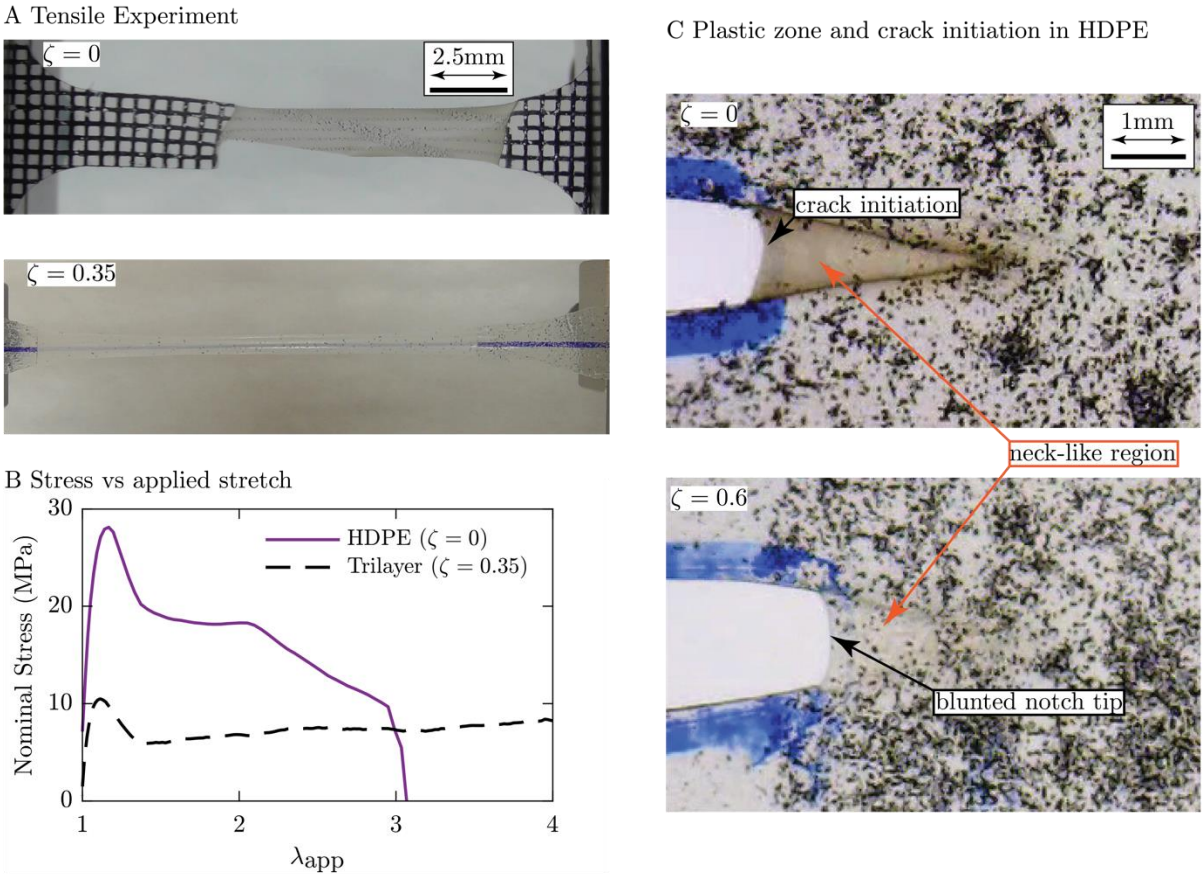

Figure 17: (A) HDPE undergoing failure by tearing at the boundary of the necked region when deformed at a nominal stretch rate of 1 s^{-1}. HDPE-SEPS trilayer of rubber fraction (ζ) of 0.35 drawing without failure when deformed at a stretch rate of 1 s^{-1}. (B) The nominal stress vs applied stretch (λ_{app}) plot for the HDPE and HDPE-SEPS trilayer experiments in (A). The nominal stress of HDPE drops to zero MPa following the fracture. (C) Notch tip deformation in HDPE and trilayer (ζ = 0.6) specimens at an applied displacement of 2 mm. Crack is insipient in the HDPE, whereas the notch is blunted in the laminate.

This study is composed of experiments followed by finite element simulations to study the stress state in the process zone. The elastomer SEPS was bonded to HDPE to create SEPS-HDPE-SEPS trilayer. First, the flaw tolerance in free-standing HDPE and SEPS films, as well as HDPE-SEPS trilayer films, is quantified by introducing sharp cracks and blunt holes of various sizes in tensile specimens and stretching them to check for failure. Since HDPE and SEPS have contrasting failure behavior, we perform fracture experiments to understand the fracture behavior of the laminates. Process zone evolution, crack initiation, and stability of crack propagation, of all the materials, is studied. Finally, finite element simulations of HDPE, SEPS, and HDPE-SEPS trilayer of various rubber fractions are conducted to quantify the stress state and the role of rubber fraction.

This chapter is arranged as follows. Section 4.2.1, 4.2.2, and 4.2.3 discuss the experimental methods, material modeling, and finite element procedures, respectively. Section 4.3.1 presents the flaw tolerance map of the SEPS-HDPE trilayer with SEPS fraction. Section 4.3.2 reports the results from fracture tests. The crack initiation mechanism in HDPE and the laminates are reported in 0. Meanwhile, Section 4.3.3 reports the experiments on process zone kinematics. Section 4.4.1 present the stretch and stress triaxiality in the tensile test. Meanwhile, Section 4.4.2 present the stress and stress triaxiality in the fracture test.

4.2 Methods

4.2.1 Experimental Methods

HDPE and HDPE-SEPS-HDPE trilayer sheets with various rubber thickness fractions (ζ) were prepared by continuous extrusion in a multilayer coextrusion die by Dr. Deepak Langhe,

Polymer Plus, Akron, OH. Free-standing SEPS sheets were solvent cast. Dog bone-shaped tensile samples were then punched out using a die in the machine-direction. Three sets of experiments were conducted on the pure material dogbone samples as well as the composites. The first was a simple tensile test with sharp edge notches, and holes punched at the center. The sharp notches were cut into the edge of dogbone samples using razor blades, whereas the holes were punched. The depth of the cut was monitored under an optical microscope. All tensile tests were done on an MTS universal tensile testing platform. The samples were mounted and pulled with a grip velocity of 50 mm/min. Fracture tests were performed on 25 mm wide and 10 mm wide samples (grip to grip). The initial sharp notches were made with a razor blade and had a length of 10 mm.

4.2.2 Material Model

The SEPS rubber is modelled using a two-parameter rate insensitive incompressible hyperelastic model. The strain energy density function is described as a function of the first (I_1) and second (I_2) invariant of the Right Green Cauchy strain tensor ($\boldsymbol{C} = \boldsymbol{F}^T\boldsymbol{F}$) as in Eqn. 4.1.

$$\psi^r = C_1^r(I_2 - 3) + C_2^r(I_1 - 3)^2 + \frac{\kappa}{2}(J - 1)^2 \tag{4.1}$$

In Eqn. 4.1, J is the determinant of the deformation gradient, and κ is an internal penalty parameter to volume change. The constitutive parameters, C_1^r and C_2^r were evaluated by fitting the simulated nominal stress response with the experimental response. The SEPS was modelled using the values C_1^r = 0.6 MPa and C_2^r = 0.05 MPa. The fit is shown in Figure 18.

Inspired from the structure of semicrystalline materials, the HDPE was modelled assuming that the mechanical response is the linear combination of the amorphous and crystalline phases (Vandommelen, Parks, Boyce, Brekelmans, & Baaijens, 2003). The amorphous phase was

modelled using a rate insensitive incompressible hyperelastic strain energy density function given in Eqn. 4.2.

$$\psi^a = C_1^a(I_1 - 3) + C_2^a(I_1 - 3)^2 + \frac{\kappa}{2}(J-1)^2 \tag{4.2}$$

Meanwhile, the crystalline phase was modelled as an elastic-plastic material. The crystalline phase was modelled using a rate-independent incompressible NeoHookean strain energy density function as in Eqn. 4.3. The kinematics of plastic deformation was implemented by multiplicative decomposition of the deformation gradient into elastic and plastic components, $\boldsymbol{F} = \boldsymbol{F}_e\boldsymbol{F}_p$. The subscript *e* and *p* represent the elastic and plastic parts, respectively.

$$\psi^c = C_1^c(I_1 - 3) + \frac{\kappa}{2}(J-1)^2 \tag{4.3}$$

The plastic flow was defined by the isotropic linear hardening yield function as in Eqn. 4.4. $\boldsymbol{M}_e^d$ is the deviatoric component of the Mandel Stress defined as$\boldsymbol{M}_e = \boldsymbol{C}_e\boldsymbol{S}_e$. Where, $\boldsymbol{C}_e = \boldsymbol{F}_e^T\boldsymbol{F}_e$, $\boldsymbol{S}_e = \frac{\partial\psi^c(\boldsymbol{C}_e)}{\partial\boldsymbol{C}_e}$ are the elastic part of Right Green Cauchy strain tensor and Second Piola Kirchhoff Stress tensor respectively. Further, ϵ_p, σ_y and H are the internal plastic parameter, yield stress and the linear strain hardening parameter.

$$f(\boldsymbol{M}_e, \epsilon_p) = \sqrt{\frac{3}{2}\boldsymbol{M}_e^d : \boldsymbol{M}_e^d} - [\sigma_y + H\epsilon_p] = 0 \tag{4.4}$$

The constitutive parameters C_1^a, C_1^c, σ_y and H were identified by fitting the simulated nominal stress response with the experimental response. The HDPE was modelled using the parameter values C_1^c = 14 MPa, σ_y = 14 MPa, H = 13 MPa, C_1^a = 0 MPa and C_2^a = 0.014 MPa. The fit is shown in Figure 18.

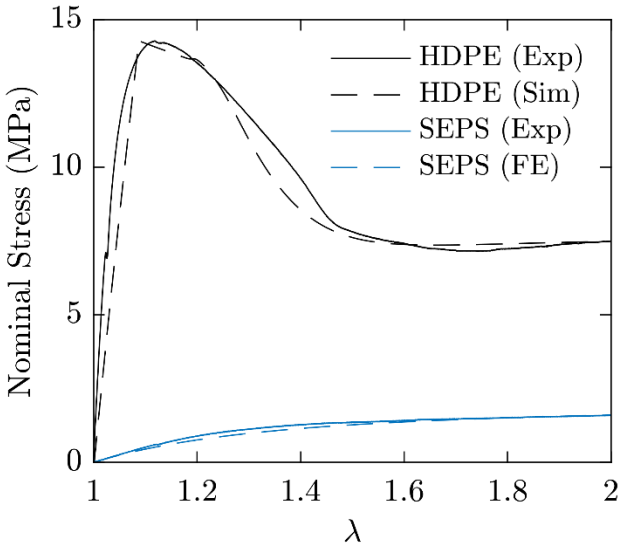

Figure 18: Simulated and experimentally measured nominal stress- stretch plots for HDPE plastic and SEPS rubber.

4.2.3 Simulation Methodology

Finite element simulations were conducted to study the stress state in simple tensile tests as at sharp crack tips and holes. A custom highly parallelized 3D quasistatic nonlinear Finite element code was used. It was previously used to study neck propagation(Rahul G. Ramachandran et al., 2020) and wrinkling(Yang et al., 2017) in rubber-plastic laminates. The finite element meshes used for simple tension simulations, fracture simulations, and simulation of a unit cell with a center hole are shown in Figure 19A, B, and C, respectively. Exploiting the symmetry of the geometries, only the quarter of the tensile specimen, half of the fracture specimen, and the quarter of the unit cell with a hole was modelled. Roller boundary conditions were imposed on the symmetry planes.

Single-layer geometries of 50 μm thickness of the three cases were created to simulate free-standing SEPS and HDPE behavior. Trilayer geometries with different SEPS fractions were

created for all three cases while keeping the HDPE layer thickness constant at 40 μm. All the meshes had two elements per layer along with the thickness (not shown in Figure 19).

The tensile geometry was meshed using 37620 3D hex elements. The mesh was refined at the center of the specimen to capture the necking and also the sharp boundary of the necked region (Figure 17A). The fracture geometry was meshed using 49396 3D hex elements. The mesh was refined at the crack tip and ahead of the crack in the plane of the notch to capture the plastic zone (Figure 17B). The notch tip radius was 50 μm.

The component of Cauchy stress tensor and the stress triaxiality defined as in Eqn. 4.5 were recorded.

$$\sigma_{tri} = \frac{\sigma_m}{\sigma_{eq}} \tag{4.5}$$

where, $\sigma_m = \frac{1}{3} trace(\boldsymbol{\sigma})$ is the mean stress of Cauchy stress tensor ($\boldsymbol{\sigma}$) and $\sigma_{eq} = \sqrt{\frac{3}{2}\boldsymbol{\sigma}^d : \boldsymbol{\sigma}^d}$ is the effective stress. $\boldsymbol{\sigma}^d$ is the deviatoric component of the Cauchy stress tensor.

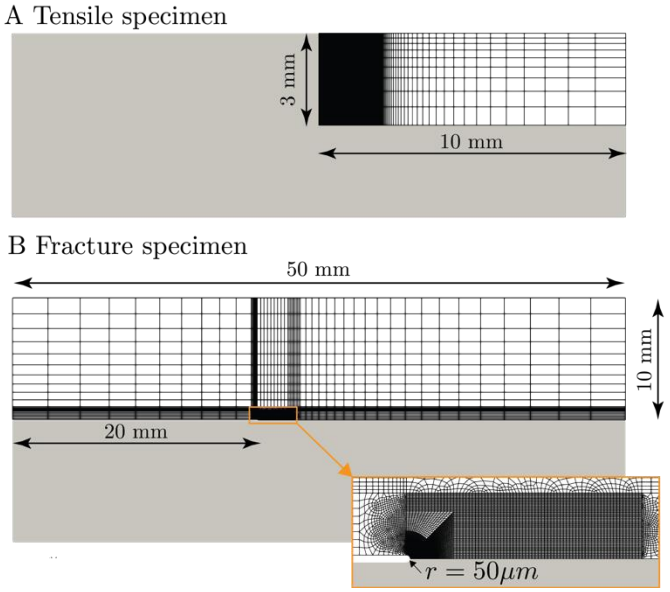

Figure 19: Finite element mesh for (A) simple tensile specimen, (B) fracture geometry, (C) and unit cell with a hole in the center.

4.3 Results

4.3.1 Flaw Tolerance Map

The stretchability of HDPE, SEPS, and HDPE-SEPS trilayer films of various rubber fractions was tested by preparing tensile specimens with controlled defects and stretching them to an applied stretch of 3. The flaw tolerance maps for tensile specimens with sharp notches as well as center holes are plotted in Figure 20A and B respectively. The flaw tolerance maps were created by marking whether the sample was able to stretch without failure (marked by green circles in Figure 20) or not (marked by red 'x' symbol in Figure 20) for a given defect dimension and rubber fraction, ζ in the composite. The ζ = 0 and 1 correspond to free-standing HDPE and SEPS films, respectively.

Free-standing HDPE films did not show flaw tolerance for any of the size of sharp notches as well as hole sizes tested. The smallest of sharp notches (~0.1 mm length) and the smallest of holes (~0.12 mm diameter punch) that could be made by our procedures propagated under tension, and the specimen failed. In contrast, for the applied stretch of 3, the rubber did not fail even for the largest hole size tested, whereas it failed for sharp notches of length exceeding 0.4 mm.

In the trilayer composites, however, the defect size for causing failure increased with increasing rubber fraction in the laminate. For sharp notches in Figure 20A, the flaw tolerance regime shifts to a larger crack size with increasing rubber fraction. Similar behavior is evident for samples with holes (Figure 20B), except that composite with a high rubber fraction generally avoided failure even to the largest hole sizes tested.

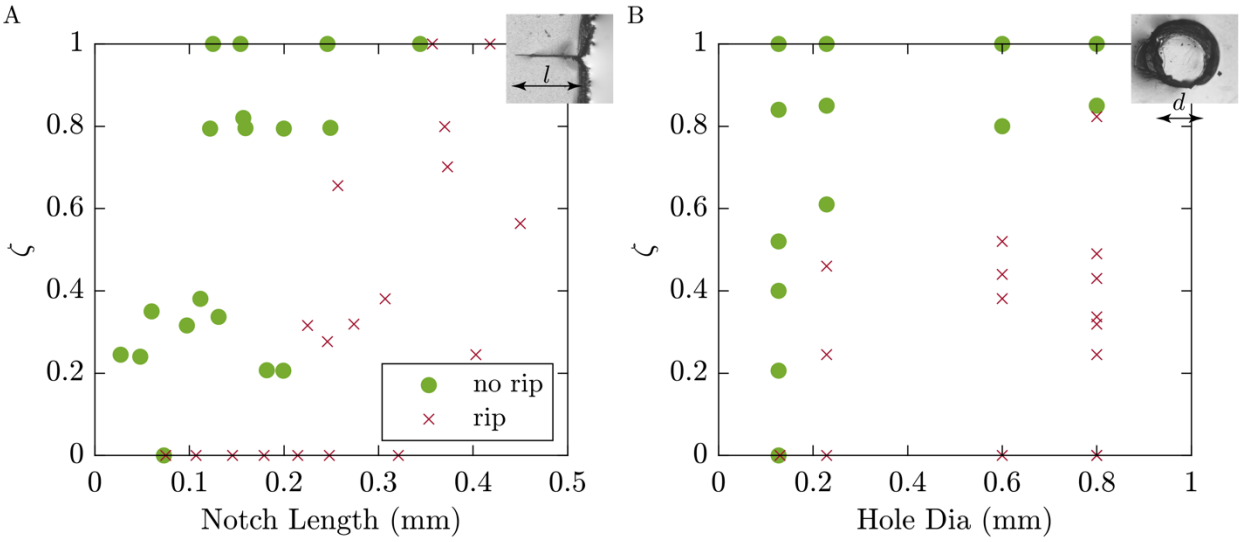

Figure 20: Flaw tolerance map plots whether the sample could successfully stretch without failure with defect size and rubber plastic ratio. (A) Notch length (*l*) (B) hole diameter (*d*)

As shown in Figure 20, the addition of rubber improved the stretchability of the HDPE film. Further, the stretchability improved with increasing rubber thickness. However, apart from the improved stretchability, the failure mechanics also was affected by the rubber fraction in the composite. In HDPE film free-standing, the crack propagation was observe4d to be stable, i.e., the load first increased as the sample was stretched and then decreased gradually as the crack propagated. In contrast, the crack propagation in SEPS rubber was abrupt and unstable, and the load reduced from a peak value to zero discontinuously as the sample ruptured. The HDPE-SEPS showed a transition of behavior from stable to unstable behavior with increasing rubber content. The goal of the following sections is to examine in greater detail the various local phenomena that contribute to this flaw tolerance map.

4.3.2 Fracture of HDPE, SEPS, and HDPE-SEPS Trilayer Films

In HDPE film, yielding creates an inelastically deformed region ahead of the notch tip called the "plastic zone". However, in the composites, the deformation ahead of the notch is not completely plastic, and hence the more general term "process zone" is adopted here. The first set of experiments was conducted to visualize the process zone and simultaneously measure the load-displacement curve of notched samples. Experiments were conducted on rectangular specimens 25 mm wide with sharp notches of 10 mm in length. The clamps were initially separated by 15 mm. A straight line of blue ink was laid on the crack plane to easily visualize the process zone deformation, and additional ink markers were placed across the surface of the sample to visualize deformation outside of the process zone.

The fracture of HDPE, SEPS, as well as HDPE-SEPS trilayer films, along with the normalized force-displacement curves, are shown in Figure 21A-D, respectively. Each row in Figure 21A-D corresponds to different applied crosshead displacements (δ). The undeformed configuration is shown in the first row. The second, third, and fourth row correspond to a displacement of δ = 1.4 mm, 3.1 mm, and 8.6 mm, respectively. The normalized force-displacement curve corresponding to the experiments in Figure 21(A-D) is shown in Figure 21E. The force is normalized using the product of the thickness and ligament length of the specimen in the undeformed configuration (A_l).

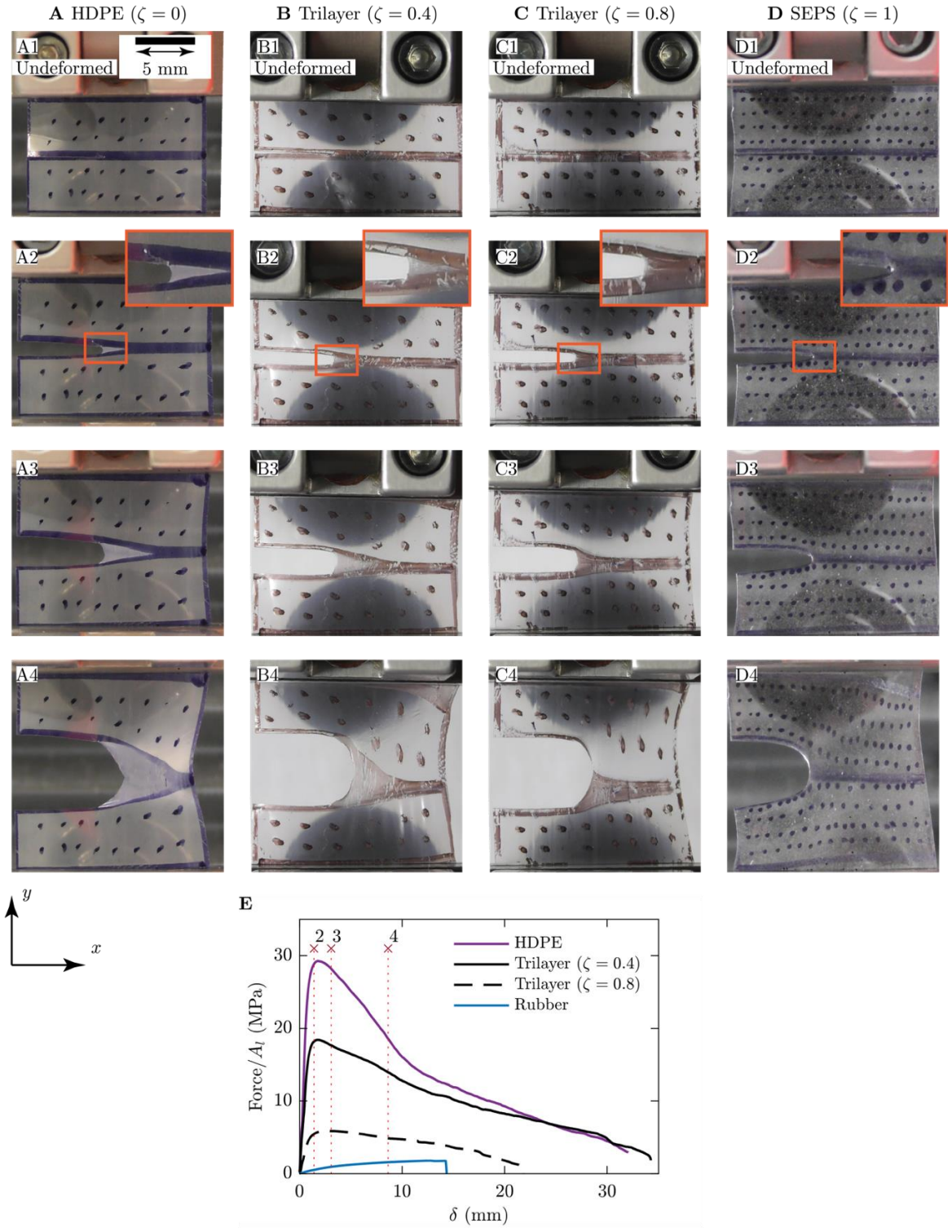

Figure 21: Fracture of (A) HDPE, (B&C) HDPE-SEPS trilayer films of ζ = 0.4 and 0.8 and (D) SEPS. (E) The corresponding force-vs-displacement curves, where force is normalized by ligament area A_l. The three vertical red dotted lines are the displacements corresponding to the lower three rows of images.

The fracture of free-standing HDPE film showed the following characteristics (Figure 21A). A triangular process zone formed at the tip of the sharp notch when the crosshead is displaced by δ = 1.4 mm (Figure 21 A2). Within this triangular region, the sample is severely stretched, indicated by its lighter hue as compared to the original line of blue ink. The transition from process zone to bulk is also sharp, i.e., within the resolution of the image, similar to the sharp edge of the necked region in tensile deformation in Figure 17. The normalized force curve for HDPE steadily rises to a peak around this displacement (Figure 21E). Further increasing the end displacement to 3.1 mm (Figure 21 A3) resulted in the growth of the process zone along the x and y directions marked in Figure 21. Concurrent with the growth of the process zone, the crack propagated inside the process zone. At δ = 8.6 mm (Figure 21 A4), the process zone grew to approach the free end of the specimen, while the crack continued its propagation in the process zone. A significant change in the slope of the normalized force curve is observed in Figure 21E after δ = 8.6 mm (marked 4). The gradual loss of load-carrying capacity with increasing deformation is a signature of stable crack propagation. Another important characteristic of the fracture of the HDPE film is that the deformation is almost completely localized in the process zone. This is evident from the lack of relative displacement of the ink markers outside the process zone in Figure 21A. Further, it is important to note that the material in the process zone gets pinned at its boundary even during crack propagation.

On the other extreme, the fracture of SEPS rubber is shown in Figure 21D. With the increase of δ (1.6 mm, 3.1 mm, and 8.6 mm), the notch progressively opened (Figure 21 D2 to D4). In contrast to HDPE, the significant opening of the notch mouth occurred without crack propagation, and the normalized force Figure 21E increased steadily with applied displacement.

Furthermore, there is large deformation concentrated at the notch mouth, and the deformation diffuses rapidly away from the crack tip. This is evident from the lack of relative displacement of the ink markers painted close to the plane of the notch. Also, there is no appreciable growth of the process zone with increasing δ. The normalized force for the SEPS increases with displacement as the crack mouth opens up, as shown in Figure 21D. This is followed by unstable crack propagation resulting in a rapid drop of the force curve to zero (Figure 21E).

Turning to the composites, at a relatively low rubber plastic ratio (ζ = 0.4), the fracture behavior in Figure 21B is qualitatively similar to HDPE (ζ = 0) in Figure 21A. An approximately triangular process zone is formed ahead of the notch tip, and the crack propagates within this process zone. However, there are some differences. Compared to the HDPE, the process zone has more diffuse edges and does not propagate as far ahead of the crack tip, whereas outside of the process zone, i.e., the material far ahead of the crack is deformed to a greater extent. The normalized force curve also shows a similar trend as that of HDPE but has a lower magnitude. The lower magnitude of the force curve results from the SEPS layer being significantly softer than the HDPE.

The fracture behavior of a composite with a large rubber fraction, ζ = 0.8, is shown in Figure 21C. The process zone at δ = 1.4 mm and 3.1 mm (Figure 21 C2 and C3) are smaller than that of the composite with ζ = 0.4 (Figure 21B2-3) and HDPE (Figure 21A2-3). The deformation in the process zone is also much smaller as compared to composite with ζ = 0.4 and HDPE. The deformation is judged by the gradient of the ink color. Furthermore, unlike HDPE and composite with ζ = 0.4, in the composite with ζ = 0.8, the crack did not start propagation at δ = 1.4 mm. However, unlike SEPS, the crack had started propagation at δ = 3.1 mm. i.e., the crack initiation happed at a larger applied displacement.

The fracture behavior of the composite with a relatively large rubber fraction, ζ = 0.8 (Figure 21C), is quite distinct from both HDPE and SEPS. Unlike HDPE film, the crack has not started to propagate at δ = 1.4 mm (Figure 21 C2). Further, in contrast to SEPS rubber, there is a visible modest process zone ahead of the crack tip where the deformation is significant. The deformation in the process zone, judging by the intensity of the paint color, as well as the size of the process zone, is smaller compared to HDPE film in Figure 21A2. At the next instance shown, i.e., δ = 3.1 mm (Figure 21 C3), the crack has started propagation, unlike the SEPS at the same applied displacement. Furthermore, the crack tip during propagation was observed to be curved, much like SEPS rubber. However, the crack propagation was stable, unlike SEPS rubber. The stable crack propagation is clearly evident from the gradual decrease in force in Figure 21E. Notch blunting and crack initiation

To differentiate notch blunting and crack initiation in the HDPE film and HDPE-SEPS trilayer films, we will focus on the deformation at the notch tip. The notch tip deformation in HDPE and HDPE-SEPS trilayer of ζ = 0.35 and 0.6 are shown in Figure 22 A, B, and C. Each row corresponds to a δ value of 1 mm, 1.5 mm, 2 mm, and 2.5 mm in Figure 22. The frames in Figure 22 are under one of two conditions, notch blunting or crack propagation. All the frames with crack propagation as judged from corresponding videos are marked by an orange background.

In HDPE, process zone formation blunts the notch in the first row (δ = 1 mm). At a δ = 1.5, the crack has initiated and propagates with further deformation. In HDPE, the crack initiates close to the process zone boundary rather than at the middle of the process zone. Meanwhile, for the trilayer with ζ = 0.35, the crack initiation is apparent only at a δ = 2 mm (the third row). Furthermore, for the trilayer with ζ = 0.6, the crack initiation is apparent only at a δ = 2.5 mm.

However, in the composites, the crack initiates at the middle of the process zone. The evolution of stretch in the process zone with time in the samples shown in Figure 22A-C is shown in Figure 6.

4.3.3 Process Zone Kinematics

The fracture experiment in Section 4.3.2 showed that a sharp notch creates a triangular process zone which is severely necked, and further loading causes growth of the process zone along the plane of the notch. Here we present a two-step experiment to visualize the deformation in the process zone with displacement. The two-step experiment was performed on specimens with a sharp edge notch (Figure 23), and with center holes (Figure 24). In the first step of the experiment, ink was applied along the notch plane (similar to Figure), and the sample was stretched until a process zone formed (Figure 23 A1 to D1). The stretching was then paused, and ink reapplied on the process zone. Then in the second step, stretching was continued (Figure 23 A2 to D2). This fresh layer of ink allows visualizing the deformation of the material that is already in the process zone.

For the HDPE film, the crack initiates inside the process zone (Figure 23A1) but off-center, close to the process zone boundary. The test is then paused, and ink is re-applied (Figure 23A2). Upon continuing stretching Figure 23A3 and A4 show a dark blue triangle (the original process zone from Figure 23A1) surrounded by a light blue boundary (material newly drawn into the process zone). This unambiguously shows that the material at the center of the process zone does not deform further; instead, the crack propagates in the newly-drawn material.

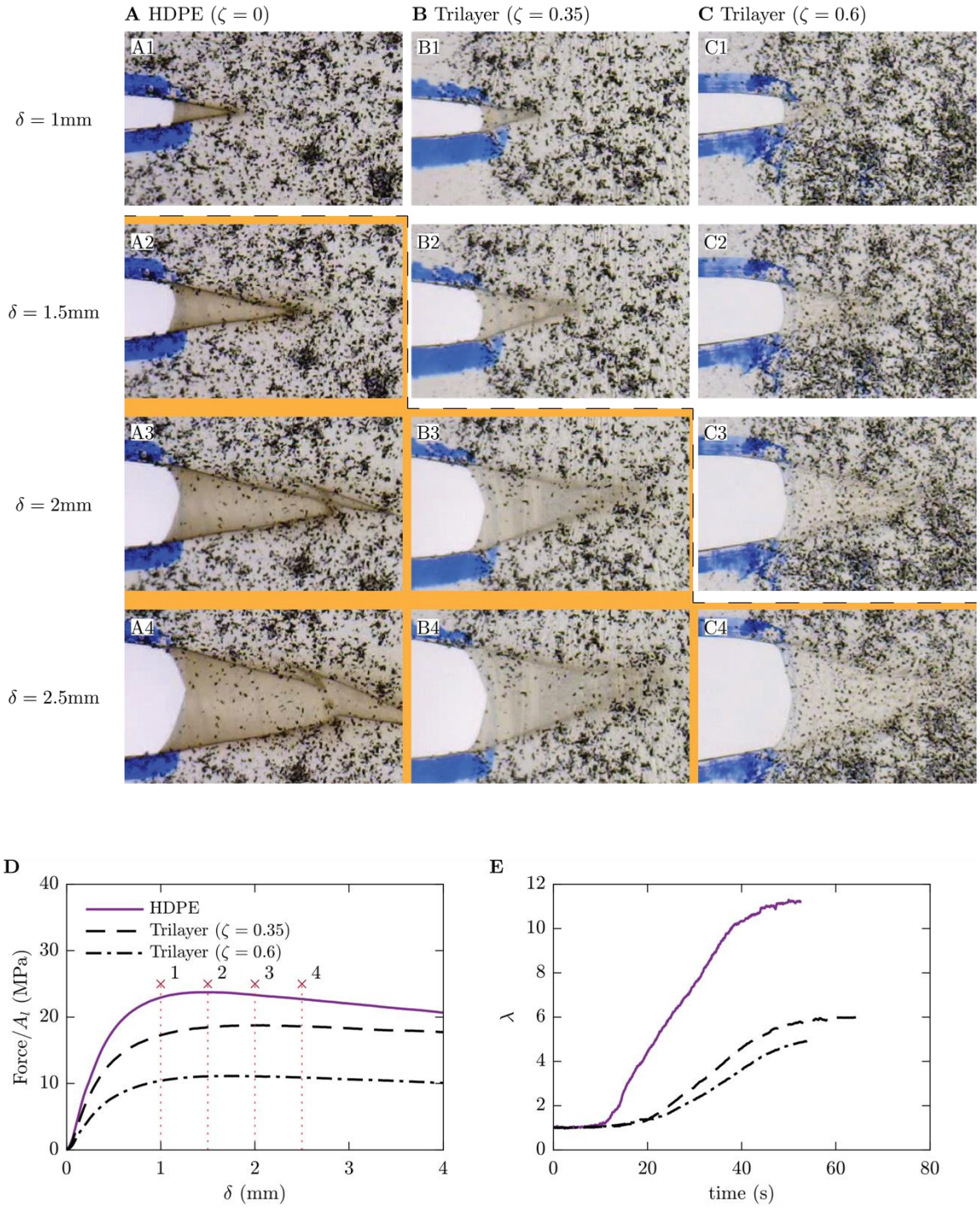

Figure 22: Process zone evolution in (A) HDPE, (B&C) HDPE-SEPS trilayer of ζ values 0.35 and 0.6. Frames that show crack initiation and propagation are marked with orange background. (D) The normalized force-displacement plot corresponds to the experiments in A-C. The displacement corresponding to each row is marked. (E) Stretch in the process zone evolution with time in the samples shown in Figure 22A-C.

Process zone configuration with further successive increase in applied displacement is shown in Figure 23 A3 and A4. The crack propagates in the process zone and the paint re-applied in the process zone remains unchanged in Figure 23 A3 and A4. This confirms, there is no further stretching of the process zone during the process of crack propagation.

In the other extreme, the notch in the SEPS rubber opens up without crack propagation (Figure 23D1-D4). As expected, there is no distinct process zone, and upon pausing and reapplying ink, the entire region ahead of the notch tip deforms further indicated by a global decrease in the blue hue. Unlike the HDPE, there is no crack propagation, at least up to the stretch examined in Figure 23.

Turning to the composites, at ζ = 0.4 (Figure 23B1-B4) is somewhat similar to that of HDPE, but with two important differences. First, upon reapplication of ink, the original process zone continues stretching, i.e. the stretching-direction growth of the process zone includes both new material drawn into the process zone, as well as stretching of the original process zone. Second, unlike in HDPE, the crack propagates approximately across the center. At ζ = 0.8, the behavior (Figure 23B1-B4) is very similar to the SEPS, except that the crack propagates along the center of the process zone (in SEPS the crack does not propagate at all).

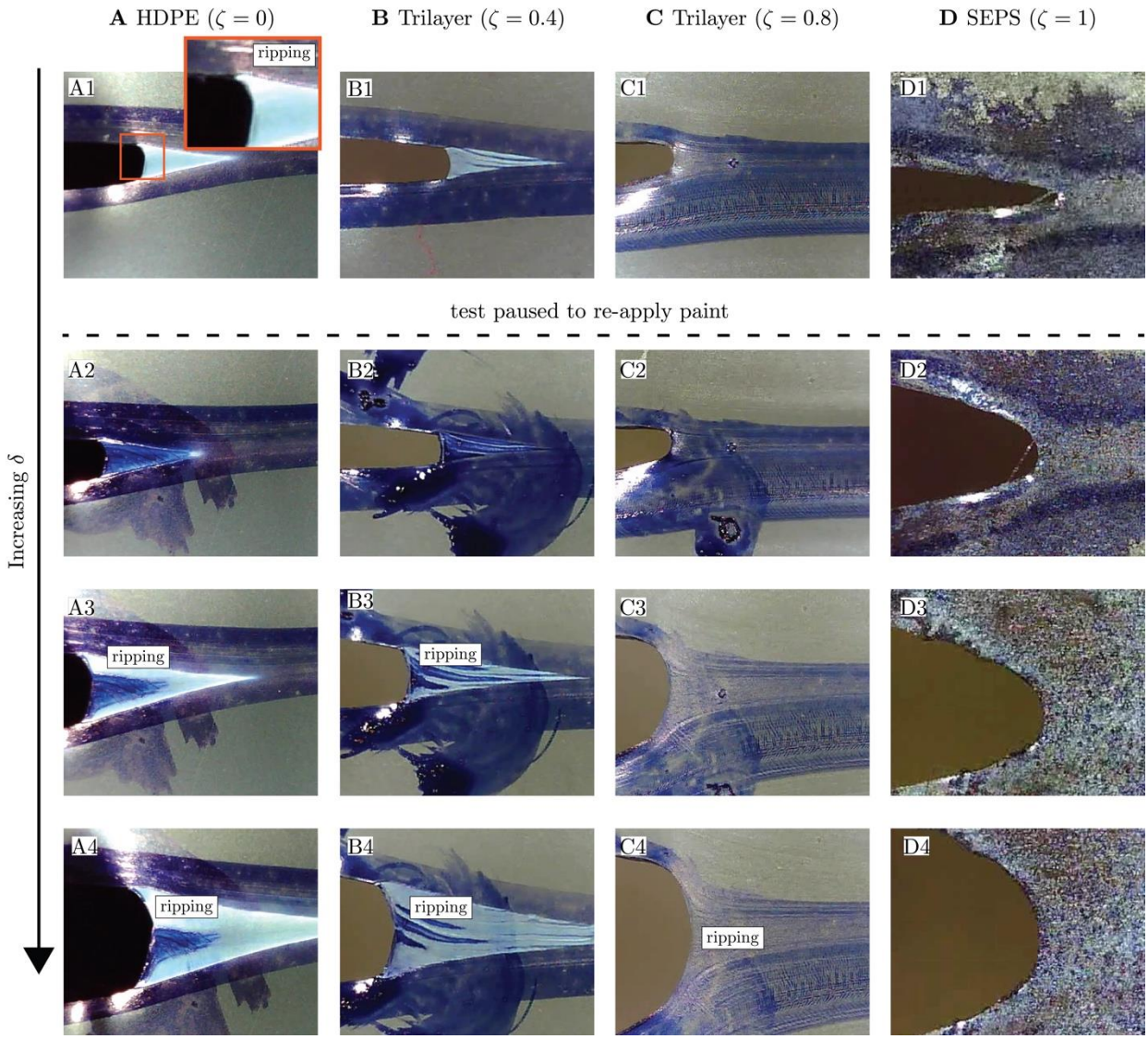

Figure 23: Process zone evolution in (A) HDPE, (B&C) HDPE-SEPS trilayer of ζ values 0.4 and 0.8, and (D) SEPS rubber, captured using a two-step experiment. First row shows the formation of process zone ahead of the crack. The test is then paused, and paint is reapplied on the material in the process zone (row 2). Evolution in the plastic zone with further stretching is shown in row 3 and row 4.

Process zone evolution ahead of hole is captured by repeating the two-step experiment presented in Figure 23 on tensile samples with center hole and is shown in Figure 24). The experiment is done for HDPE, HDPE-SEPS trilayer films of ζ = 0.4 and 0.8, as well as SEPS

rubber and is shown in Figure 24A-D respectively. The first row shows the undeformed configuration.

The overall process zone formation and its growth in specimens with center hole (Figure 24) is found to be qualitatively similar to that at a sharp notch (Figure 23). The two-step experiment in Figure 24 show that the formation of process zone is at the center of the hole and its propagation happens in both the two directions. The crack appeared in the HDPE with film only after the boundary of the process zone has almost completely traversed the height of the hole (Figure 24A). The crack initiate at the boundary of the process zone. Meanwhile, the process zone in the trilayer with ζ = 0.4 could traverse the height of the hole without failure (Figure 24B). Further, there is no visible process zone formation is seen in trilayer with ζ = 0.8 and SEPS (Figure 24C and D respectively). Also, the deformation in the ahead of the hole, (elongation of the hole in the vertical direction) reduced with increasing ζ.

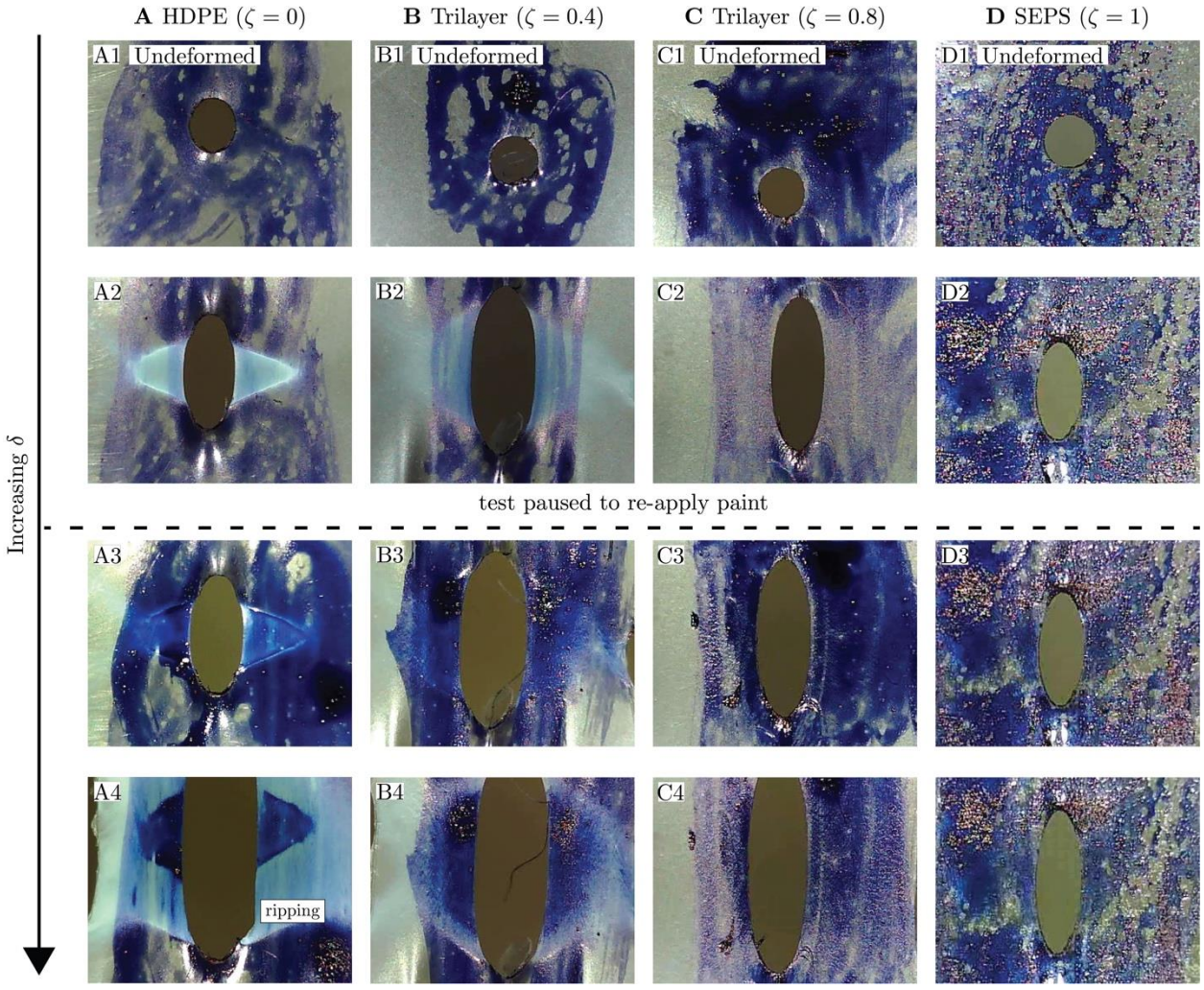

Figure 24: Plastic zone evolution in HDPE is captured using a two-step experiment in specimen with center hole. First row (A1 – D1) shows the undeformed configuration. (A2 – D2) In the second-row small cross head displacement is applied to allow the formation of a process zone. (A3 - D3) In the third row, the test is paused, and paint is reapplied on the material in the plastic zone. (A4 - D4) Evolution in the plastic zone with further stretching is shown in the fourth row.

4.4 Discussion

The ductile to brittle transition in HDPE has received considerable research attention(Krishnaswamy, 2005) (Kitao, 2001; O'Connell, Duckett, & Ward, 2002) (J. & B., 2006) (Ognedal, Clausen, Dahlen, & Hopperstad, 2014). The transition is decided by the competition of yielding and stress-triaxiality (Eqn. 4.5) at the crack tip. This is because stress triaxiality drives cavitation and void growth(Ognedal et al., 2014). Therefore, an increase in stress triaxiality reduces the local strain to failure (Bao & Wierzbicki, 2004; El-Sayed et al., 2001; Han et al., 2020). Factors like increasing temperature(Kitao, 2001; O'Connell et al., 2002) and decreasing strain rate (O'Connell et al., 2002) promote yielding in the material. Meanwhile, decreasing sample thickness(J. & B., 2006) or decreasing curvature of a notch(Fouad, 2010; Ognedal et al., 2014) decreases the stress triaxiality. Therefore, the material can behave more ductile with increasing temperature, decreasing strain rate, decreasing sample thickness, or decreasing the curvature of the notch root.

In Figure 17, it was shown that very large deformation rate could also initiate failure in a sample with no macroscopic defects. Introducing a sharp notch or a hole resulted in the failure of the film with tensile deformation (Section 4.3.1, 4.3.2) even at a slow rate. There are two characteristics common to all these different failures of the HDPE films. First, there is significant necking or neck-like process zone formation before failure. Second, the failure in the tensile specimen with and without macroscopic flaws initiated close to the boundary of the necked region or the neck-like process zone.

The thin free-standing HDPE film can undergo yielding even in the presence of sharp notches prior to failure. Therefore, there is no brittle fracture in the HDPE film. However, nonlinear strain hardening in the HDPE causes deformation in the neck-like process zone to arrest.

Thus, an increase in applied strain is accommodated by neck propagation. This was followed by crack initiation in the neck-like process zone. In the sample with holes, there was significant process zone growth before the crack initiation. However, in the specimen with a sharp notch, the crack initiation almost coincided with any process zone growth. The boundaries are locations of the extreme deformation gradient and hence become hot spots for stress triaxiality(G'Sell et al., 1983). Finite element results in the neck section are done to rationalize this failure observation.

A decrease in the stretch in the necked region with increase of rubber fraction in rubber-plastic laminates was shown in our previous publication(R. G. Ramachandran et al., 2018; Rahul G. Ramachandran et al., 2020). However, reduction of stretch in the neck and neck-like process zone with rubber fraction alone does not explain the improvement in the stretchability of the HDPE. Blending of elastomer into HDPE is a technique used to increase the toughness of HDPE. The improved toughness is due to micro-yielding observed at the interface of the matrix and blend(Bartczak et al., 1999). Similarly, the addition of a rubber layer is also found to reduce crazing in plastic(Hachisuka et al., 2019). This is because of the reduction in the stress triaxiality due to rubber addition. In this context, the effect of the rubber layer on the stress triaxiality during neck and process zone propagation needs attention. These aspects are further explored in detail in Sections 4.4.1and 4.4.2.

4.4.1 Stretch and Damage Parameter in Tensile Deformation

The longitudinal stretch (λ) and stress triaxiality (σ_{tri}) (Eqn. 4.6) is plotted for HDPE (ζ = 0), SEPS (ζ = 1) and trilayers of various ζ when deformed to an applied stretch of 1.5 is shown in Figure 25A and B respectively. The stress triaxiality (σ_{tri}) is averaged over the elements in the HDPE layer in the trilayer. The stretch is maximum at the center of the neck, and the magnitude

of the stretch decreases with increasing ζ. Meanwhile. The stress triaxiality, σ_{tri} has the highest intensity at the boundary of the neck (Figure 25B). The σ_{tri} also decrease with increasing ζ.

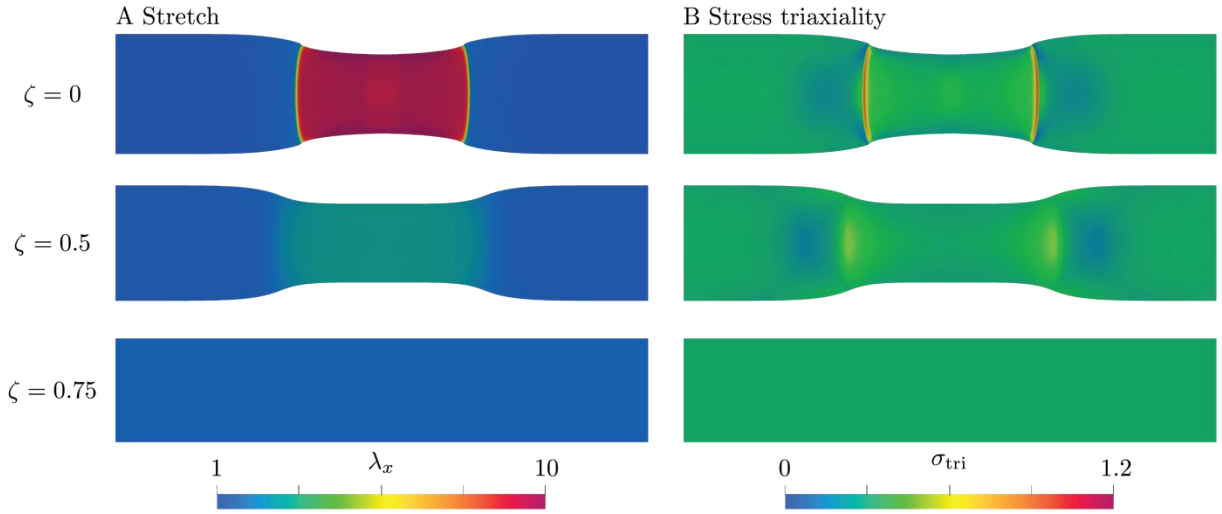

Figure 25: (A) Stretch and (B) damage function η is plotted for HDPE (ζ = 0), HDPE-SEPS trilayer of ζ values of 0.25, 0.5 and 0.75 as well as SEPS (ζ = 1). All the deformed configurations are at an applied stretch of 1.5.

4.4.2 Stretch and Stress Triaxiality in Fracture Specimen

The stretch contour is plotted on the deformed configuration at the notch tip in Figure 26A. HDPE, SEPS, and HDPE-SEPS trilayer of various ζ at different applied displacements (δ) are shown. The undeformed configuration is also shown in Figure 26. The process zone formation and its growth in HDPE are captured in the simulation. The propagation of the stretch contour is comparable to the experimental results in Section 0. The effect of rubber fraction ζ on the process zone kinematics observed in the experiments has also been well captured in the simulation. The size of the process zone decreased and started concentrating at the notch tip with increasing ζ.

The stress triaxiality contours for the specimen in Figure 26A are shown in Figure 26B. For the HDPE, the notch tip is a region of low triaxiality, while ahead of the notch tip in the plane of the notch as well as the borders of the process zone away from the plane of the notch become hotspots. With an increase in displacement, the low stress triaxiality region at the notch tip expands, with the triaxiality further concentrating at the process zone boundary. Failure in polycarbonate, a material that yields and strain harden like HDPE, has been reported to occur ahead of the notch tip in the notch plane(Gearing & Anand, 2004). But the experimental observations in this paper suggest that the failure occurs rather close to the process zone boundary (Figure 22A). This suggests that the combined factor of large stress triaxiality and large stretch at the notch boundary causes crack initiation.

The magnitude of the stress triaxiality is seen to reduce with increasing ζ. This explains the observation in Figure 22 B and C, where, unlike the HDPE, the crack initiation occurred close to the middle of the process zone.

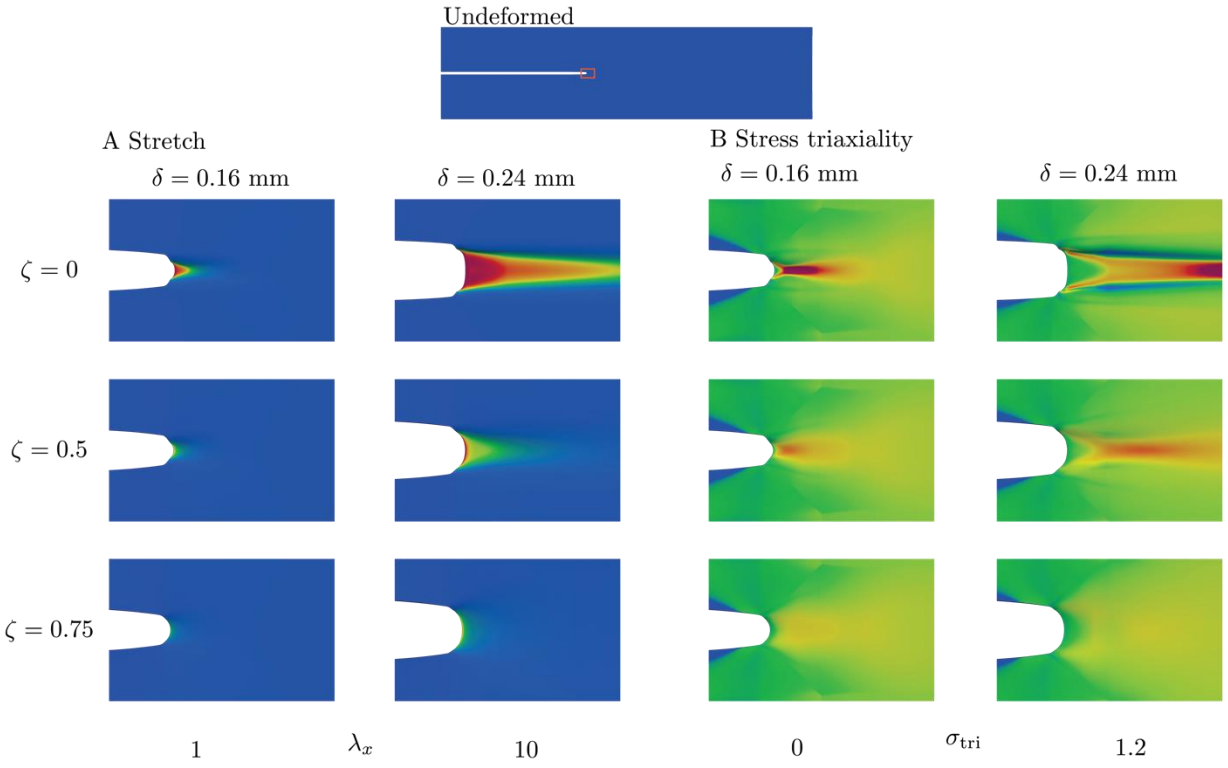

Figure 26: Deformed configuration of fracture specimen at different applied displacement, δ, for HDPE (ζ = 0) and trilayer films of various ζ = 0.5 and 0.75. (A) Stretch contour is plotted (B) Stress triaxiality is plotted.

4.5 Conclusions

HDPE films (approximately 40 μm thick) are flaw sensitive. Even the smallest defect we introduced (100 μm) caused the failure of HDPE in tension. Bonding a rubber layer improved the flaw tolerance of HDPE film, with the trilayer composite film able to tolerate increasing defect size with increasing rubber fraction in the composite. HDPE and HDPE-SEPS laminates showed stable crack propagation at all rubber fractions examined. Even though laminates with 80% rubber content showed process zone behavior close to that of free-standing SEPS, crack initiated at a

much smaller applied displacement as compared to free-standing SEPS. Further, unlike SEPS, which showed unstable crack propagation, even the laminate with 80% rubber content showed stable crack propagation. Thus, even a modest level of plastic is able to stabilize the crack propagation of the rubber.

Further, fracture experiments on HDPE and HDPE-SEPS trilayers films showed that these materials undergo notch tip blunting followed by crack initiation in the process zone. The crack initiation increased to large-applied displacement with increasing rubber fraction. Meanwhile, the crack initiation location changed from close to the process zone boundary in HDPE to the middle of the process zone in the laminates. The simulations of the neck propagation and HDPE fracture showed that the stress-triaxiality is high at these locations of crack initiations. Meanwhile, addition of rubber not only decreased the stretch in the process zone but also the magnitude of stress triaxiality.

5.0 Uniaxial Stretch-Release of Rubber-Plastic Bilayers: Strain Dependent Transition to Stable Helices, Rolls, Saddles, and Tubes

5.1 Introduction

When stretched, an elastomeric sheet stores the work done on it as elastic energy and recovers its original shape upon unloading. In contrast, a sheet of yielding material dissipates almost all the work of stretching, and therefore remains at or near its stretched configuration when unloaded. A composite bilayer composed of these two materials, when stretched and unloaded can bend out-of-plane, sometimes with interfacial buckling or wrinkling. This article is about the various mono-stable shapes with single or dual curvature formed by a uniaxial stretch and release of a rubber-plastic bilayer. The central focus of this article is to elucidate the role of inelastic deformation in the bending process.

Elastic strain mismatch within a material can trigger complex shape deformations. Hence it is a powerful tool for creating intricate shapes and structures. In nature, plants and animal tissues exploit growth-induced heterogenous elastic strain to create a myriad of static shapes and dynamic mechanisms. Opening of seed pods by elastic incompatibility(Armon et al., 2011), growing complex three dimensional features in internal organs(B. Li et al., 2011; Nelson, 2016), twisting of plant tendrils(Gerbode et al., 2012), curvatures in leaves(Liang & Mahadevan, 2009) and others(Katifori et al., 2010; Savin et al., 2011; Sharon & Efrati, 2010) are all examples of shape changes through inhomogeneous strain generation. Many researchers have sought to exploit such shape changes for engineering(Ionov, 2011; Kim et al., 2017; Klein, Efrati, & Sharon, 2007) and biomedical (Kanik et al., 2019; B. Li et al., 2011; Smela, Inganas, Pei, & Lundstrom, 1993)

applications. Heterogenous strain driven fabrication techniques have also found popularity in micro- and nano-scale fabrication(M. Huang, Cavallo, Liu, & Lagally, 2011; Leong, Benson, Call, & Gracias, 2008; W. Li et al., 2012; Smela et al., 1993), where it would be difficult to create intricate 3D shapes with conventional methods. Nano tubes and channels and many other three-dimensional shapes can be created through these techniques. Morphology changes driven by controllable strain gradients are also explored widely in the literature(Z. Chen, Majidi, Srolovitz, & Haataja, 2011; Douglas P. Holmes, 2019; D. P. Holmes, Roche, Sinha, & Stone, 2011; Smela, Inganas, & Lundstrom, 1995; van Manen, Janbaz, & Zadpoor, 2018).

Much previous research on shape changes has created a strain mismatch by applying a uniform stimulus to a heterogeneous structure. A common example of this mechanism is the bimetallic strip sometimes used in household thermostats. A bimetallic strip is made by bonding two metals with unequal thermal expansion coefficient. When heated, the strip bends into an arch, with the metal with higher thermal expansion coefficient material on the outside. Instead of thermal expansion, other stimuli such as differences in solvent swelling of the layers (Geng & Selinger, 2012; Z. Hu, Zhang, & Li, 1995; W. Li et al., 2012; Zhao, Kuang, Yuan, Qi, & Fang, 2018), or shape memory of one of the layers(Cui, Adams, & Zhu, 2018), can also be used to induce bending. In the rest of this paper, we will be concerned exclusively with such bilayers in which a large difference in mechanical properties between layers induces shape changes.

Some of the recent fundamental research on bilayer mechanics was conducted by bonding together layers while holding one or both layers prestretched (Caruso, Cvetkovic, Lucantonio, Noselli, & DeSimone, 2018; Z. Chen et al., 2011; DeSimone, 2018; Robertson et al., 2015). Upon bonding the layers and then releasing, the composite specimen adopted a bent configuration. When the prestretched layer was under equi-biaxial stretch, the composite bilayers bent into bistable

cylinders or spherical bowls depending on thickness and width of the specimen as well as the applied prestretch(Caruso et al., 2018). Unlike a bimetallic strip where the strain mismatch is inherently isotropic, prestretching allows investigations of anisotropic strain states. In (Caruso et al., 2018) it is found that the curvatures of the system bifurcate upon reducing bilayer thickness, and such bifurcation separates two scaling regimes for the energy of the system. In a related work, upon searching for isometries from a reference surface of the bilayer, DeSimone nicely modeled the effects of bonding a uniaxially prestretched rubber layer to an unstretched rubber layer(DeSimone, 2018). This is done in [27] using a novel finite dimensional constrained energy minimization problem. Upon unloading, the composite bilayer bent into an mono-stable roll, with the prestretched layer on the inside (DeSimone, 2018). In contrast, Chen et al. bonded rubber layers that were both prestretched, but along perpendicular directions(Z. Chen et al., 2012). Upon releasing, the composite bilayers bent into saddle shapes or bistable cylinders depending on thickness and width of the specimens(Z. Chen et al., 2012). Such bonding with prestretch also allows investigations of how specimen geometry couples with anisotropy in prestretch, e.g. a rectangular strip where the long direction is at an angle with respect to the prestretch direction forms helical shape(DeSimone, 2018).

This article focuses on shape changes occurring due to a *deformation-induced strain mismatch*. Specifically, we examine shape changes of a rubber-plastic bilayer which has been uniaxially stretched, and then released, as illustrated in Figure 27B. First consider the free-standing layers of the rubber and the plastic, Figure 27A. Upon stretch-release, the rubber layer recovers its original configuration, whereas the plastic maintains its stretched shape. Now consider a bilayer in which these two layers are bonded to each other, both under stress-free conditions. Upon

stretching, an elastic strain mismatch is created. Thus, upon releasing, the bilayer is expected to bend (Figure 27B).

Real rubbery materials are not perfectly elastic and may undergo modest inelastic deformations. Similarly, real plastics do not maintain their deformed shape perfectly, but instead show modest shape recovery after deformation. Nevertheless, provided that the degree of inelastic deformation of the two layers is unequal, bending is expected. Excellent examples of such bending are shown by Wisinger et. al(Wisinger et al., 2019). Incidentally note that Figure 27, which is a 2-dimensional illustration, only shows simple arch shapes, whereas Wisinger et. al showed arches as well as helical shapes, depending on the magnitude of elastic strain mismatch. This paper will show an even wider range of complexity including saddle shapes such as mentioned in the previous paragraph for fully elastic bilayers under biaxial strain mismatch. Further, we will show that even the direction and sign of the curvature depend on the applied stretch, a complexity not reflected in Figure 27.

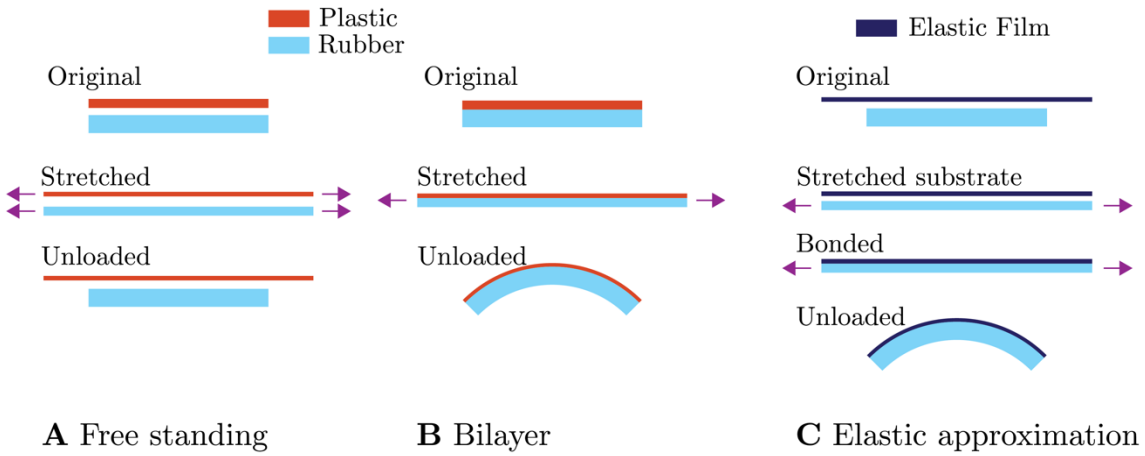

Figure 27: Schematic of rubber and plastic behavior when stretched and unloaded. (A) Both the layers are free-standing. (B) The layers are bonded, forcing equal deformation at the interface. (C) Schematic of shape change that occurs when a stretched rubber substrate is bonded to an unstretched elastic film, and then released.

The *deformation-induced strain mismatch* of Figure 27B is a powerful means to realize shape-morphing materials. Changes in shape can be induced by simply stretching the material to the desired extent, which is far simpler than stimuli such as light or heat(Robertson et al., 2015; Wisinger et al., 2019). Irreversible deformation is common amongst a variety of materials including metals, polymers, or even amorphous particulate materials, and hence this approach can be applied to a variety of systems. Indeed, an excellent example is of helically-coiled synthetic muscle fibers which were created by simply stretching an elastic-plastic composite(Kanik et al., 2019).

Despite the potential power of elastic-plastic composites to realize complex shape changes, their mechanics is poorly understood, even for the case of bilayers. At first glance, it is tempting to interpret such bending as being analogous to the shape change of an elastic-elastic bilayer with a strain mismatch. This analogy is illustrated in Figure 27C: the stretched state of the elastic-plastic bilayer is regarded as equivalent to bonding a stress-free elastic layer to a rubber layer pre-stretched to the same dimensions(Wisinger et al., 2019). As per this analogy, the ***only*** role of inelastic deformation is to create a strain mismatch when the sample is stretched; the mechanics after release presumes that both materials behave elastically. Indeed, this "elastic-after-release" is exactly the modeling approach followed by Wisinger et.al(Wisinger et al., 2019). Yet, although the analogy of Figure 27C is useful, inelastic deformation may have several consequences beyond merely creating the strain mismatch upon stretching.

First, upon releasing, the plastic layer experiences compression, and if the compressive stress exceeds the yield stress of the plastic, it will deform inelastically. Figure 27B presumes that the plastic remains at its stretched dimensions upon release, but if it yields in compression, the

degree of bending will reduce. This is well-recognized in bimetallic strips in which, if the yield stress of one of the layers is exceeded, the curvature becomes much less sensitive to temperature changes(Finot & Suresh, 1996; Shen & Suresh, 1995). An example will be shown in this paper.

Second, if the elastic layer is relatively soft and thick, the plastic face of the bilayer may buckle in compression and develop wrinkles at sufficiently large strain mismatch (Y. Hu, Hiltner, & Baer, 2004; Srinivasan, Subbarayan, & Siegmund, 2012; Takei et al., 2016; Yang et al., 2017). In fact, wrinkles may develop even for a purely elastic bilayer in the geometry of Figure 27C(Z. Y. Huang, Hong, & Suo, 2005; Jin, Takei, & Hutchinson, 2015; Lin et al., 2020; Ma et al., 2016; Song et al., 2008; Takei, Jin, Hutchinson, & Fujita, 2014; Yin, Yague, Eggenspieler, Gleason, & Boyce, 2012), but in elastic-plastic composites, the wrinkling is coupled with yielding, and wrinkles can form before or after yielding(Yang et al., 2017). This paper will show that yielding occurs before wrinkling, and wrinkles persist even when the plastic layer is debonded from the rubber, which indicates the formation of plastic hinges. The effect of wrinkles on shape changes have not been explored in this context before.

Third, in fully-elastic bilayers, bistable shapes are encountered commonly. Bistability can be desirable, e.g. Venus flytrap relies on the snap-through of a double curvature surface(Forterre, Skotheim, Dumais, & Mahadevan, 2005) or snapping mechanical wires(Charlot, Sun, Yamashita, Fujita, & Toshiyoshi, 2008) and many others reviewed here(Zhang et al., 2019). Similarly, a biaxial elastic strain mismatch can induce bistability such that the bilayer can bend in one of two possible directions (Caruso et al., 2018; DeSimone, 2018). However, bistability need not be desirable and considerable research been done on guiding the direction along which curvature develops(Cendula, Kiravittaya, Monch, Schumann, & Schmidt, 2011; Cendula, Malachias, Deneke, Kiravittaya, & Schmidt, 2014; Cui et al., 2018). This article shows that rubber-plastic

bilayers tend to form single stable shapes. Thus, no external control other than the magnitude of applied stretch is required to control the final morphology.

Finally, even during the stretching process itself, inelastic deformation may introduce complexities beyond merely introducing a strain mismatch. Free-standing plastic layers are prone to necking behavior in tension, and free-standing polymeric plastic layers may also show stable neck propagation(Argon, 2013a). Bonding an elastic layer to a plastic reduces the tendency for necking, nevertheless, if the elastic layer is sufficiently thin or soft, an elastic-plastic bilayer may show necking and/or stable neck propagation(Ben Bettaieb & Abed-Meraim, 2017; Holland, Li, Feng, & Kuhl, 2017; T. Li & Suo, 2006; N. Lu, X. Wang, Z. Suo, & J. Vlassak, 2007; R. G. Ramachandran et al., 2018; Rahul G. Ramachandran et al., 2020). Thus, due to non-homogeneous stretching, in-plane strain gradients may develop during the stretching phase, which would then affect subsequent shape changes. An example of this will also be shown in this paper.

In summary, the above arguments suggest that an "elastic-after-release" framework is tenable only if (1) the elastic-plastic bilayer deforms homogeneously during stretching, (2) compressive stress developed in the plastic layer after release is lower than its yield stress and (3) surface instabilities like wrinkles do not appear. The second and third condition suggests that elastic strain mismatch must depend, even qualitatively, on the applied stretch. Upon releasing from a low stretch, the rubber imposes only a modest compressive stress on the plastic layer, and hence the plastic may not yield. However, upon releasing after a large applied stretch, the rubber must impose a correspondingly large stress on the plastic, and yielding becomes likely. Similarly, a critical strain mismatch is required for wrinkling to occur. Indeed, this paper confirms a significant dependence of shape changes on the applied stretch.

This chapter is organized as follows. Section 5.2 describes the materials and methods. Section 5.3.1 describes experimental observations of rubber-plastic bilayers subjected to stretch and release. We show that even the qualitative nature of shape changes in such composites depend on the applied strain. Rectangular specimens released from a small stretch bend as expected into arch or roll shapes with a single dominant curvature. Specimens released from a large stretch also show a single dominant curvature, but with the opposite sign and direction. Intermediate stretches give both curvatures, i.e., saddle shapes. Unlike elastic-elastic composites, all these shapes appear to be monostable. Section 5.3.4 and 5.3.5 show how the sample geometry affects the results, in particular that narrow specimens are susceptible to twisting deformations. Finally, Section 5.3.7 shows non-homogeneous bending that occurs because the plastic layer is prone to necking. An analytical model is described in Section 5.4 which shows how modification in elastic strain mismatch due to inelastic deformation and wrinkling during release can lead to flip in sign and direction of the curvature with increasing stretch.

Table 1 List of Symbols Used

H^r, H^p	Thickness of rubber layer and plastic layer in the undeformed configuration
h^r, h^p	Thickness of rubber layer and plastic layer in the deformed configuration
λ_x, λ_y	Stretch along the X and Y – direction away from the grips
λ_{max}	Highest value of λ_x imposed during the stretching
σ	Cauchy stress
λ_{per}^p, λ_{per}^r, λ_{per}	Permanent stretch in the plastic, rubber, and bilayer after unloading from a stretch of λ_{max}
$\lambda_{x,mis}$, $\lambda_{y,mis}$	Stretch mismatch in the X and Y – directions estimated from free-standing rubber and plastic layers
$\bar{\lambda}_{x,mis}$, $\bar{\lambda}_{y,mis}$	Effective stretch mismatch in the X and Y – directions estimated from the bilayer experiments
κ_y	Curvature in the XZ plane with normal along Y – direction
κ_x	Curvature in the YZ plane with normal along X – direction
ψ^r	Strain energy density function of the rubber
V^r	Volume of rubber layer
U^r	Total strain energy in the rubber layer

5.2 Methods

5.2.1 Experimental

Sheets of natural rubber (McMaster Carr) of undeformed thickness, $H^r = 250\ \mu m$, 500 μm and 750 μm were used as the elastomer layer. Sheets of linear low-density polyethylene (LLDPE) of $H^p = 50\ \mu m$ thickness was used as the plastic. Rubber-plastic bilayers of different thickness ratios were prepared by bonding the LLDPE sheets to the rubber sheets. The bond was made by passing the two layers together through heated mechanical rollers to eliminate air pockets and then heating to 150^oC and holding for 10 mins to strengthen the bond. Rectangular specimens of 22 mm length and various width values of 2 mm, 4 mm, 8 mm, 12 mm, and 16 mm where then cut out using punches. The test specimens were stretched and unloaded on an MTS® tensile testing machine at a clamp speed of 5 mm/min. Either ink marks or small particles were applied on the rubber side of the samples, the tests were video-recorded, and the marker displacements were calculated by Digital Image Correlation (DIC) analysis using the Blender software. The true stretch along the X-direction (λ_x) was then calculated from the marker displacements as described in our previous publication(R. G. Ramachandran et al., 2018). Only regions of the samples away from the grips were used in this analysis. These true values of λ_x measured directly from the images were typically somewhat smaller than nominal values expected from the motion of the clamps. This may be due to slipping of the specimen at the grips at large stretches, or slightly non-homogeneous deformation near the sample ends. We will only use true values throughout this paper. The highest value of λ_x for any given specimen, designated λ_{max}, is used as a measure of imposed stretch.

To study the effect of applied stretch on the final morphology, each sample was stretched to the desired extent, corresponding to λ_{max} values ranging from 1.4 to 3.8, and then unloaded. The end-sections of the samples that had been clamped in the tensile testing device were then cut off with a razor blade, thus leaving only the sections that had experienced stretching. These final equilibrium shapes were photographed.

The stress-free state of the layers in the bilayer after deformation was studied by forcing delamination of the layers. Partial or full delamination happened naturally after several days' storage. Partially delaminated samples were then exposed to solvent heptane to achieve complete delamination.

The experiments of Section 5.3.7, on samples that show necking in tension, used a different pair of materials that will be described in that section.

5.2.2 Material behavior

Prior to measuring the behavior of the free-standing monolayers, LLDPE and rubber samples were first heated identically as the bilayers to erase any possible processing effects from the film manufacturing. Figure 28A and 2C show the Cauchy stress (σ) vs true stretch in the X-direction (λ_x) response of LLDPE and the rubber films after stretching to three different values of stretch. The Cauchy stress was computed as $\sigma = \frac{F}{A_o}\lambda_x$ where F is the reaction force measured and A_o is the original cross section area of the specimens.

In all cases, the force increased during stretching, and then decreased back to zero during release. The stretch, λ_x at which the force reverted to zero during release is dubbed the "permanent

stretch" (λ_{per}) and is a measure of inelastic deformation. The LLDPE underwent significant permanent deformation after stretching, e.g., after stretching to an λ_{max} of 3.8 and then releasing, the sample recoiled to a permanent stretch of λ_{per}^{p} =2.98. The permanent stretch in plastic (λ_{per}^{p}) obtained from three experiments in Figure 28A is plotted against the λ_{max} in Figure 28B, along with a straight line fit:

$$\lambda_{per}^{p} = 0.84\lambda_{max} - 0.25 \tag{5.1}$$

Eqn. 5.1 does not have physical significance but will only be used to interpolate between the experimentally recorded λ_{max} values in the range $1.8 < \lambda_{max} < 3.8$.

In contrast to the plastic, the rubber is much more elastic, e.g., after releasing from a λ_{max} of 3.3, the rubber recoils to a permanent stretch of $\lambda_{per}^{r} \approx 1.08$, indicating only a small permanent deformation. It is this difference between the degree of elastic recoil that causes the strain mismatch, which in turn induces shape changes.

Since λ_{per}^{r} is close to 1 (i.e., the rubber recovers almost completely), the stretch mismatch between the free-standing layers is taken as equal to the permanent stretch in the plastic layer ($\lambda_{x,mis} = \lambda_{per}^{p}$). It is this mismatch stretch that induces severe bending. Note that if the layers follow uniaxial deformation kinematics with $\lambda_y = 1/\sqrt{\lambda_x}$, there must be a strain mismatch in the Y-direction with magnitude $\lambda_{y,mis} = 1/\sqrt{\lambda_{x,mis}} = 1/\sqrt{\lambda_{per}^{p}}$. The two mismatch stretches are shown in Figure 37A, to be discussed later.

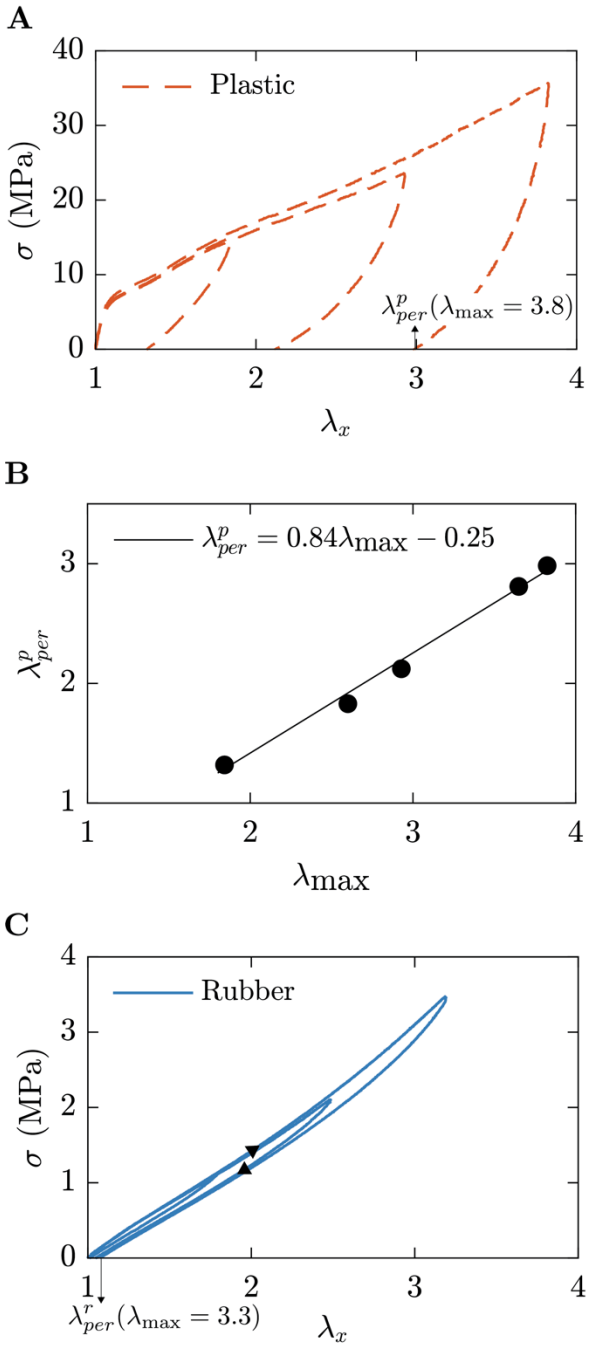

Figure 28: (A) Cauchy stress (σ) vs true stretch in the X-direction (λ_x) for LLDPE film. The permanent stretch (λ^p_{per}) is marked for the curve with $\lambda_{max} = 3.8$ (B) λ^p_{per} for the three curves in Figure 28A vs corresponding λ_{max} . (C) σ vs λ_x for natural rubber.

Incidentally, it is noteworthy that that for the plastic, a plot of force vs stretch (or equivalently engineering stress, F/A_o vs stretch, dashed curve shown in ESI Figure S2) does not show a peak; such a peak would indicate necking. Moreover, quantitative video analysis confirms that LLDPE stretches uniformly. This is in contrast to the necking seen in many semi-crystalline polymers. The engineering stress vs stretch of such a necking material is also presented in ESI Figure S2 (purple curve). Section 5.3.7 will show an example of such a necking plastic.

5.3 Results

The schematics of stretch-release and subsequent morphology change is shown in Figure 29A. The initial sample dimensions are denoted L, W, and H along the X, Y, and Z directions respectively. When a stretch λ_x is applied, the length increases but the width, w and thickness, h in the stretched configuration both reduce due to the Poisson effect.

The final morphology after unloading can have two curvatures. The curvature about the Y-axis (i.e., in the XZ plane) is marked as κ_y, whereas the curvature about the X-axis (i.e., in the YZ plane) is denoted as κ_x. In some cases, one of these curvatures may be nearly zero.

5.3.1 Roll to half-tube transition with increasing λ_{max}

As mentioned in Section 5.2.2, the strain mismatch between the rubber and plastic layers increases with increasing λ_{max}. Accordingly, the shapes after stretch-release also depend on the λ_{max}, as shown in Figure 29B-I. These figures all correspond to rectangular bilayer specimens of initial dimensions $L = 18$ mm and $W = 8$ mm, released after various applied stretches. The

rubber and plastic had a thickness of $H^r = 750\ \mu m$ and $H^p = 50\ \mu m$ respectively. Only the applied stretch was varied. At the lowest λ_{max} value of 1.4, the sample bends into an arch shape with the plastic layer being on the outside of the arch, i.e., $\kappa_y > 0$ and κ_x is nearly zero (in fact, slightly negative). With increasing λ_{max}, κ_y increases significantly as the sample forms a roll shape, but κ_x remains near zero. Once the $\lambda_{max} \geq 2.9$ (Figure 29F), the samples adopt a saddle-shape, i.e., dual curvature with $\kappa_y > 0$ and $\kappa_x < 0$. It is noteworthy that κ_y now reduces with increasing stretch. With further increase in λ_{max}, κ_y continues reducing whereas κ_x becomes increasingly negative, i.e., the samples gradually revert to having a mono-curvature, but with a sign and direction that both are flipped with respect to the original arch. The shape of Figure 29J is dubbed a "half-tube" in this paper. A final interesting feature is that for $\lambda_{max} \geq 2.8$, wrinkles appear. These wrinkles are always oriented parallel to the width direction and are always on the plastic face of the specimens.

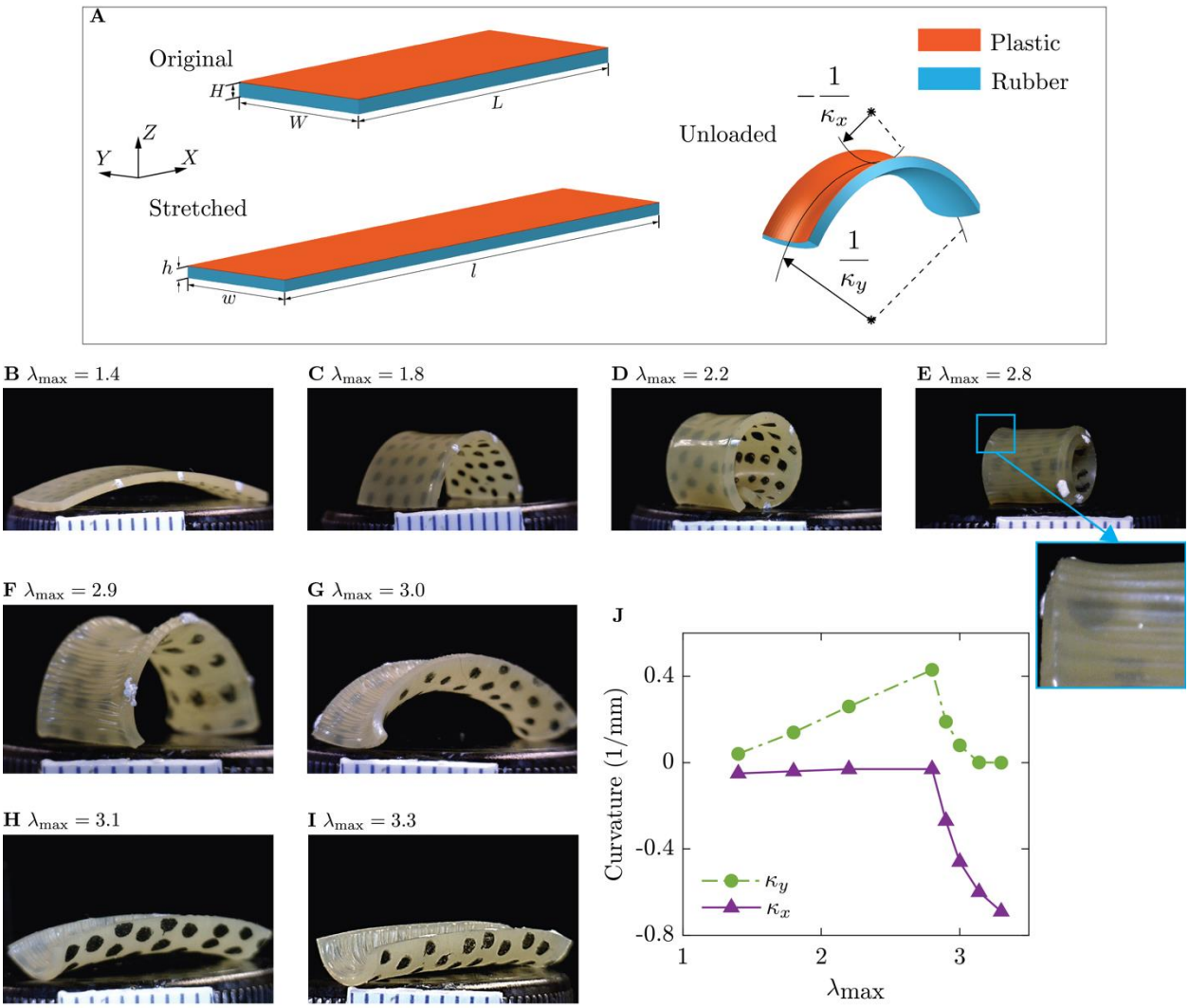

Figure 29: (A) Schematic of a rectangular rubber-plastic bilayer specimen subjected to stretch of λ_{max} along X-direction. In general, the final morphology after unloading (right image) has two curvatures as indicated. The curvatures about the X and Y axes are denoted κ_x and κ_y where $\kappa_x < 0$ and $\kappa_y > 0$. The corresponding radii of curvature, $-\frac{1}{\kappa_x}$ and $\frac{1}{\kappa_y}$ are marked, where the * points indicate the centers around which the curvature develops. (B-I) Pictures of final shape for specimens as λ_{max} increases from 1.4 to 3.3. Spacing between the scalebar marking is 1 mm. Note the change in the direction and sign of the curvature between (E) and (H). Also note the wrinkles on the plastic face for E-I (J) Curvatures κ_x and κ_y vs λ_{max}.

The curvature values, κ_x and κ_y quantified by image analysis (see Figure S1 in supplementary material) for the specimens of Figure 29B-I are shown in Figure 29J. This figure clearly shows the non-monotonic nature of κ_y. Further, the maximum in κ_y also roughly coincides with the stretch at which κ_x first deviates significantly from zero.

5.3.2 Inelasticity in Compression and Wrinkling of Film

A key question raised in the Introduction is: to what extent is the deformation inelastic during the release process? We address this question by debonding the layers after stretch release and letting them revert to their stress-free shapes. These debonded layers can then be compared with free-standing layers stretched to the same extent. If the permanent deformations of these debonded layers agree with those expected for the free-standing layers (permanent stretch of the plastic layer should be λ_{per}^{p} from Figure 2B, and permanent stretch of the rubber layer should be nearly 1), an elastic-upon-release view would be justified. Any deviation would indicate inelastic deformation during the release.

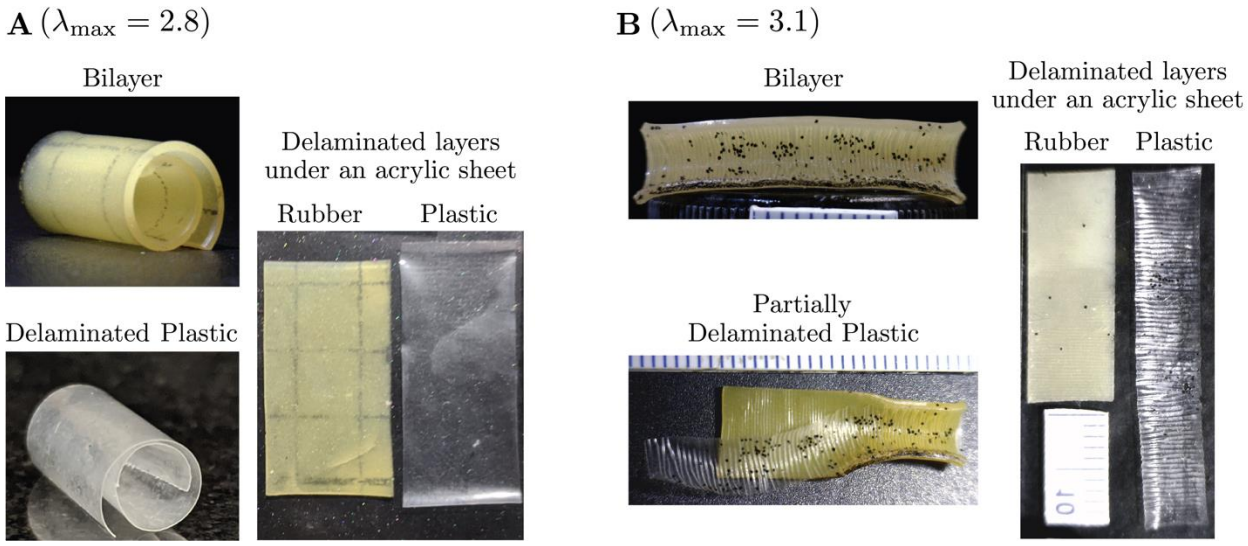

Figure 30: (A) Roll shape is formed after stretching and unloading a rubber-plastic bilayer to $\lambda_{max} = 2.8$. The film keeps its shape when it is delaminated from the rubber substrate. (B) Half-tube shape is formed after unloading from $\lambda_{max} = 3.1$. Partially delaminated plastic show permanent wrinkles. Thin white lines are apparent on the rubber indicating some local damage. Spacing between the scalebar marking is 1 mm.

Two examples are shown in Figure 30. Figure 30A corresponds to an 18 mm × 12 mm sample ($H^r = 750\ \mu m$) with $\lambda_{max} = 2.8$, for which the shape prior to debonding was a roll with $\kappa_y > 0$ and $\kappa_x \approx 0$. The shape is not a perfect cylinder but shows a small gradient in curvature. Upon debonding, the plastic film remained in the form of a roll (Figure 30A) with little apparent change as compared to the fully bonded bilayer. Meanwhile the rubber recovered its undeformed shape almost completely. The roll-shaped plastic layer was then gently unrolled, placed alongside the corresponding delaminated rubber, and held flat by placing it under a thin acrylic sheet. This image of the two layers side-by-side is also included in Figure 30A. It is immediately apparent that the debonded plastic layer is only about 10% longer than the rubber layer (i.e., its permanent stretch is only 1.1), indicating only a small elastic mismatch. Moreover, substituting $\lambda_{max} = 2.8$ into Eqn. 5.1 gives $\lambda_{per}^{p} = 2.1$, i.e., the free-standing plastic, released from the same stretch, would end up

almost twice as long as the debonded plastic from Figure 30A. This is clear evidence that the rubber was able to inelastically compress the plastic layer significantly, almost back to the stress-free configuration of the rubber itself.

Figure 30B corresponds to a sample with applied $\lambda_{max} = 3.1$, where the shape prior to release (Figure 29I) is nearly a half-tube with $\kappa_x < 0$ and and $\kappa_y = 0.04\ \text{mm}^{-1}$ with wrinkles on the plastic face. The λ_{per} of the half-tube was measured to be nearly 1, i.e., the rubber nearly recovered its undeformed length even prior to debonding. The plastic layer accommodated this by wrinkling and/or in-plane yielding. Upon debonding, the plastic layer remained permanently wrinkled, whereas faint lines are apparent in the rubber that indicate some local damage at the wrinkle locations. An image of the two delaminated layers flattened by weighing down with an acrylic sheet is also included in Figure 30B. Unlike Figure 30A, there is now a large mismatch in length and width of the two debonded layers. The end-to-end length of the flattened delaminated plastic in Figure 30B is found to be 1.5 times of the delaminated rubber. In fact, the wrinkles on the delaminated plastic are not perfectly flattened by the acrylic sheet, and hence its true contour length is somewhat larger. Nevertheless, the contour length is significantly less than would be expected for free- standing plastic (λ_{per}^{p}=2.35, obtained by substituting $\lambda_{max} = 3.1$ into Eqn. 5.1). Thus, the plastic layer in Figure 30B deformed permanently in both in-plane compression and wrinkling.

The central conclusions from Figure 30 are twofold, both of which testify to the importance of yielding during release. First, at modest values of λ_{max} (Figure 30A) the inelastic deformation of the plastic layer has a through-thickness gradient that is roughly uniform across the entire area of the sample. This causes it to stay bent even after debonding. The actual values of the permanent deformations also show a large degree of inelastic in-plane compression of the plastic during the

release step. Second, at large values of λ_{max} (Figure 30B), the wrinkles indicate that the inelastic deformation of the plastic has highly localized through-thickness gradients that are periodic along the X-direction. Such highly-localized inelastic bending is often called plastic hinge formation(Takei et al., 2016). The formation of wrinkles allowed the plastic to maintain a large contour length, while conforming to the small length of the rubber at the interface.

5.3.3 Kinematics During Release

While examination of the films after debonding gives insights into the final state after complete unloading, an examination of the videos during stretch and release offers further insights. The experiment with λ_{max}= 3.1 (L =18 mm, W =8 mm, $H^r = 750\ \mu m$) shown in Figure 30B is considered again since it undergoes inelastic compression as well as inelastic wrinkling. For this experiment, two video cameras were used: a view normal to the Z-direction was used to quantify stretches, and a view at a shallow angle with respect to the X-Y plane was used to image wrinkle development. This latter video, entitled *VideoUnloading.mp4*, is available as ESI, and the results are shown in Figure 31.

Figure 31A shows the evolution of reaction force with test time. Figure 31B and C show the λ_x and λ_y calculated from the displacements of the markers applied on the specimen. The orange x-marks in the three graphs correspond to the three images in Figure 31D-F. These images are portions of the sample at three times close to the instant when wrinkles are first evident in the video.

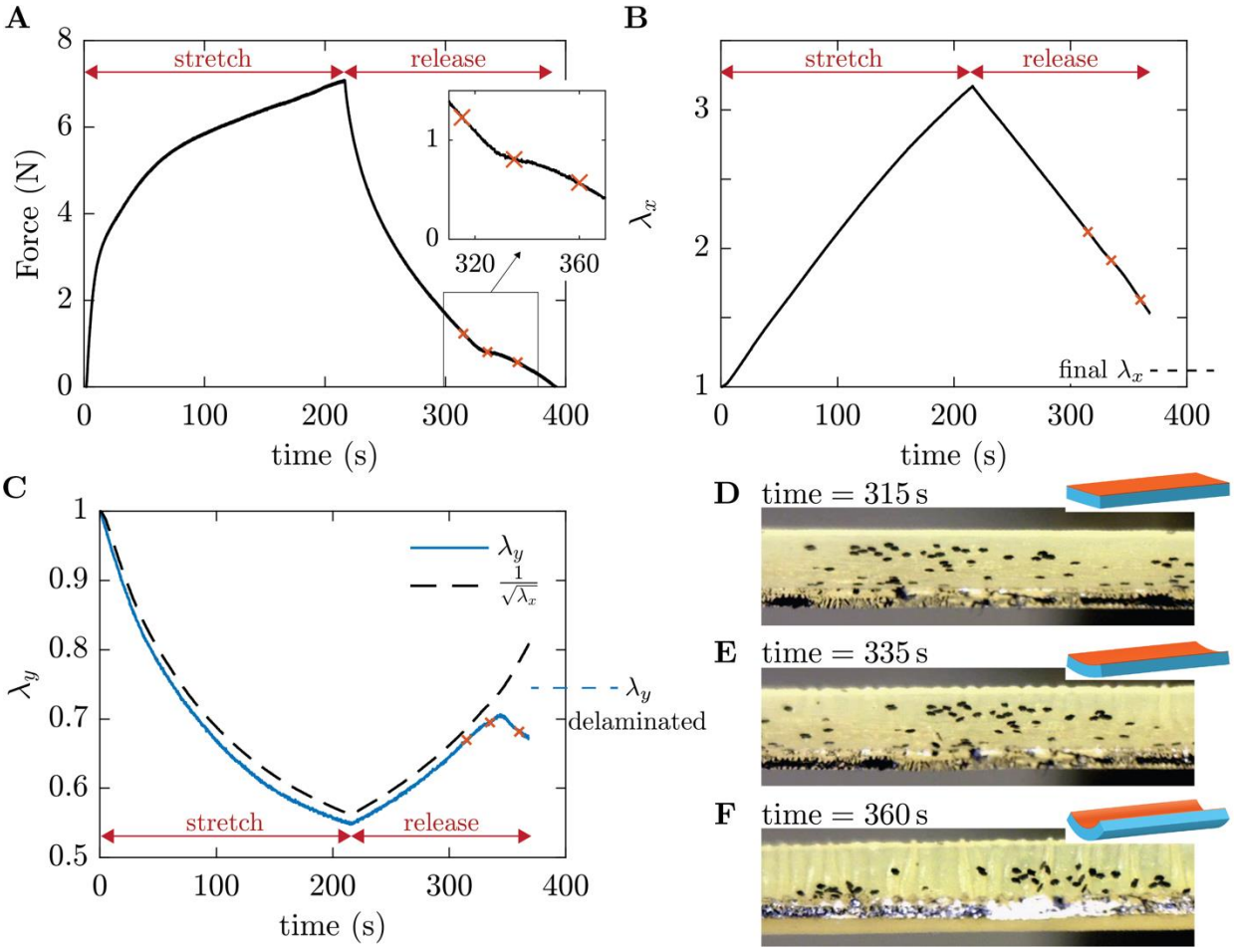

Figure 31: Kinematics during loading and unloading of a 18mm × 8mm sample with $\lambda_{max} = 3.2$. (A) Reaction force with test time. (B) Stretch in the X-direction (λ_x) vs test time. Final λ_x from the fully-unloaded sample is shown as horizontal dashed line. (C) Stretch in the Y-direction (λ_y) vs test time. Final λ_y estimated from the width of the delaminated plastic layer is shown as dashed line. (D-F) Pictures of specimen at test times marked by orange x in A-C taken at an oblique angle (Inset show schematic of sample shape). Wrinkles appear around time = 335 s. Specimen is strongly bent (i.e., $\kappa_x \neq 0$) in F.

During the stretching phase, the force (Figure 31A) and λ_x (Figure 31B) both increase monotonically, whereas λ_y reduces (Figure 31C). The black dashed curve in Figure 31C corresponds to uniaxial kinematics, $\lambda_y = 1/\sqrt{\lambda_x}$, and is in excellent agreement with the measured λ_y.

The release step has two distinct phases. Up to a time of 335 s, the force reduces, and λ_x and λ_y approach 1. The measured λ_y remains consistent with uniaxial kinematics. Beyond 335 s (second orange x mark), several changes appear: there is an abrupt change in slope of the force vs time curve; the plastic face of the sample develops wrinkles (Figure 31E); λ_y becomes smaller than expected from uniaxial kinematics; and the sample bends around the X-direction (Figure 31F, but clearer in the corresponding video file *VideoUnloading.mp4)*. Due to this last effect, λ_y can no longer be estimated reliably from the DIC analysis of the video. These changes appear only in samples that wrinkle. Samples that do not show wrinkles (not shown) obey uniaxial kinematics throughout the release process and do not show any abrupt change in slope of the force-time curve.

The λ_x measured from the contour length of fully-unloaded sample is shown as a horizontal dashed line in Figure 31B. Further, the width of the plastic layer after delamination allows an estimate of the final value of λ_y in the fully-unloaded sample, and that value is shown as a dashed horizontal line in Figure 31C. This final value of λ_y is far below that expected from uniaxial kinematics.

The central insight from Figure 31 is that wrinkles play a major role during the release step. The rubber seeks to reduce in length and increase in width during release, and it seeks to impose the same kinematics on the plastic. Prior to wrinkling, as the plastic layer is forced to reduce in length (λ_x decreases), it also increases in width (λ_y increases) consistent with uniaxial kinematics. Once wrinkles appear however, the plastic accommodates the x-direction compression by wrinkling, and the y-direction tension by bending, i.e., by developing κ_x. Accordingly, as judged from macroscopic shape changes, the width and length of the plastic layer appear to become decoupled: the length reduces continuously with time, whereas the width remains almost constant.

Yielding of the plastic, either with or without wrinkling, implies that the strain mismatch calculated from the permanent deformation of the free-standing layers does not determine the final shape. Accordingly, we now define "effective" strain mismatches $\bar{\lambda}_{x,mis}$ and $\bar{\lambda}_{y,mis}$, which are estimated from the permanent deformation of the delaminated layers. The horizontal dashed lines in Figure 31B and Figure 31C correspond to $\bar{\lambda}_{x,mis} \approx 1.1,$ and $\bar{\lambda}_{y,mis} \approx 0.74$ respectively for this sample.

The same digital correlation analysis was repeated for all the samples and the effective strain mismatches were measured. They are shown against λ_{max} in Figure 37C. The difference between Figure 37A vs C quantifies the three effects of inelastic deformation. First, at all stretch values, $\bar{\lambda}_{x,mis} \ll \lambda_{x,mis}$ due to yielding during release. Second, for $\lambda_{max} \geq 2.8$ (exactly corresponding to the stretches at which wrinkles appear in Figure 29), $\bar{\lambda}_{x,mis}$ reduces as λ_{max} increases. Such non-monotonic behavior of mismatch stretch could not have been anticipated from the behavior of the free-standing films at all. Finally, samples that wrinkle also deviate from uniaxial kinematics. This is shown by the small green circles which are the calculated values of $1/\sqrt{\bar{\lambda}_{x,mis}}$. The measured $\bar{\lambda}_{y,mis}$ remain close $1/\sqrt{\bar{\lambda}_{x,mis}}$ up to $\lambda_{max} < 2.8$ but are significantly smaller once wrinkles appear.

5.3.4 Effect of Specimen Width

The tests shown in Section 5.3.1 were repeated for specimens of width 2 mm, 4 mm, and 16 mm. In all cases, the undeformed length of the sample was kept at 18 mm and the rubber thickness was kept at 750 μm, same as in the previous section. The final shapes after applying λ_{max} of 1.8, 2.8, and 3.3 are shown in Figure 32 . For most samples, two images are shown, taken

along the Y and X directions respectively to clearly indicate the two curvatures. The images in the in the 8 mm row are the same samples as in Figure 29. The background colors of the table are chosen to distinguish between the various shapes: green for arch/roll shapes ($\kappa_y > 0$ and $\kappa_x \approx 0$), orange for saddles ($\kappa_y > 0$ and $\kappa_x < 0$), blue for tubular shapes ($\kappa_y \approx 0$ and $\kappa_x < 0$), and pink for helical ones.

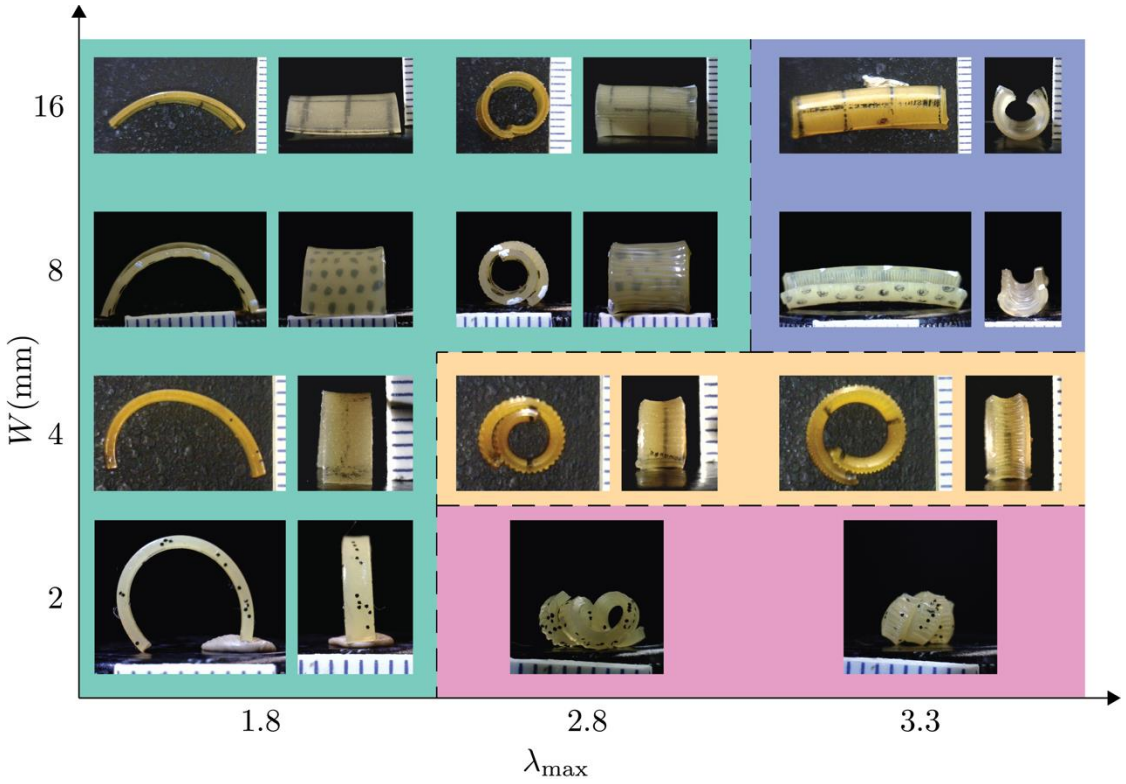

Figure 32: The final shapes formed after stretching and unloading 2 mm, 4 mm, 8 mm, and 16 mm wide rubber-plastic bilayer specimens when λ_{max} is 1.8, 2.8, and 3.2. Two images, taken from orthoganal directions are shown for most samples. The 8 mm wide samples are the same as those discussed in Section 5.3.1. For the 2 mm wide sample, complex helical shapes appeared for large λ_{max} values. Spacing between the scalebar marking is 1 mm.

The left column in Figure 32 shows that at all widths, arches/rolls form at the smallest stretch examined. Width affects both, the value of λ_{max} up to which arches are stable, and which shape appears at high stretch. As stretch increases, the narrowest samples transition into helices which will be discussed in Section 5.3.6. Wider samples first transition into saddles and then into half-tubes; increasing W raises the stretch needed for both transitions.

While Figure 32 shows a transition from rolls to tubes directly at large W, Figure 29 has already shown that for $W = 8$ mm, saddle shapes appear in between. Similar intermediate saddle shapes may exist at $W = 18$ mm as well. Further, at $W = 4$ mm, the magnitude of κ_y decreases and that of κ_x increases as λ_x increases. I.e., even though unambiguous tubular shapes ($\kappa_y \approx 0$) are not evident up to the stretch examined, the trend is consistent with a saddle to tube transition

5.3.5 Effect of Rubber Thickness

All the data thus far used a single rubber thickness of 750 μm. Figure 33 shows the effect of reducing the rubber thickness using samples of the same lateral dimensions ($W = 8$ mm x $L = 18$ mm) as in Figure 29. Reducing H^r has three distinct effects. First, the magnitude of curvature increases with decreasing rubber thickness. For example, the first column of Figure 33 shows that for $\lambda_{max} = 1.8$, κ_y increases with decreasing rubber thickness. Second, when the rubber thickness is 500 or 250 μm, neither a saddle nor a tube shape is formed regardless of the λ_{max}. Instead, the final shapes are arch/roll when the λ_{max} is small, and more complex helical shapes when $\lambda_{max} = 3.3$. Although at first glance, these look distinctly different from the helices in Figure 32, in fact, they show the same twisting deformations during release (see Section 5.3.6). Finally, wrinkles

require significantly higher stretches to appear: the λ_{max} needed for wrinkles increases from 2.8 at $H^r = 750\ \mu m$ to 3.3 for $H^r = 500\ \mu m$, whereas the bilayers with $H^r = 250\ \mu m$ do not show wrinkles at even the highest stretch examined.

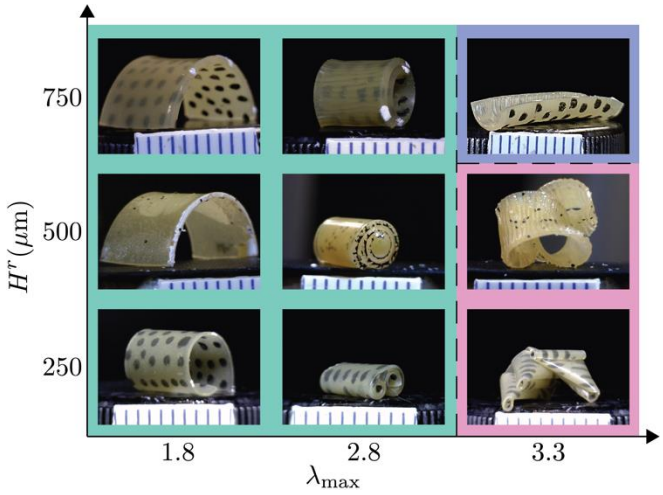

Figure 33: The final shapes formed from bilayers with rubber thickness of 250 μm, 500 μm, 750 μm with λ_{max} of 1.8, 2.8 and 3.3. The samples with 250 μm and 500 μm thick rubber formed complex helical shapes when $\lambda_{max} = 3.3$. Spacing between the scalebar marking is 1 mm.

5.3.6 Helical Twisting

Apart from rolls, tubes, and saddles, rubber-plastic bilayers can form complex helical shapes. Helical shapes were also noted by Wisinger et. al(Wisinger et al., 2019). Kanik et. al(Kanik et al., 2019) also created helical springs in an elastic-plastic multilayer system, although the cross sections of their bilayers were not precisely rectangular. Figure 32 and Figure 33 show that twisting deformations are favored by narrow samples, thin samples, and by large stretch values prior to release.

Insight into twisting deformations can be obtained from videos recorded during the unloading process (*Video1Twisting.mp4, Video2Twisting.mp4)*, and snapshots from these videos are shown in Figure 34. As the strain mismatch increases during release, the samples develop an internal stress that promotes bending around the Y direction; in an unconstrained sample, this would lead to $\kappa_y > 0$. However, during the release process, the sample is constrained by the grips, i.e., by a global tensile load. It appears therefore that the large out-of-plane twisting deformations permit bending with a $\kappa_y > 0$, even though the ends remain constrained. As the applied stretch reduces, the global tensile load reduces, thus allowing well-formed helices.

It is interesting to note that in the two halves of the sample, the twist direction is opposite, because the grips not only impose an overall sample length, but also prohibit overall rotation. Thus, a vector drawn normal to a face of the sample cannot have net rotation around the x-direction. This induces the formation of mutually opposing twists, reconciled by a perversion near the middle of the sample(Gerbode et al., 2012; Goriely & Tabor, 1998; Pieranski, Baranska, & Skjeltorp, 2004; D. Wang, Thouless, Lu, & Barber, 2020). In fact, experiments on elastic ribbons that have an intrinsic curvature (not shown) exhibit the same behavior during unloading suggesting that to a first approximation, such twisting is not due to inelastic deformation.

Yet, we note that after full unloading, the twisting deformation is permanent, i.e., despite the fact that the grips no longer constrain the sample, the helices cannot be induced to form rolls even by gentle manipulation by hand. Thus, some degree of inelastic deformation must be present which stabilizes the helical shapes.

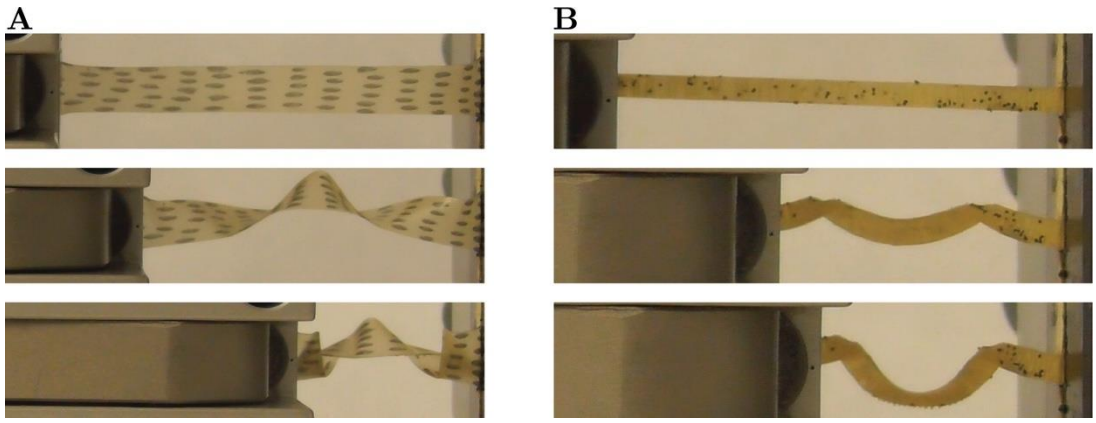

Figure 34: Formation of helical shapes during release of samples with (A) $18\ \text{mm} \times 8\ \text{mm} \times 250\ \mu\text{m}$ rubber and (B) $18\ \text{mm} \times 2\ \text{mm} \times 0.75\text{mm}$ rubber.

5.3.7 Non-Uniform Strain Mismatch

Section 5.2.2 mentioned that the LLDPE plastic did not show a peak in force displacement curve, and consistent with that, no necking was evident visually. However, many plastics, including many grades of polyethylene can undergo necking and subsequent drawing(I. M Ward, 1971a). Previously (R. G. Ramachandran et al., 2018; Rahul G. Ramachandran et al., 2020) we discussed how necking and drawing can be regulated by bonding a rubber layer to a plastic. When the rubber layer is relatively thin, the deformation of the rubber-plastic bilayer resembles that of the necking plastic, albeit with a decrease in the stretch in the neck. Necking creates a non-uniform strain distribution, and thereby non-uniform elastic strain mismatch between layers. All the discussion in this paper presumed that the strain mismatch was uniform everywhere; here we briefly consider a counter example.

For studying the effect of non-uniform strain mismatch, bilayers were prepared by bonding LLDPE sheets of thickness $H^p = 120\ \mu m$ to styrene-ethylene/propylene-styrene (SEPS) rubber sheets of 50 μm thickness as previously reported(R. G. Ramachandran et al., 2018). Then

10 mm × 5 mm wide rectangular specimens were cut, subjected to an applied stretch of 2.5, and released.

Unlike the plastic film used in the rest of this paper, the LLDPE used in this section shows strong necking under tension, and the onset of necking coincides with a peak in the force-displacement curve, shown in Figure S2 in supplementary material. An image of a bilayer during stretching is shown in Figure 35A. The non-homogeneous deformation is readily evident and quantified (see color map in Figure 35A) using our previous procedure(R. G. Ramachandran et al., 2018). Upon unloading, from a relatively small stretch, the sample took on the shape in Figure 35B, which resembles a hinge, i.e., substantially-flat regions connected by a sharply-bent region. If a larger displacement was imposed, the necked region showed localized twisting and resulted in the curled shape of Figure 35C.

Such localized necking may be exploited to realize strong localized bending, as common in origami design. The corresponding shape changes are however considerably complicated by the non-homogeneous strain distribution.

The central conclusion of this section therefore is that plastic materials are prone to necking under tension. Accordingly, when selecting materials for applications that exploit stretch-release behavior of elastic-plastic composites, it is crucial to know whether the free-standing plastic can neck or not.

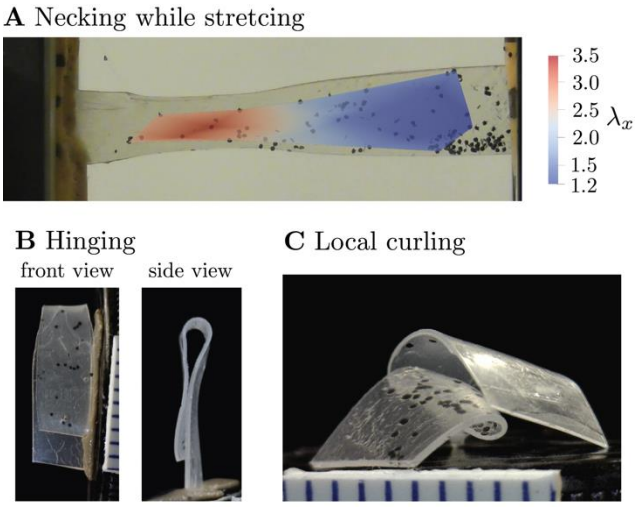

Figure 35: (A) SEPS-LLDPE rubber-plastic bilayer specimen undergoing necking under stretching. Color map shows local stretch along the stretching direction. (B) Non uniform deformation creating a hinge. (C) Non uniform deformation creating a localized curling. Spacing between the scalebar marking is 1 mm.

5.4 Discussion: Strain Dependent Arch to Half-Tube Transition

In a bilayer with an elastic strain mismatch, unidirectional bending, saddle formation, wrinkling, and helical twisting all offer competing pathways for energy minimization. In fully-elastic bilayers, uniaxial elastic strain mismatch induces stable unidirectional bending(DeSimone, 2018). Meanwhile, a equi-biaxial elastic strain mismatch creates dual curvature into bowl shapes at small mismatch, but bistable unidirectional bending into cylindrical shapes at large mismatch(Alben, Balakrisnan, & Smela, 2011). This paper shows that for elastic-plastic bilayers, uniaxial stretching and subsequent unloading induces formation of mono-stable arches/rolls, saddles, tubular shapes, or helical shapes. While formation of rolls and helix under uniaxial strain mismatch has been documented before(Wisinger et al., 2019) on a similar system, the formation of saddle and half-tube shapes through uniaxial loading is a new finding. To our knowledge, such

a strain-dependent transition in the direction and sign of curvature has not been noted previously, and is the focus of this section.

Due to Poisson effects, uniaxial stretch-release creates non-equi-biaxial strain mismatch between the layers of the rubber-plastic bilayer such that $\epsilon_{x,mis} > 0$ and $\epsilon_{y,mis} < 0$. Here, ϵ is the logarithmic strain defined as $\epsilon = \ln(\lambda)$. A tube shape reduces ϵ_y while leaving ϵ_x unaffected, whereas a roll/arch shape reduces ϵ_x while leaving ϵ_y unaffected. Therefore when $|\epsilon_{y,mis}| > |\epsilon_{x,mis}|$, a tube is expected to be the favored configuration since it allows more energy reduction than a roll/arch shape. However, the magnitude of Poisson strain is much smaller than the imposed uniaxial strain ($|\epsilon_{y,mis}| < |\epsilon_{x,mis}|$.). Hence it is not clear how Poisson effects induce half-tube shapes or saddles when λ_{max} is large.

Section 5.3.3 showed that at large values of λ_{max} the elastic strain mismatch in the X and Y direction can become decoupled, coinciding with the formation of wrinkles. Therefore, in section 5.4.1, through a minimal model we examine how the uncoupling of elastic strain mismatch in the X and Y direction affect the shapes created. The model is not predictive, instead takes as input the final stretch at the interface in the X and Y direction. While, high aspect ratio wrinkles are known to form on elastic stretch release systems(Y. C. Chen & Crosby, 2014), extreme aspect ratios are observed when the film can yield(Takei et al., 2016; Yang et al., 2017), suggesting that yielding can have an indirect effect on the uncoupling of the two stretch mismatches.

5.4.1 Saddle Model

As an approximation, the mechanical contribution of the plastic film is ignored. Accordingly, the plastic film is treated as a coating layer, without structural functionalities, which

applies known strain mismatches $\lambda_{x,mis} > 1$ and $\lambda_{y,mis} < 1$, on the surface of the rubber sheet. Informed by the experimental observations, the rubber sheet is assumed to take on a saddle shape with a uniform curvature at all locations. The model identifies the combination of curvatures (κ_x,κ_y) that minimizes the total strain energy in the rubber. This approach is similar to (Wissman, Finkenauer, Deseri, & Majidi, 2014).Here (κ_x, κ_y) correspond to the curvatures of the centerlines of the top surface around the X and Y directions respectively. These saddles can approach arches/rolls ($|\kappa_x| \ll |\kappa_y|$) or half-tubes ($|\kappa_x| \gg |\kappa_y|$). Accordingly, the model can evaluate whether there is an arch to half-tube transition as the imposed stretches are varied. Any pairs of $\lambda_{x,mis}$ and $\lambda_{y,mis}$ can be imposed, including combinations that do or do not obey the uniaxial kinematic relationship, $\lambda_{y,mis} = 1/\sqrt{\lambda_{y,mis}}$. We emphasize that the mismatch stretches are not calculated from the model but provided as inputs as measured from experiment.

We represent the rubber as a neo-Hookean slab with dimensions L, W, and H^r in the reference configuration subjected to biaxial stretches $\lambda_{x,mis} > 1$ and $\lambda_{y,mis} < 1$ imposed on the top surface, which induce bending deformation (Figure 36A). The corresponding strain energy density (ψ^r) is given by

$$\psi^r(\lambda_1, \lambda_2, \lambda_3) = \mu^r(\lambda_1^2 + \lambda_2^2 + \lambda_3^2 - 3) \tag{5.2}$$

where, μ_r is the shear modulus taken as 1 MPa, and λ_i (i = 1-3) are the principal stretches. Here 1 is taken as the X direction, 2 as the Y direction, and 3 as the Z direction (normal to the sample) in the undeformed reference configuration (Figure 36A). And $\lambda_3 = \frac{1}{\lambda_1 \cdot \lambda_2}$, since volume is conserved.

The deformation gradient, $\boldsymbol{F}$, is decomposed multiplicatively into two parts, as the stretch mismatch, $\boldsymbol{F_m}$, and bending contribution, $\boldsymbol{F_b}$. The stretch mismatch is defined as follows:

$$\boldsymbol{F_m} = diag\left(\lambda_{x,mis}, \lambda_{y,mis}, \frac{1}{\lambda_1 \cdot \lambda_2}\right) \tag{5.3}$$

The bending contribution corresponds to a saddle shape, as in (Wissman et al., 2014), namely:

$$\boldsymbol{F_b} = diag\left(\left(1 + \kappa_y z + (1 - \cos(-\kappa_x \cdot y))\left(-\kappa_y z - \frac{\kappa_y}{\kappa_x}\right)\right), (\kappa_x z + 1), \frac{1}{\lambda_1 \cdot \lambda_2}\right) \tag{5.4}$$

where z and y are the coordinates mapping points in the current configuration corresponding to the Z and Y ones in the reference configuration. We consider the following approximation: z ∈ [0 to $-h^r \approx \frac{H^r}{\lambda_{x,mis} \cdot \lambda_{y,mis}}$], and $y \in [-\frac{w}{2} \approx -\frac{W \cdot \lambda_{y,mis}}{2}$ to $\frac{w}{2} \approx \frac{W \cdot \lambda_{y,mis}}{2}$].

The total deformation gradient is, $\boldsymbol{F} = \boldsymbol{F_b F_m}$ **:**

$$\boldsymbol{F} = diag\begin{pmatrix}\left(\kappa_y z + \left(-\kappa_y z - \frac{\kappa_y}{\kappa_x}\right)(1 + \cos(y\,\kappa_x)) + 1\right)\lambda_{x,mis}, \\ (1 + \kappa_x z)\,\lambda_{y,mis}, \frac{1}{\lambda_1 \cdot \lambda_2}\end{pmatrix} \tag{5.5}$$

Substituting these λ_i values into Eqn. 5.2 then gives an explicit expression for ψ^r at any location within the slab. The total strain energy (U^r) in the rubber substrate is then evaluated by integrating the strain energy density ψ^r over the entire slab.

$$U^r = \int_{V^r} \psi^r dV \tag{5.6}$$

where V^r is the volume of the rubber slab. Given the slab dimensions and the mismatch stretches, we now seek the combination of curvatures, (κ_x, κ_y), that minimize U^r.

This minimization was conducted graphically as follows. A pair of curvatures (κ_x, κ_y) was selected. Eqn. 5.2 (with λ_i values from Eqn. 5.5) was used to evaluate ψ^r (Eqn. 5.2) at all points

on a 50x50 grid in the range $y \in [0, W]$ and $z \in [0, h^r]$. Integrating these values as per Eqn. 5.6 gave the total strain energy U^r corresponding to the selected pair of curvatures. This calculation was repeated at all combinations of curvatures (κ_x, κ_y) within the range $\kappa_x h^r \in [0,1)$ and $\kappa_y h^r \in [0, -1)$, with $\kappa_x h^r$and $\kappa_y h^r$ increments of 0.02. This yielded the entire strain energy landscape $U^r(\kappa_x, \kappa_y)$, from which the curvatures corresponding to the minimum energy can be identified readily.

Figure 36B is an illustrative plot of the dimensionless energy landscape, $U^r/\mu^r V^r$ against dimensionless curvatures $\kappa_x h^r$and $\kappa_y h^r$ for ($\lambda_{x,mis}$, $\lambda_{y,mis}$) = (1.4, 0.67), $W = 8\,mm$ and $H^r = 750\,\mu m$. V^r is the volume of the rubber substrate. This pair of mismatch stretches show minimum energy for a saddle shape with nondimensional curvatures $\kappa_x h^r = -0.11$ and $\kappa_y h^r = 0.24$. The advantage of this graphical procedure is that it simultaneously confirms that for all cases in Figure 37, U^r is convex shape with a single minimum, i.e., the predicted saddle shapes are stable.

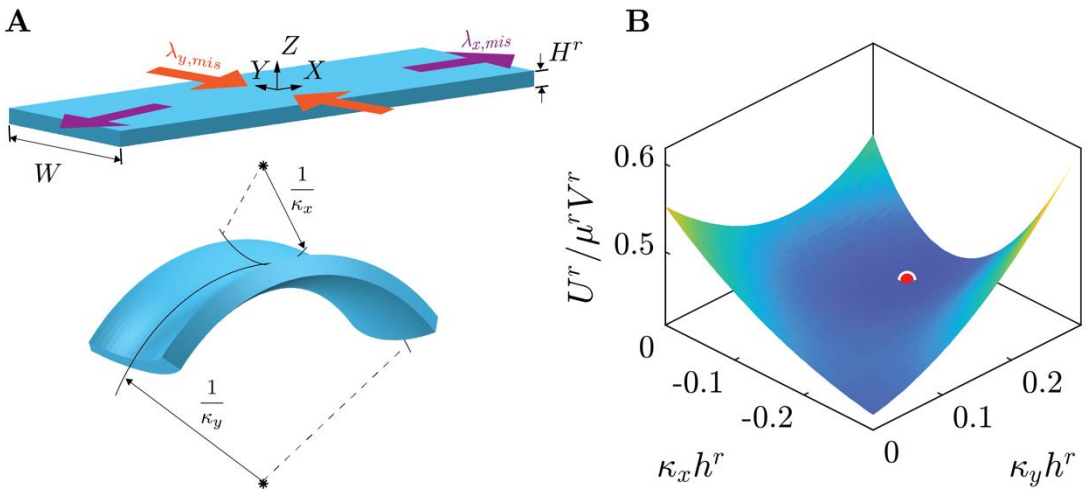

Figure 36: (A) Illustration of boundary conditions on the model. The strain mismatches $\lambda_{x,mis}$ and $\lambda_{y,mis}$ is applied on the top surface. (B) Dimensionless energy landscape as a function of the two dimensionless curvatures $\kappa_x h^r$ and $\kappa_y h^r$.

The above procedure now allows us to predict the curvatures, and hence shape changes, corresponding to any prescribed ($\lambda_{x,mis}$, $\lambda_{y,mis}$). The chief question of interest is whether an arch to half-tube is predicted as increasing λ_{max} changes the values of ($\lambda_{x,mis}$, $\lambda_{y,mis}$).

We first apply the model, substituting the mismatch stretches from Figure 37A, which were estimated from the free-standing films (Eqn. 5.1). Width is taken as 8 mm and thickness is 750 μm. It is important to note that these pairs of $\lambda_{x,mis}$ and $\lambda_{y,mis}$ obey uniaxial kinematics ($\lambda_{y,mis} = 1/\sqrt{\lambda_{x,mis}}$). The corresponding curvatures ($\kappa_x h^r$, $\kappa_y h^r$) that minimize strain energy U^r are shown in Figure 37B. It is immediately apparent that in all cases, $\kappa_x \approx 0$, whereas $\kappa_y > 0$, i.e., only arch/roll shapes are predicted. This is in agreement with the existing literature(DeSimone, 2018).

Next, to capture the effect of inelastic compression and wrinkling, we apply the model using the mismatch stretches from Figure 37C which were estimated from the final shape of the bilayers ($\bar{\lambda}_{x,mis}, \bar{\lambda}_{y,mis}$). As discussed in Section 5.3.3, these values are much smaller than those calculated from freestanding plastic due to inelastic deformation during the release step. Further, for samples that wrinkle (yellow shaded region in Figure 37C), the x-direction mismatch reduces with increasing prestretch, and $\bar{\lambda}_{y,mis} \neq 1/\sqrt{\bar{\lambda}_{x,mis}}$. The corresponding curvatures that minimize the energy for the pairs ($\bar{\lambda}_{x,mis}, \bar{\lambda}_{y,mis}$) are shown in Figure 37D. These trends are similar to those observed experimentally and do predict a transition from arch/roll shapes to tube shapes as the applied stretch increases. Indeed, even the quantitative values of the non-dimensional curvature are in excellent agreement with the measured values.

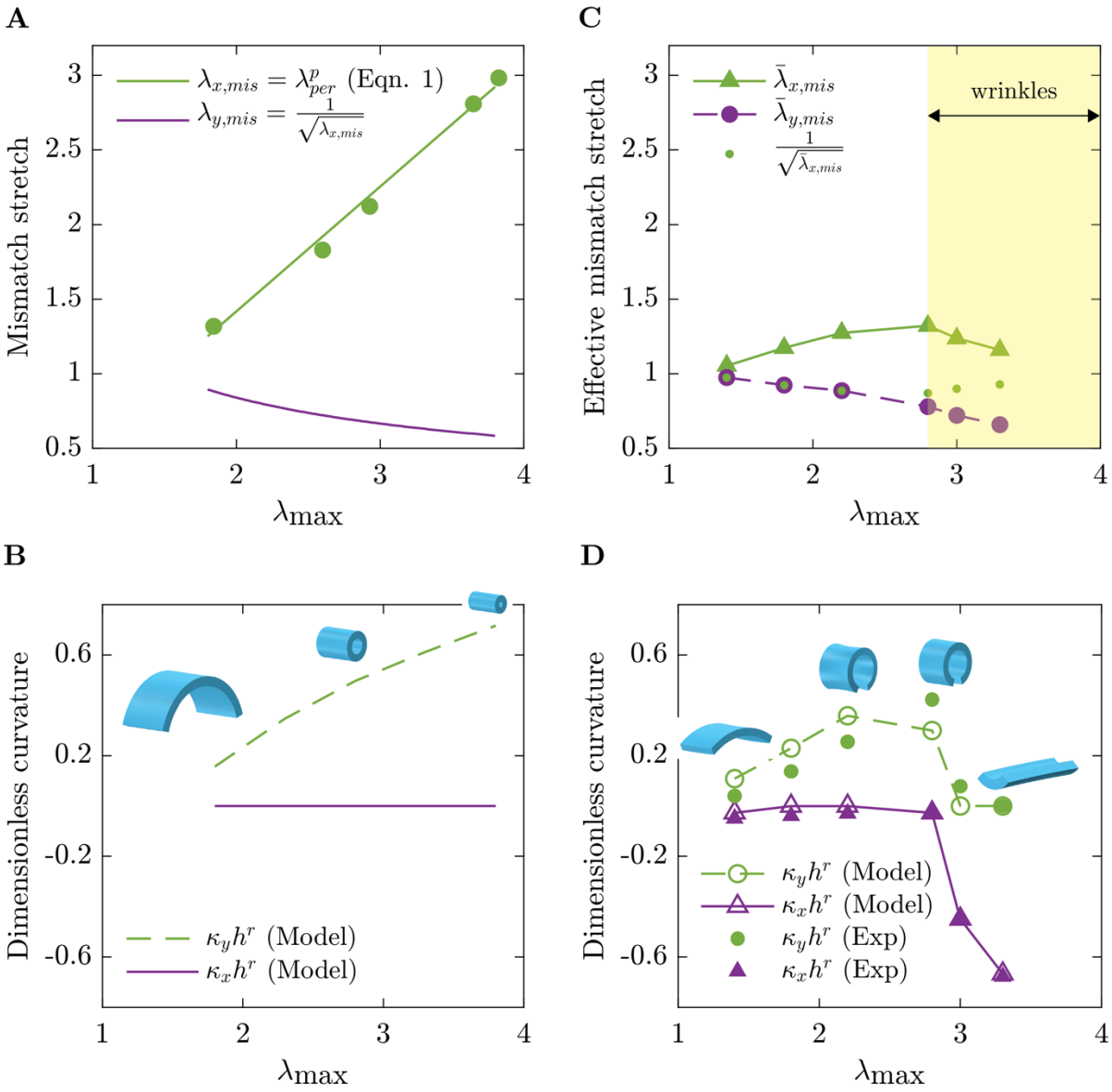

Figure 37: (A) The mismatch stretches ($\lambda_{x,mis}$ *and* $\lambda_{y,mis}$) estimated from the behavior of the free-standing layers vs the maximum applied stretch. Here $\lambda_{x,mis}$ is taken to be equal to λ^{p}_{per}. (B) Model predictions for the normalized curvatures for the mismatch stretch from freestanding behavior of layers shown in Figure 37A. (C) The effective strain mismatch obtained experimentally from the final configuration of bilayers shown in Figure 29. (D) Model predictions for the normalized curvatures using the mismatch stretches from Figure 37C. The experimentally measured dimensionless curvatures (same as from Figure 29J) are shown as filled symbols.

The central conclusion therefore is that a neo-Hookean slab of the geometry examined here, when subjected to biaxial surface stretches, does not show saddles shapes if the applied stretches obey uniaxial deformation kinematics. Surface stretch states that deviate from uniaxial kinematics may show saddle shapes. Furthermore, if $\lambda_{y,mis}$ is farther from 1 than expected from uniaxial kinematics, a curvature flip from an arch/roll to a tube is predicted that agrees quantitatively with experiments. Thus, at least for samples such as in this paper in which the plastic layer is thin, the central role of in-plane yielding, and wrinkling is to decouple the mismatch stretches. The final shape can then be regarded as the response of the rubber slab to these stretches.

While the model is quantitatively successful in predicting curvatures and the transition in shapes with increasing λ_{max}, it has significant limitations. First, the strain energy in the film is ignored. Second, only three shapes are explored in the model, an arch/roll, tube, or a saddle. The model cannot capture helical deformations. Third, the model is developed specifically for the cases examined here for which $L > W \gg H^r$, and the saddle shapes were presumed to be invariant along the X-direction. For samples with $L < W$ (not studied in this paper), the model is not suitable. Finally, and most importantly, the dependence of stretches ($\lambda_{x,mis}, \lambda_{y,mis}$) on λ_{max} is measured from experiments and is not solved for in the model. We reiterate that a full model including plasticity effects would be able to predict the mismatch stresses, and not provide them as input as done here.

5.5 Summary and Conclusions

In summary, we have explored shape changes induced by stretching rectangular strips of rubber-plastic bilayer uniaxially, and then releasing them back to a stress-free state. Such shape

changes result from deformation-induced strain mismatch: the plastic deforms permanently, whereas the rubber deforms elastically. Accordingly, upon stretching, the stress-free shape of the plastic is longer and narrower than of the rubber, and hence upon releasing, the specimen bends. We found that the bilayers formed helical shapes when the sample had small width or small thickness. Otherwise, the samples formed stable arch/rolls when the applied stretch was small, tubes when the applied stretch was large, and saddles when the applied stretch was intermediate. Perhaps the most unexpected result from this paper is that as the stretch prior to release is increased, the sign of curvature and direction of the curvature both flip: samples at small stretches bend into arches/rolls with the plastic on the outside, whereas at larger stretches, they bend into half-tubes with the plastic on the inside.

Much of this paper focuses on quantifying the role of inelastic deformation in the shape changes. We document numerous differences between elastic-plastic bilayers with a deformation-induced strain mismatch vs elastic-elastic bilayers with a strain mismatch induced by differential expansion or prestretching. Most importantly, we show that that yielding of the plastic during release is a dominant feature of the mechanics of elastic-plastic bilayers. At small applied stretches, the rubber forces the plastic to yield in-plane. At large applied stretches, the plastic also yields by developing permanent wrinkles, and such wrinkling has an enormous effect on all aspects of shape changes. The net result of yielding is that the actual strain mismatch is far smaller than that expected from the behavior of free-standing plastic and rubber films. We have developed a model in which experimentally measured mismatch stretches act on the surface of a neo-Hookean slab, which then responds by bending into saddle shapes. In the limit of small or large stretches, these saddle shapes approach either arches or rolls, consistent with observations. While this model captures the curvature flip quantitatively, a full model that can predict the mismatch stretches

remains to be developed. Overall, it appears that bending, twisting, saddle formation, in-plane yielding, and elastic or inelastic wrinkling are all competitive mechanisms that can relieve strain mismatch. Only a model that fully couples all these mechanisms can be truly predictive. Elastic-plastic composites are already being considered for applications such as artificial muscles, and further, deformation-induced strain mismatch can provide a new approach to origami design. A clear understanding of shape changes that come from an interplay of inelastic and elastic deformations can guide these new applications of elastic-plastic composites.

6.0 Conclusions and Future works

The mechanics of a yielding material bonded to an elastic substrate have been explored before. Under tensile deformation, delocalization of strain has been observed when a yielding metal is laid on an elastic polymeric substrate (T. Li et al., 2005). In contrast, the plastics discussed in this thesis undergo extreme stretches by the process of cold drawing. The modification in the neck properties during drawing by the addition of rubber is being explored for the first time, in this thesis. Meanwhile, on failure, bonding an elastomer layer has been shown to improve the toughness of plastic-like polypropylene(Hachisuka et al., 2019). While the competition of ductile and brittle behavior at the notch tip has been studied before, this thesis explored the large deformation in the process zone, and the effect of bonding a rubber layer has on process zone kinematics for the first time. Finally, plasticity has been previously used to create shapes through elastic strain mismatch in polymeric bilayers(Wisinger et al., 2019). However, in this thesis, the magnitude of the elastic strain mismatch is many times the maximum strain values that has been studied previously. This allowed for the unlocking of alternate energy minimization pathways, thereby creating different shapes previously not observed. Additionally, it is showed here that the formation of alternate shapes is driven by the yielding of the plastic in compression and formation of wrinkles. While the tensile, failure, and shape generation in laminate materials composed of elastic and yielding materials has been explored before, this thesis explored the same in rubber-plastic laminates at very large deformations.

6.1 Major conclusions

The tensile behavior of the LLDPE-SEPS laminates under extreme stretches was studied. The addition of a soft rubber layer can significantly modify the tensile behavior of the plastic. The modulus of the rubber controlled the onset of necking, whereas the strain hardening of the rubber controlled the stretch in the neck as well as the rubber thickness required to impose homogeneous deformation.

Thin films of HDPE underwent ductile fracture in the presence of a visible defect. The ductile fracture involved plastic blunting followed by crack initiation in the process zone. The addition of rubber caused the crack initiation to be delayed to a larger applied stretch. We propose that the crack initiation is governed by both the extent to which the material at the crack tip is deformed and by the triaxial stress state formed at the boundary of the process zone. We attribute this to a decrease in the stretch and stress triaxiality at the process zone boundary. Further, the size of the process zone formed decreased with the rubber fraction in the composite.

Stretch release of Natural Rubber–LLDPE bilayers created a variety of shapes. A remarkable dependence of the final shape upon the stretch applied prior to release was observed. At a small stretch, all bilayers bend into arch or roll shapes with the plastic on the convex face. At a large stretch, the bilayers bend into half-tubes with the plastic, now heavily wrinkled, becoming the concave face. Thus, the sign and direction of the curvature both flip at a large applied stretch. Between these two extremes, saddle shapes appear, which have characteristics of both arches as well as half-tubes. Sufficiently narrow samples show different behavior: they transition from arches to helices as stretch increases. Further, all these shapes are stable. The numerous ways in which the mechanics of rubber-plastic bilayers differs from that of fully-elastic bilayers are documented. Most importantly, yielding of the plastic layer during the shape change strongly

affects the mechanics of the elastic-plastic bilayers, and yielding accompanied by plastic wrinkling has an especially large effect. A strain energy model illustrates how the change in shape is dictated by the change in the ratio of elastic strain mismatch in the two directions due to the formation of wrinkles at the rubber-plastic interface.

6.2 Future works

Two projects as a continuation of this thesis are proposed as future work:

- First, fracture of HDPE is shown to be decided by the interplay between yielding and stress triaxiality. The stress triaxiality is affected by the factors like notch radius and thickness. However, strain rate would affect the yield stress. Cold drawing materials like HDPE are subjected to large true strain rates at modest nominal deformation rates. This is because large deformation is concentrated at the propagating neck front. Since the addition of rubber not only reduces the stretch in the neck but also widens the neck front, there will be significant reduction in the true strain rate of deformation due to addition of rubber. The strain rate effect needs to be studied to evaluate the effect of rubber addition even at a modest applied deformation rate.
- Second, in an elastic-elastic system, uniaxial strain mismatch can create only shapes with uni-directional curvature. The stretch release of Natural rubber-LLDPE bilayers showed that the variety of shapes could be realized by increasing the applied stretch prior to release. This happens due to two phenomena. The first is the formation of wrinkles at the rubber plastic interface, and the second is the in-

plane compressive yielding in the plastic during unloading. Both of which redistributed the elastic strain mismatch in the longitudinal and orthogonal directions. The model presented in the thesis has sufficiently elucidated the effect of redistribution of elastic strain mismatch on the final shape. However, the model is not predictive. A predictive model which models considering LLDPE as elastic-plastic material will be a useful tool to relate the applied deformation to the final shape formed.

Bibliography

Abdullah, A. M., Li, X. L., Braun, P. V., Rogers, J. A., & Hsia, K. J. (2018). Self-Folded Gripper-Like Architectures from Stimuli-Responsive Bilayers. *Advanced Materials, 30*(31), 9. doi:10.1002/adma.201801669

Alben, S., Balakrisnan, B., & Smela, E. (2011). Edge Effects Determine the Direction of Bilayer Bending. *Nano Letters, 11*(6), 2280-2285. doi:10.1021/nl200473p

Amoabeng, D., & Velankar, S. S. (2017). A review of conductive polymer composites filled with low melting point metal alloys. *Polymer Engineering & Science, 58*(6), 1010-1019. doi:10.1002/pen.24774

Anderson, T. L. *Fracture mechanics: Fundamentals and applications*. Florida: CRC Press.

Andreasson, E., Kao-Walter, S., & Ståhle, P. (2014). Micro-mechanisms of a laminated packaging material during fracture. *Engineering Fracture Mechanics, 127*, 313-326. doi:10.1016/j.engfracmech.2014.04.017

Andrews, J. M., & Ward, I. M. (1970). COLD-DRAWING OF HIGH DENSITY POLYETHYLENE. *Journal of Materials Science, 5*(5), 411-&. doi:10.1007/bf00550003

Arafat, Y., Dutta, I., & Panat, R. (2015). Super-stretchable metallic interconnects on polymer with a linear strain of up to 100%. *Applied Physics Letters, 107*(8), 5. doi:10.1063/1.4929605

Arafat, Y., Dutta, I., & Panat, R. (2016). On the deformation mechanisms and electrical behavior of highly stretchable metallic interconnects on elastomer substrates. *Journal of Applied Physics, 120*(11), 11. doi:10.1063/1.4962453

Argon, A. S. (2013a). The Physics of Deformation and Fracture of Polymers. In *The Physics of Deformation and Fracture of Polymers* (pp. 325-341). Cambridge, U. K: Cambridge University Press.

Argon, A. S. (2013b). The Physics of Deformation and Fracture of Polymers. In *The Physics of Deformation and Fracture of Polymers* (pp. 273-324). Cambridge, U. K: Cambridge University Press.

Argon, A. S. (2013a). The Physics of Deformation and Fracture of Polymers- Instabilities in extensional plastic flow. In *The Physics of Deformation and Fracture of Polymers*: Cambridge University Press.

Argon, A. S. (2013b). The Physics of Deformation and Fracture of Polymers- plasticity og glassy polymers and plasticity of semi crystalline polymers. In *The Physics of Deformation and Fracture of Polymers*: Cambridge University Press.

Armon, S., Efrati, E., Kupferman, R., & Sharon, E. (2011). Geometry and Mechanics in the Opening of Chiral Seed Pods. *Science, 333*(6050), 1726-1730. doi:10.1126/science.1203874

Bao, Y., & Wierzbicki, T. (2004). On fracture locus in the equivalent strain and stress triaxiality space. *International Journal of Mechanical Sciences, 46*(1), 81-98. doi:10.1016/j.ijmecsci.2004.02.006

Barenblatt, G. I. (1974). Neck Propagation in polymers. *Rheol. Acta, 13,* 924-933.

Bartczak, Z., Argon, A. S., Cohen, R. E., & Weinberg, M. (1999). Toughness mechanism in semi-crystalline polymer blends: I. High-density polyethylene toughened with rubbers. *Polymer, 40*(9), 2331-2346. doi:10.1016/s0032-3861(98)00445-5

Ben Bettaieb, M., & Abed-Meraim, F. (2017). Localized Necking in Elastomer-Supported Metal Layers: Impact of Kinematic Hardening. *Journal of Manufacturing Science and Engineering-Transactions of the Asme, 139*(6), 10. doi:10.1115/1.4035183

Bigg, D. M. (1976). A Review of Techniques for Processing Ultra High Modulus Polymers. *Plolymer Engineering and Science, 16,* 725-734.

Bower, A. F. (2010). Applied Mechanics of Solids. In *Applied Mechanics of Solids* (pp. 562-563). Boca Raton, Florida: CRC Press.

Calvert, P. (2009). Hydrogels for Soft Machines. *Advanced Materials, 21*(7), 743-756. doi:10.1002/adma.200800534

Carothers, W. H., & Hills, J. W. (1932). Studies of Polymerization and Ring Formation. XV. Artificial fibres from synthetic linear condensation superpolymers. *J. Am. Chem. Soc., 54,* 1579.

Caruso, N. A., Cvetkovic, A., Lucantonio, A., Noselli, G., & DeSimone, A. (2018). Spontaneous morphing of equibiaxially pre-stretched elastic bilayers: The role of sample geometry. *International Journal of Mechanical Sciences, 149,* 481-486. doi:10.1016/j.ijmecsci.2017.08.049

Cendula, P., Kiravittaya, S., Monch, I., Schumann, J., & Schmidt, O. G. (2011). Directional roll-up of nanomembranes mediated by wrinkling. *Nano Lett, 11*(1), 236-240. doi:10.1021/nl103623e

Cendula, P., Malachias, A., Deneke, C., Kiravittaya, S., & Schmidt, O. G. (2014). Experimental realization of coexisting states of rolled-up and wrinkled nanomembranes by strain and etching control. *Nanoscale, 6*(23), 14326-14335. doi:10.1039/c4nr03986f

Charlot, B., Sun, W., Yamashita, K., Fujita, H., & Toshiyoshi, H. (2008). Bistable nanowire for micromechanical memory. *Journal of Micromechanics and Microengineering, 18*(4). doi:10.1088/0960-1317/18/4/045005

Chen, C., Wang, Z. J., & Suo, Z. G. (2017). Flaw sensitivity of highly stretchable materials. *Extreme Mechanics Letters, 10,* 50-57. doi:10.1016/j.eml.2016.10.002

Chen, Y. C., & Crosby, A. J. (2014). High aspect ratio wrinkles via substrate prestretch. *Adv Mater, 26*(32), 5626-5631. doi:10.1002/adma.201401444

Chen, Z., Guo, Q., Majidi, C., Chen, W., Srolovitz, D. J., & Haataja, M. P. (2012). Nonlinear geometric effects in mechanical bistable morphing structures. *Phys Rev Lett, 109*(11), 114302. doi:10.1103/PhysRevLett.109.114302

Chen, Z., Majidi, C., Srolovitz, D. J., & Haataja, M. (2011). Tunable helical ribbons. *Applied Physics Letters, 98*(1). doi:10.1063/1.3530441

Choi, B. H., Demirors, M., Patel, R. M., deGroot, A. W., Anderson, K. W., & Juarez, V. (2010). Evaluation of the tear properties of polyethylene blown films using the essential work of fracture concept. *Polymer, 51*(12), 2732-2739. doi:10.1016/j.polymer.2010.04.001

Coates, P. D., & Ward, I. M. (1978). The plastic deformation behaviour of linear polyethylene and polyoxymethylene. *Journal of Materials Science, 13*(9), 1957-1970. doi:10.1007/bf00552903

Coates, P. D., & Ward, I. M. (1980). Neck Profiles in Drawn Linear Polyethylene. *Journal of Materials Science, 15*(11), 2897-2914. doi:10.1007/bf00550561

Coleman, B. D. (1983). NECKING AND DRAWING IN POLYMERIC FIBERS UNDER TENSION. *Archive for Rational Mechanics and Analysis, 83*(2), 115-137. Retrieved from <Go to ISI>://WOS:A1983RB49500002

Considère, A. G. (1885). *Annales P., 9*, 574-775.

Courtney, T. H. (1990a). Mechanical Behavior of Materials. In *Mechanical Behavior of Materials* (2 ed., pp. 20-30). Illinois: Waveland Press.

Courtney, T. H. (1990b). *Mechanical Behavior of Materials*. Illinois: Waveland Press.

Courtney, T. H. (1990c). Mechanical Behavior of Materials. In (2 ed., pp. 20-30). Illinois: Waveland Press.

Coyle, S., Majidi, C., LeDuc, P., & Hsia, K. J. (2018). Bio-inspired soft robotics: Material selection, actuation, and design. *Extreme Mechanics Letters, 22*, 51-59. doi:10.1016/j.eml.2018.05.003

Creton, C., & Ciccotti, M. (2016). Fracture and adhesion of soft materials: a review. *Reports on Progress in Physics, 79*(4), 57. doi:10.1088/0034-4885/79/4/046601

Crist, B., & Metaxas, C. (2004). Neck propagation in polyethylene. *Journal of Polymer Science Part B-Polymer Physics, 42*(11), 2081-2091. doi:10.1002/polb.20087

Cui, J. X., Adams, J. G. M., & Zhu, Y. (2018). Controlled bending and folding of a bilayer structure consisting of a thin stiff film and a heat shrinkable polymer sheet. *Smart Materials and Structures, 27*(5). doi:ARTN 055009
10.1088/1361-665X/aab9d9

DeSimone, A. (2018). Spontaneous bending of pre-stretched bilayers. *Meccanica, 53*(3), 511-518. doi:10.1007/s11012-017-0732-z

El-Sayed, H. F. M., Barton, D. C., Abdel-Latif, L. A., & Kenawy, M. (2001). Experimental and numerical investigation of deformation and fracture of semicrystalline polymers under

varying strain rates and triaxial states of stress. *Plastics Rubber and Composites, 30*(2), 82-87. doi:10.1179/146580101101541471

Erickson, J. L. (1975). Equilibrium of bars. *Journal of Elasticity, 5*, 191-201.

Fager, L. O., & Bassani, J. L. (1986). PLANE-STRAIN NECK PROPAGATION. *International Journal of Solids and Structures, 22*(11), 1243-1257. doi:10.1016/0020-7683(86)90079-x

Finot, M., & Suresh, S. (1996). Small and large deformation of thick and thin-film multi-layers: Effects of layer geometry, plasticity and compositional gradients. *Journal of the Mechanics and Physics of Solids, 44*(5), 683-721. doi:10.1016/0022-5096(96)84548-0

Forterre, Y., Skotheim, J. M., Dumais, J., & Mahadevan, L. (2005). How the Venus flytrap snaps. *Nature, 433*(7024), 421-425. doi:10.1038/nature03185

Fouad, H. (2010). Experimental and numerical studies of the notch strengthening behaviour of semi-crystalline ultra-high molecular weight polyethylene. *Materials & Design, 31*(3), 1117-1129. doi:10.1016/j.matdes.2009.09.042

Fouad, H., & Elleithy, R. (2011). High density polyethylene/graphite nano-composites for total hip joint replacements: processing and in vitro characterization. *J Mech Behav Biomed Mater, 4*(7), 1376-1383. doi:10.1016/j.jmbbm.2011.05.008

Fung, Y. C. (1993). *Biomechanics Mechanical Properties of Living Tissues* (2 ed.): Springer.

G. E. Dieter, H. A. K., S. L. Semiatin. (2003). Handbook of Workability and Process Design. In (pp. 147). United States of America: ASM International.

G'Sell, C., Aly-Helal, N. A., & Jonas, J. J. (1983). Effect of stress triaxiality on neck propagation during the tensile stretching of solid polymers. *Journal of Materials Science, 18*(6), 1731-1742. doi:10.1007/bf00542069

Gearing, B. P., & Anand, L. (2004). Notch-sensitive fracture of polycarbonate. *International Journal of Solids and Structures, 41*(3-4), 827-845. doi:10.1016/j.ijsolstr.2003.09.058

Geng, J., & Selinger, J. V. (2012). Deformation of an asymmetric thin film. *Phys Rev E Stat Nonlin Soft Matter Phys, 86*(3 Pt 2), 036602. doi:10.1103/PhysRevE.86.036602

Gerbode, S. J., Puzey, J. R., McCormick, A. G., & Mahadevan, L. (2012). How the cucumber tendril coils and overwinds. *Science, 337*(6098), 1087-1091. doi:10.1126/science.1223304

Goriely, A., & Tabor, M. (1998). Spontaneous Helix Hand Reversal and Tendril Perversion in Climbing Plants. *Physical Review Letters, 80*(7), 1564-1567. doi:10.1103/PhysRevLett.80.1564

Gsell, C., & Jonas, J. J. (1979). Determination of the Plastic Behavior of Solid Polymers at Constant True Strain Rate. *Journal of Materials Science, 14*(3), 583-591. Retrieved from <Go to ISI>://WOS:A1979GM05700008

Hachisuka, R., Kobayashi, T., & Yamaguchi, M. (2019). Improvement of mechanical toughness of polypropylene by laminating with elastomer. *Journal of Polymer Research, 26*(10), 7. doi:10.1007/s10965-019-1910-6

Han, L., Zhang, Y., Xue, S., Zhou, B., & Liu, C. (2020). Behavior of polyethylene under different triaxial stress states: An experimental and numerical study. *Proceedings of the Institution of Mechanical Engineers, Part L: Journal of Materials: Design and Applications, 235*(3), 527-541. doi:10.1177/1464420720970587

Haward, R. N. (1993). Strain-Hardening of Thermoplastics. *Macromolecules, 26*(22), 5860-5869. doi:10.1021/ma00074a006

Holland, M. A., Li, B., Feng, X. Q., & Kuhl, E. (2017). Instabilities of soft films on compliant substrates. *Journal of the Mechanics and Physics of Solids, 98*, 350-365. doi:10.1016/j.jmps.2016.09.012

Holmes, D. P. (2019). Elasticity and stability of shape-shifting structures. *Current Opinion in Colloid & Interface Science, 40*, 118-137. doi:10.1016/j.cocis.2019.02.008

Holmes, D. P., Roche, M., Sinha, T., & Stone, H. A. (2011). Bending and twisting of soft materials by non-homogenous swelling. *Soft Matter, 7*(11), 5188-5193. doi:10.1039/c0sm01492c

Hu, Y., Hiltner, A., & Baer, E. (2004). Buckling in elastomer/plastic/elastomer 3-layer films. *Polymer Composites, 25*(6), 653-661. doi:10.1002/pc.20060

Hu, Z., Zhang, X., & Li, Y. (1995). Synthesis and application of modulated polymer gels. *Science, 269*(5223), 525-527. doi:10.1126/science.269.5223.525

Huang, M., Cavallo, F., Liu, F., & Lagally, M. G. (2011). Nanomechanical architecture of semiconductor nanomembranes. *Nanoscale, 3*(1), 96-120. doi:10.1039/c0nr00648c

Huang, Z. Y., Hong, W., & Suo, Z. (2005). Nonlinear analyses of wrinkles in a film bonded to a compliant substrate. *Journal of the Mechanics and Physics of Solids, 53*(9), 2101-2118. doi:10.1016/j.jmps.2005.03.007

Hui, C. Y., A, J., Bennison, S. J., & Londono, J. D. (2003). Crack blunting and the strength of soft elastic solids. *Proceedings of the Royal Society of London. Series A: Mathematical, Physical and Engineering Sciences, 459*(2034), 1489-1516. doi:10.1098/rspa.2002.1057

Hutchinson, J. W. (2014). Necking modes in multilayers and their influence on tearing toughness. *Mathematics and Mechanics of Solids, 19*(1), 39-55. doi:10.1177/1081286513505468

Hutchinson, J. W., & Miles, J. P. (1974). Bifurcation Analysis of Onset of Necking in an Elastic-Plastic Cylinder under Uniaxial Tension. *Journal of the Mechanics and Physics of Solids, 22*(1), 61-71. doi:10.1016/0022-5096(74)90014-3

Hutchinson, J. W., & Neale, K. W. (1977). Influence of Strain-Rate Sensititvity on Necking Under Uniaxial Tension. *Acta Metallurgica, 25*(8), 839-846. doi:10.1016/0001-6160(77)90168-7

Hutchinson, J. W., & Neale, K. W. (1983). Neck Propagation. *Journal of the Mechanics and Physics of Solids, 31*(5), 405-426. doi:10.1016/0022-5096(83)90007-8

Ionov, L. (2011). Soft microorigami: self-folding polymer films. *Soft Matter, 7*(15), 6786-6791. doi:10.1039/c1sm05476g

J., K. H., & B., J. P.-Y. (2006). Toughness of high-density polyethylene in plane-strain fracture. *Polymer Engineering & Science, 46*(10), 1428-1432. doi:doi:10.1002/pen.20603

Jia, Z., & Li, T. (2013). Necking limit of substrate-supported metal layers under biaxial in-plane loading. *International Journal of Plasticity, 51*, 65-79. doi:10.1016/j.ijplas.2013.06.007

Jin, L. H., Takei, A., & Hutchinson, J. W. (2015). Mechanics of wrinkle/ridge transitions in thin film/substrate systems. *Journal of the Mechanics and Physics of Solids, 81*, 22-40. doi:10.1016/j.jmps.2015.04.016

Kanik, M., Orguc, S., Varnavides, G., Kim, J., Benavides, T., Gonzalez, D., . . . Anikeeva, P. (2019). Strain-programmable fiber-based artificial muscle. *Science, 365*(6449), 145-150. doi:10.1126/science.aaw2502

Katifori, E., Alben, S., Cerda, E., Nelson, D. R., & Dumais, J. (2010). Foldable structures and the natural design of pollen grains. *Proceedings of the National Academy of Sciences of the United States of America, 107*(17), 7635-7639. doi:10.1073/pnas.0911223107

Kim, J., Kim, C., Song, Y., Jeong, S.-G., Kim, T.-S., & Lee, C.-S. (2017). Reversible self-bending soft hydrogel microstructures with mechanically optimized designs. *Chemical Engineering Journal, 321*, 384-393. doi:10.1016/j.cej.2017.03.125

Kitao, K. (2001). Effect of entanglement on brittle-ductile transition in polyethylene. *Polymer Engineering and Science, 41*(7), 1146-1155. doi:10.1002/pen.10816

Klein, Y., Efrati, E., & Sharon, E. (2007). Shaping of elastic sheets by prescription of non-Euclidean metrics. *Science, 315*(5815), 1116-1120. doi:10.1126/science.1135994

Krishnaswamy, R. K. (2005). Analysis of ductile and brittle failures from creep rupture testing of high-density polyethylene (HDPE) pipes. *Polymer, 46*(25), 11664-11672. doi:10.1016/j.polymer.2005.09.084

Lacour, S. P., Chan, D., Wagner, S., Li, T., & Suo, Z. G. (2006). Mechanisms of reversible stretchability of thin metal films on elastomeric substrates. *Applied Physics Letters, 88*(20), 3. doi:10.1063/1.2201874

Lambricht, N., Pardoen, T., & Yunus, S. (2013). Giant stretchability of thin gold films on rough elastomeric substrates. *Acta Materialia, 61*(2), 540-547. doi:10.1016/j.actamat.2012.10.001

Lee, C., Kim, M., Kim, Y. J., Hong, N., Ryu, S., Kim, H. J., & Kim, S. (2017). Soft robot review. *International Journal of Control, Automation and Systems, 15*(1), 3-15. doi:10.1007/s12555-016-0462-3

Leong, T. G., Benson, B. R., Call, E. K., & Gracias, D. H. (2008). Thin Film Stress Driven Self-Folding of Microstructured Containers. *Small, 4*(10), 1605-1609. doi:10.1002/smll.200800280

Li, B., Cao, Y.-P., Feng, X.-Q., & Gao, H. (2011). Surface wrinkling of mucosa induced by volumetric growth: Theory, simulation and experiment. *Journal of the Mechanics and Physics of Solids, 59*(4), 758-774. doi:10.1016/j.jmps.2011.01.010

Li, T., Huang, Z. Y., Suo, Z., Lacour, S. P., & Wagner, S. (2004). Stretchability of thin metal films on elastomer substrates. *Applied Physics Letters, 85*(16), 3435-3437. doi:10.1063/1.1806275

Li, T., Huang, Z. Y., Xi, Z. C., Lacour, S. P., Wagner, S., & Suo, Z. (2005). Delocalizing strain in a thin metal film on a polymer substrate. *Mechanics of Materials, 37*(2-3), 261-273. doi:10.1016/j.mechmat.2004.02.002

Li, T., & Suo, Z. (2006). Deformability of thin metal films on elastomer substrates. *International Journal of Solids and Structures, 43*(7-8), 2351-2363. doi:10.1016/j.ijsolstr.2005.04.034

Li, T., & Suo, Z. (2007). Ductility of thin metal films on polymer substrates modulated by interfacial adhesion. *International Journal of Solids and Structures, 44*(6), 1696-1705. doi:10.1016/j.ijsolstr.2006.07.022

Li, W., Huang, G., Yan, H., Wang, J., Yu, Y., Hu, X., . . . Mei, Y. (2012). Fabrication and stimuli-responsive behavior of flexible micro-scrolls. *Soft Matter, 8*(27). doi:10.1039/c2sm25366f

Liang, H., & Mahadevan, L. (2009). The shape of a long leaf. *Proc Natl Acad Sci U S A, 106*(52), 22049-22054. doi:10.1073/pnas.0911954106

Lin, J., Guo, Q., Dou, S., Hua, N., Zheng, C., Pan, Y., . . . Chen, W. (2020). Bistable structures with controllable wrinkled surface. *Extreme Mechanics Letters, 36*. doi:10.1016/j.eml.2020.100653

Liu, Y. Q., He, K., Chen, G., Leow, W. R., & Chen, X. D. (2017). Nature-Inspired Structural Materials for Flexible Electronic Devices. *Chemical Reviews, 117*(20), 12893-12941. doi:10.1021/acs.chemrev.7b00291

Logan, D. L. (2007). A first Course in the Finite Element Method. In *A first Course in the Finite Element Method* (pp. 443 - 484). Canada: Thomson.

Lu, N., Wang, X., Suo, Z., & Vlassak, J. (2007). Metal films on polymer substrates stretched beyond 50%. *Applied Physics Letters, 91*(22). doi:10.1063/1.2817234

Lu, N. S., Wang, X., Suo, Z. G., & Vlassak, J. (2007). Metal films on polymer substrates stretched beyond 50%. *Applied Physics Letters, 91*(22). doi:10.1063/1.2817234

Ma, Y. J., Xue, Y. G., Jang, K. I., Feng, X., Rogers, J. A., & Huang, Y. G. (2016). Wrinkling of a stiff thin film bonded to a pre-strained, compliant substrate with finite thickness. *Proceedings of the Royal Society a-Mathematical Physical and Engineering Sciences, 472*(2192), 6. doi:10.1098/rspa.2016.0339

Macionczyk, F., & Bruckner, W. (1999). Tensile testing of AlCu thin films on polyimide foils. *Journal of Applied Physics, 86*(9), 4922-4929. doi:10.1063/1.371461

Malpass, D. B. (2010). *Introduction to Industrial Polyethylene: Properties, Catalysts, and Processes*. Germany: Wiley.

Neale, K. W., & Tugcu, P. (1985). ANALYSIS OF NECKING AND NECK PROPAGATION IN POLYMERIC MATERIALS. *Journal of the Mechanics and Physics of Solids, 33*(4), 323-337. doi:10.1016/0022-5096(85)90032-8

Nelson, C. M. (2016). On Buckling Morphogenesis. *J Biomech Eng, 138*(2), 021005. doi:10.1115/1.4032128

Nguyen, K. Q., Mwiseneza, C., Mohamed, K., Cousin, P., Robert, M., & Benmokrane, B. (2021). Long-term testing methods for HDPE pipe - advantages and disadvantages: A review. *Engineering Fracture Mechanics, 246*. doi:10.1016/j.engfracmech.2021.107629

Nisticò, R. (2020). Polyethylene terephthalate (PET) in the packaging industry. *Polymer Testing, 90*. doi:10.1016/j.polymertesting.2020.106707

O'Connell, P. A., Duckett, R. A., & Ward, I. M. (2002). Brittle-ductile transitions in polyethylene. *Polymer Engineering and Science, 42*(7), 1493-1508. doi:10.1002/pen.11046

Ognedal, A. S., Clausen, A. H., Dahlen, A., & Hopperstad, O. S. (2014). Behavior of PVC and HDPE under highly triaxial stress states: An experimental and numerical study. *Mechanics of Materials, 72*, 94-108. doi:10.1016/j.mechmat.2014.02.002

Pascu, M., Vasile, Cornelia. (2005). *Practical Guide to Polyethylene.* . United Kingdom: RAPRA Technology.

Pieranski, P., Baranska, J., & Skjeltorp, A. (2004). Tendril perversion—a physical implication of the topological conservation law. *European Journal of Physics, 25*(5), 613-621. doi:10.1088/0143-0807/25/5/004

Ramachandran, R. G., de Cortie, J., Maiti, S., Deseri, L., & Velankar, S. S. (2021). Uniaxial stretch-release of rubber-plastic bilayers: Strain-dependent transition to stable helices, rolls, saddles, and tubes. *Extreme Mechanics Letters, 48*. doi:10.1016/j.eml.2021.101384

Ramachandran, R. G., Hariharakrishnan, S., Fortunato, R., Abramowitch, S. D., Maiti, S., & Velankar, S. S. (2018). Necking and drawing of rubber-plastic bilayer laminates. *Soft Matter, 14*(24), 4977-4986. doi:10.1039/c8sm00684a

Ramachandran, R. G., Maiti, S., & Velankar, S. S. (2020). Necking and drawing of rubber–plastic laminate composites: Finite element simulations and analytical model. *Journal of the Mechanics and Physics of Solids, 142*. doi:10.1016/j.jmps.2020.104012

Robertson, J. M., Torbati, A. H., Rodriguez, E. D., Mao, Y. Q., Baker, R. M., Qi, H. J., & Mather, P. T. (2015). Mechanically programmed shape change in laminated elastomeric composites. *Soft Matter, 11*(28), 5754-5764. doi:10.1039/c5sm01004g

Savin, T., Kurpios, N. A., Shyer, A. E., Florescu, P., Liang, H., Mahadevan, L., & Tabin, C. J. (2011). On the growth and form of the gut. *Nature, 476*(7358), 57-62. doi:10.1038/nature10277

Seguela, R. (2007). On the natural draw ratio of semi-crystalline polymers: Review of the mechanical, physical and molecular aspects. *Macromolecular Materials and Engineering, 292*(3), 235-244. doi:10.1002/mame.200600389

Sharon, E., & Efrati, E. (2010). The mechanics of non-Euclidean plates. *Soft Matter, 6*(22). doi:10.1039/c0sm00479k

Shen, Y. L., & Suresh, S. (1995). Elastoplastic deformation of multilayered materials during thermal cycling. *Journal of Materials Research, 10*(5), 1200-1215. doi:10.1557/jmr.1995.1200

Smela, E., Inganas, O., & Lundstrom, I. (1995). Controlled folding of micrometer-size structures. *Science, 268*(5218), 1735-1738. doi:10.1126/science.268.5218.1735

Smela, E., Inganas, O., Pei, Q. B., & Lundstrom, I. (1993). Electrochemical muscles - micromachining fingers and corkscrews. *Advanced Materials, 5*(9), 630-632. doi:10.1002/adma.19930050905

Song, J., Jiang, H., Liu, Z. J., Khang, D. Y., Huang, Y., Rogers, J. A., . . . Koh, C. G. (2008). Buckling of a stiff thin film on a compliant substrate in large deformation. *International Journal of Solids and Structures, 45*(10), 3107-3121. doi:10.1016/j.ijsolstr.2008.01.023

Srinivasan, K., Subbarayan, G., & Siegmund, T. (2012). Wrinkling on irreversibly deforming foundations. *Thin Solid Films, 520*(17), 5671-5682. doi:10.1016/j.tsf.2012.04.071

Takei, A., Jin, L., Fujita, H., Takei, A., Fujita, H., & Jin, L. (2016). High-Aspect-Ratio Ridge Structures Induced by Plastic Deformation as a Novel Microfabrication Technique. *ACS Appl Mater Interfaces, 8*(36), 24230-24237. doi:10.1021/acsami.6b07957

Takei, A., Jin, L., Hutchinson, J. W., & Fujita, H. (2014). Ridge localizations and networks in thin films compressed by the incremental release of a large equi-biaxial pre-stretch in the substrate. *Adv Mater, 26*(24), 4061-4067. doi:10.1002/adma.201306162

van Manen, T., Janbaz, S., & Zadpoor, A. A. (2018). Programming the shape-shifting of flat soft matter. *Materials Today, 21*(2), 144-163. doi:10.1016/j.mattod.2017.08.026

Vandommelen, J., Parks, D., Boyce, M., Brekelmans, W., & Baaijens, F. (2003). Micromechanical modeling of the elasto-viscoplastic behavior of semi-crystalline polymers. *Journal of the Mechanics and Physics of Solids, 51*(3), 519-541. doi:10.1016/s0022-5096(02)00063-7

Vincent, P. I. (1960). The Necking and Cold-Drawing of Rigid Plastics. *Polymer, 1*(1), 7-19. doi:10.1016/0032-3861(60)90003-3

Wallace H. Carothers, J. W. H. (1932). Studies of Polymerization and ring formation. XV. Artificial fibres from synthetic linear condensation superpolymers. *Communication No. 78 from the experimental station of E I Du Pont De Nemours & Co*.

Wang, D., Thouless, M. D., Lu, W., & Barber, J. R. (2020). Generation of perversions in fibers with intrinsic curvature. *Journal of the Mechanics and Physics of Solids, 139*. doi:10.1016/j.jmps.2020.103932

Wang, L., Isaac, G., Wilcox, R., Jones, A., & Thompson, J. (2019). Finite element analysis of polyethylene wear in total hip replacement: A literature review. *Proc Inst Mech Eng H, 233*(11), 1067-1088. doi:10.1177/0954411919872630

Ward, I. M. (1971). In *Mechanical Properties of Solid Polymers* (pp. 47 -55). England: J. W Arrowsmith Ltd.

Ward, I. M. (1971a). Mechanical Properties of Solid Polymers. In *Mechanical Behavior of Solid Polymers* (pp. 321 - 394). Bristol: J. W Arrowsmith Ltd.

Ward, I. M. (1971b). *Mechanical Properties of Solid Polymers* (2 ed.). Bristol: W. Arrowsmith Ltd.

Wisinger, C. E., Maynard, L. A., & Barone, J. R. (2019). Bending, curling, and twisting in polymeric bilayers. *Soft Matter, 15*(22), 4541-4547. doi:10.1039/c9sm00268e

Wissman, J., Finkenauer, L., Deseri, L., & Majidi, C. (2014). Saddle-like deformation in a dielectric elastomer actuator embedded with liquid-phase gallium-indium electrodes. *Journal of Applied Physics, 116*(14). doi:10.1063/1.4897551

Xiang, Y., Li, T., Suo, Z. G., & Vlassak, J. J. (2005). High ductility of a metal film adherent on a polymer substrate. *Applied Physics Letters, 87*(16), 3. doi:10.1063/1.2108110

Xue, Z. Y., & Hutchinson, J. W. (2007). Neck retardation and enhanced energy absorption in metal-elastomer bilayers. *Mechanics of Materials, 39*(5), 473-487. doi:10.1016/j.mechmat.2006.08.002

Xue, Z. Y., & Hutchinson, J. W. (2008). Neck development in metal/elastomer bilayers under dynamic stretchings. *International Journal of Solids and Structures, 45*(13), 3769-3778. doi:10.1016/j.ijsolstr.2007.10.006

Yang, J., Damle, S., Maiti, S., & Velankar, S. S. (2017). Stretching-induced wrinkling in plastic-rubber composites. *Soft Matter, 13*(4), 776-787. doi:10.1039/c6sm01823h

Yin, J., Yague, J. L., Eggenspieler, D., Gleason, K. K., & Boyce, M. C. (2012). Deterministic order in surface micro-topologies through sequential wrinkling. *Adv Mater, 24*(40), 5441-5446. doi:10.1002/adma.201201937

Zhang, Z., Li, Y., Yu, X., Li, X., Wu, H., Wu, H., . . . Chai, G. (2019). Bistable morphing composite structures: A review. *Thin-Walled Structures, 142*, 74-97. doi:10.1016/j.tws.2019.04.040

Zhao, Z. A., Kuang, X., Yuan, C., Qi, H. J., & Fang, D. N. (2018). Hydrophilic/Hydrophobic Composite Shape-Shifting Structures. *Acs Applied Materials & Interfaces, 10*(23), 19932-19939. doi:10.1021/acsami.8b02444